UNIVERSITY OF CAPE TOWN
IYUNIVESITHI YASEKAPA • UNIVERSITEIT VAN KAAPSTAD

Department of Civil Engineering
Computational Continuum Mechanics Group
Polar Engineering Research Group

Permeability of winter and spring first-year ice in the Antarctic marginal ice zone

---

Author: Xuefeng Lin **Supervisor: Prof. Sebastian Skatulla**

18 August 2022

Plagiarism Declaration

- I know that plagiarism is wrong. Plagiarism is to use another's work and to pretend that it is one's own.
- Each significant contribution to and quotation in this document from the work or works of other people has been attributed and has been cited and referenced.
- This thesis is my own work.
- I have not allowed and will not allow anyone to copy my work with the intention of passing it as his or her own work.

Surname: Xuefeng Lin Student Number: LNXXUE001

Date: 18/08/2022 Signature: 

Abstract

This study was part of the 2019 Southern oCean seAsonal Experiment (SCALE) Winter and Spring Cruise of the South African icebreaker SA Agulhas II. First-year spring and winter sea ice were sampled from the Antarctic marginal ice zone. Consolidated pack ice was collected during both cruises, while pancake ice floes and brash ice floes were collected during Winter and Spring Cruise, respectively. The ice cores analyses of temperature, salinity, and texture were subsequently performed during the Spring and Winter Cruise, and an additional falling head permeability test was conducted during the Spring Cruise. The brine volume is determined empirically from sea ice temperature and bulk salinity. The ice permeability is then calculated from the porosity-permeability relation. The mean permeability of spring pack ice is $2.6 \times 10^{-11} \pm 3.67 \times 10^{-11}$ m^2, marginally higher than the winter pack ice with a mean permeability of $1.1 \times 10^{-11} \pm 2.3 \times 10^{-11}$ m^2. Comparing the permeability values of spring and winter consolidated pack ice shows a continuous increase in permeability with seasonal progressions and a rise in ice temperature. The falling head permeability test using kerosene has been made in-house by Hasham Taujoo to determine the in situ sea ice permeability during the Spring Cruise. The experimentally determined permeability values of spring consolidated pack ice were consistent with the above-stated permeability data. However, the permeability values of spring brash ice floes ($1.4 \times 10^{-11} \pm 2.12 \times 10^{-11}$ m^2) determined from porosity-permeability relation deviate from field observations due to the presence of large holes and cracks on the ice samples.

Acknowledgment

I would like to express my deepest appreciation to the following, who helped and guided me throughout the research:

1. Prof. Sebastian Skatulla
2. My parents
3. Mr. Rutger Marquart
4. Dr. Keith MacHutchon
5. A/Prof Marcello Vichi
6. Mr. Emmanuel Omatuku Ngongo
7. Mr. Paul Namalomba
8. Mr. Hasham Taujoo
9. Mr. Ben Adey
10. Miss. Andrea Cook

Contents

List of Figures

List of Tables

Introduction

Background

The Antarctic Marginal Ice Zone (MIZ) of the Southern Ocean is the transitional zone between the open ocean and pack ice where the boundary of MIZ is characterised by the satellite-derived sea ice concentration [80]. MIZ is well known for its harsh atmospheric and oceanic conditions in which sea ice leads to pronounced regional variability in sea ice properties [71]. Lack of understanding results inaccurate prediction of the climate response to MIZ sea ice by current climate models [35]. MIZ sea ice is well under-researched compared to Arctic sea ice, especially in situ ice sampling and testing. For example, numerous in situ permeability tests have been conducted on Arctic sea ice [18, 26, 65] for the past two decades. Such in situ permeability test is yet to be done on MIZ sea ice. Insufficient in situ data from the Antarctic region compelled the researchers to adopt empirically-derived parameters in climate models that have little physical meaning [71]. Therefore, it is essential to perform extensive exploration on the fundamental mechanics of Antarctic sea ice during the period of formation, growth, and decay. A comprehensive understanding of sea ice characteristics can be achieved by combining field observations and remote sensing.

Aim

First-year sea ice samples were collected at the edge of the Antarctic marginal ice zone during the 2019 SCALE Winter and Spring Cruise. The study focuses on the physical properties of the sea ice (pancake ice floe, consolidated pack ice and brash ice floe) with the emphasis on permeability. The properties investigated include temperature, salinity, brine volume, permeability and morphology. The evolution of spring and winter sea ice is accessed through the permeability results. Furthermore, during the Spring Cruise, the permeability is determined experimentally, and the comparison is made against permeability calculated using porosity-permeability relation.

Chapter 1

Literature Review

1.1 Crystal structure of sea ice

Depending on the temperature, three phases are associated with any substance, namely solid, liquid, and gas. Typically, their densities will decrease from solid to liquid to gas. Interestingly, the density of solid ice is lower than the density of water. The theory behind this phenomenon can be explained by the molecular structure of ice. The most common crystal ice structure is called ice Ih where "I" stands for ice and "h" suggests crystal symmetry in a hexagonal system. The structure of ice Ih as shown in Figure 1.1 where water molecules (H_2O) are arranged tetrahedrally, oxygen atoms are located at the apex leading to hexagonal symmetry. The oxygen atoms of the crystal lattice structure are arranged by the hydrogen bonds leading to an open structure and lower density than liquid water [10].

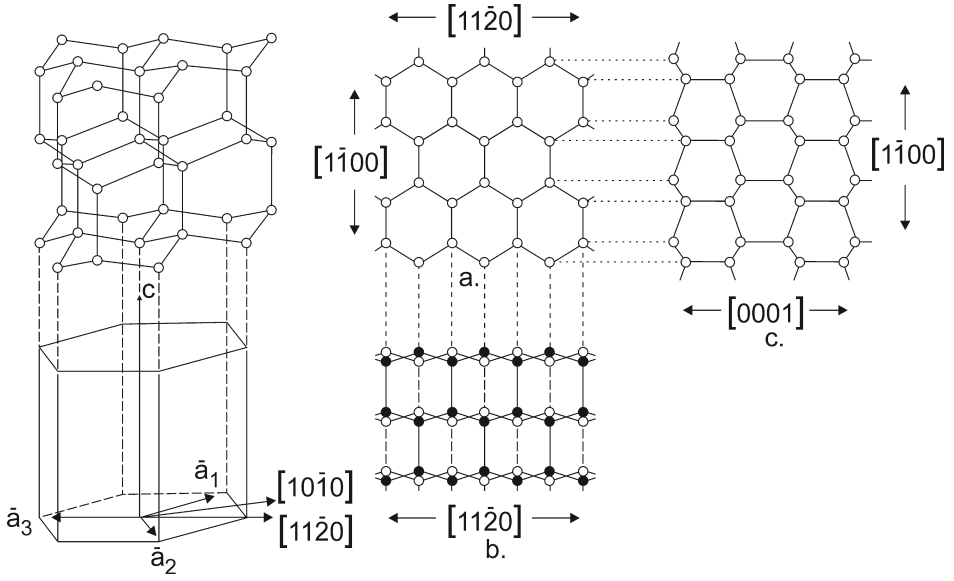

Figure 1.1: Crystal structure of ice Ih. The c-axis is indicated at left and right, the centre panels correspond to a view along (top) and normal (bottom) to the c-axis [1].

It should be noted that the oxygen atoms of ice Ih are arranged in a series of parallel planes with six-fold rotatory symmetry. Such parallel planes are referred to as basal planes defined by three a-axes with the normal vector defined as the c-axis. Basal planes are also known as the planes of weakness or cleavage since they have fewer bonds compared to other crystal planes [10]. Furthermore,at the molecular level, the interface between basal planes is smooth. In contrast, the planes perpendicular to the basal planes are rough, resulting in different interface kinetics [62], hence anisotropy in growth rates. The growth rate along the basal

planes can be up to two magnitudes higher than the growth rate along the c-axis [35]. The anisotropy in growth rate leads to pancake ice rather than sphere ice. Lastly, Hobbs [35], and Wettlaufer [85] found that the partition coefficient of large salt ions into the ice Ih crystal lattice is around 10^{-4}. The majority of salt inclusion happens between basal planes rather than within the ice Ih.

1.2 Granular ice microstructure

1.2.1 Frazil ice

Sea ice is a complex material that consists of solid ice, brine, and air voids, and its properties are dependent heavily on the surrounding environment. Environmental variation results in different grain structures such as granular and columnar [76]. The freezing point of seawater depends on its salinity. Salt content depresses the freezing point. The freezing point of seawater can be approximated using [56]:

$$T_{fsw} \approx -0.003 - 0.0527S_0 - 0.00004S_0^2 \tag{1.1}$$

Where T_{fsw} is the freezing point of the seawater(°C) and S_0 is the salinity of the ocean(PSU). Cooling on the surface of the ocean causes the density of top layer seawater to increase. Vertical density instability leads to convective overturning in which warmer seawater underneath flows to the surface. Therefore, the surface of the ocean will normally not start to freeze until the entire water column (around 20 m) reaches its freezing point. When the ambient temperature falls below -1.86°C, the freezing point for seawater at 34 PSU, needle-like ice crystals with a mean thickness of a few centimeters called frazil ice starts to form.

Reaching the critical size, each frazil crystal starts developing dendritic surfaces through the solute build-up. Frazil ice in the turbulent ocean tends to collide into a cluster of crystals. During melting season, the Antarctic ice shelve produces a large volume of frazil ice which contributes to ice shelves, and coastal sea ice [50]. Around 10 – 30% of loose frazil crystals consolidate into the granular ice. Such process has been attributed to downward freezing of voids and change of morphology of frazil crystals [62]. Maus & De la Rosa [52] and Naumann et al. [55] illustrated the consolidation of frazil mesh by convective overturning and gradual freezing of pore spaces as part of desalination process.

1.2.2 Stages of ice growth

Under quiescent conditions, the grease ice will form a continuous ice sheet up to 10 cm called nilas. There are two types of nilas: dark nilas with thickness less than 5cm and light nilas with thickness between 5 and 10 cm. Nilas is very saline with bulk salinity up to 100 PSU

[51]. Agitation and convective overturning lead to the gradual removal of salt, allowing for the progressive downward freezing of the interstitial brine and accretion of the frazil ice to pancake ice floes. The diameter of pancake ice ranges from 20 cm to 3 m. The pancake ice bumps against each other and congeals into a continuous large sheet of ice by growing nilas in between. Freezing of randomly oriented frazil ice results in granular ice at the top-most 0.3-0.5 m of sea ice. Columnar ice usually forms underneath the granular ice. Young ice has a thickness between 10 cm and 30 cm, which includes grey ice (10 cm-15 cm) and grey-white ice (15 cm-30 cm). First-year white ice has a thickness greater than 30 cm, and old ice refers to the ice that survives through the summer [62].

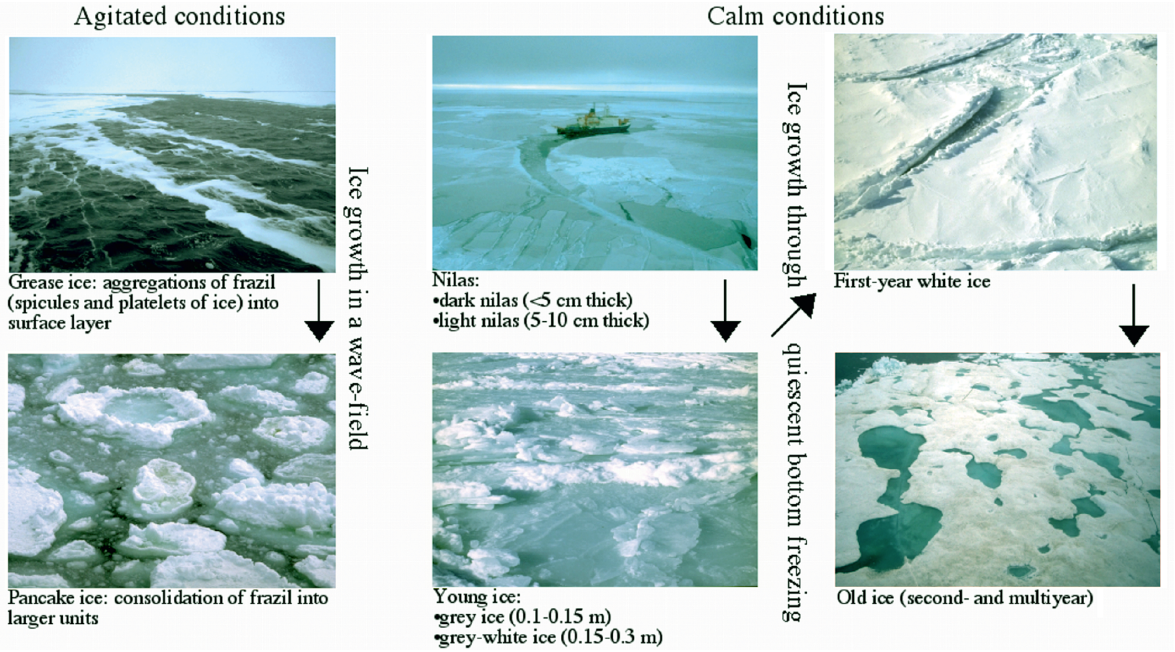

Figure 1.2: Flow diagrams showing stages of ice growth [62].

1.3 Columnar ice microstructure

1.3.1 Supercooling

As ice freezes downward, brine leaves the ice. Thus, higher salinity at the ice-water interface leads which enhances salt diffusion away to the ocean. According to Equation 1.1, high salinity decreases the freezing temperature of seawater. The diffusion of salt towards the ocean is slower than diffusion of heat. That results in the freezing temperature determined from the salinity being higher than the actual temperature of seawater. The actual temperature profile is linear, while the salinity-determined freezing point is exponential, as illustrated in Figure

1.3. The profile discrepancy leads to a brine layer just underneath the ice bottom being cooled below its freezing point. Such a phenomenon is often referred to as constitutional supercooling [32]. Meanwhile, the movement of salt via convection is increased when the high salinity brine is in contact with the ice surface. [88]. Regardless, the transport of salt is still slower than the diffusion of heat.

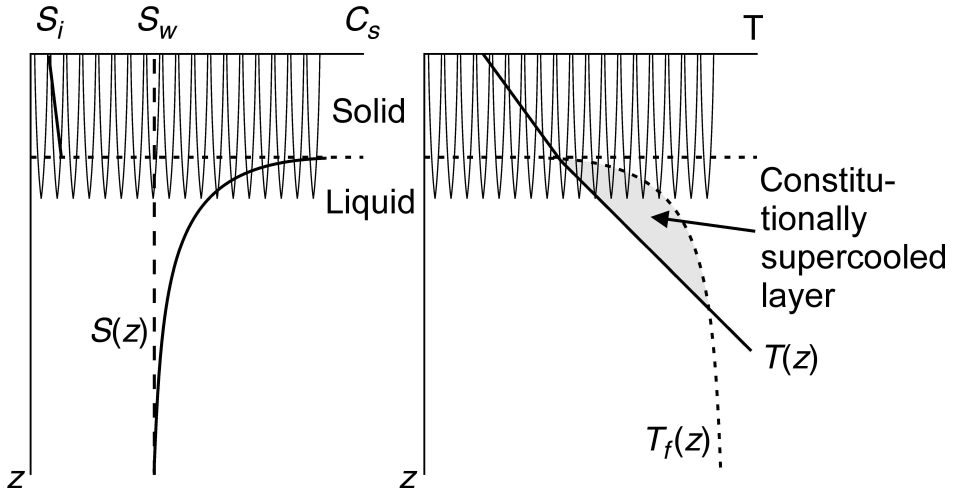

Figure 1.3: Schematic of the lamellar ice-water interface (skeletal layer) and the corresponding salinity (left) and temperature(right) gradients. The freezing temperature profile is shown as a dashed line at right, with a constitutionally supercooled layer bounded by the actual temperature gradient and the salinity-dependent freezing-point curve [62].

1.3.2 Geometric selection

As a result of supercooling, the ice will gain a growth advantage with any small protrusion into the supercooled region. When the grease ice formed at the surface of the ocean, the crystal orientation was initially random [83]. However, as mentioned earlier, the growth rate along the basal plane is up to two order magnitudes higher than off basal planes. The ice lamellae that are tilted vertically have a growth advantage over ice lamellae that tilted more to the horizontal. Therefore, the number of crystal grains with vertical ice lamellae (horizontal c-axis) increases dramatically as ice thickens. The process is called geometric selection. Furthermore, the horizontal c-axis can incorporate azimuthal alignment [83] caused by the shear current underneath the ice interface. The ice lamellae with the c-axis parallel to the direction of the current gain growth advantage [49] from enhanced solute diffusion induced by turbulence [10]. Both processes together result in the dominant presence of vertical lamellae in columnar ice. Columnar ice comprises very thin (around 0.4-1mm) vertically aligned ice lamellae parallel to the heat flow. The brine is incorporated between the ice lamellae, acting as planes of weakness [76]. Nakawo and Sinha [54] found decreasing in growth rate to the greater width of ice lamellae for Arctic ice, causing less brine to get trapped. The isolated brine inclusions are often elliptical, and they generally interconnect laterally as ice lamellae

lengthen [21]. Figure 1.4 illustrates the main ice textures, growth conditions, and timescales, and typical winter temperature and salinity profiles for first-year sea ice [62].

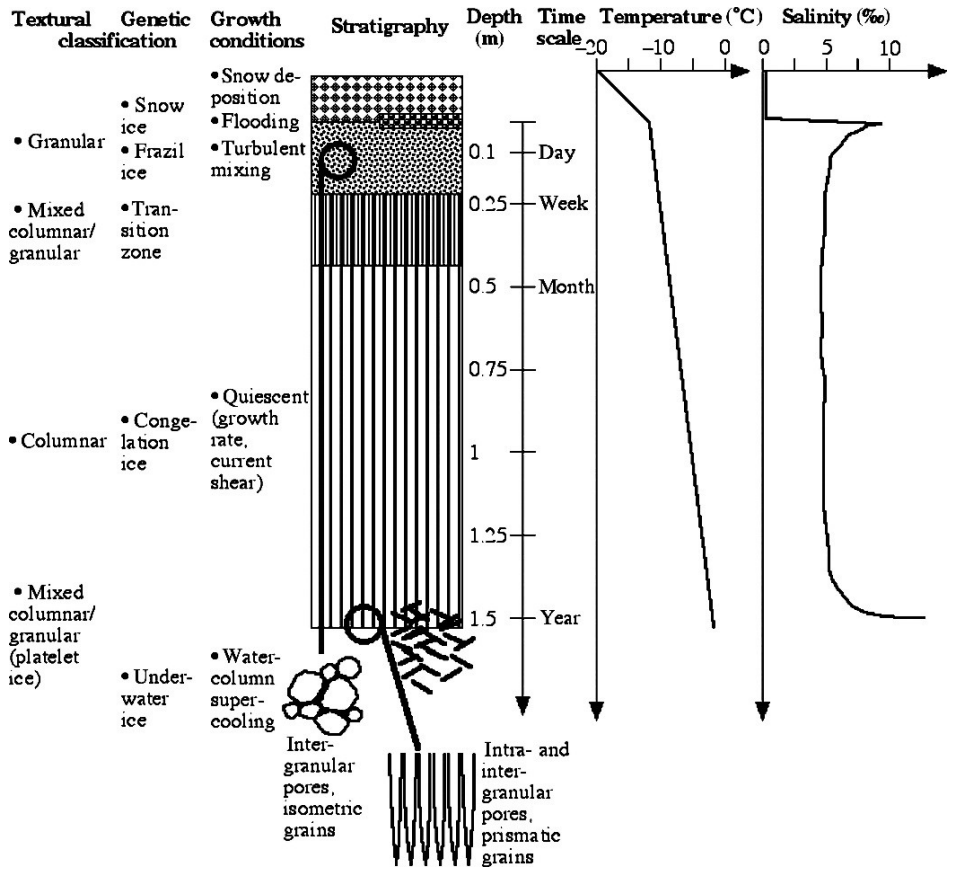

Figure 1.4: Schematic summarizing the main ice textures, growth conditions and timescales, and typical winter temperature and salinity profiles for first-year sea ice [62].

1.3.3 Skeletal layer

The bottom centimetres of the sea ice is the skeletal layer with porosity around 30% and very low mechanical strength. A substantial convective overturning of brine and desalination occurs in this region. The consolidation of the skeletal layer is described by the phase diagram in Figure 1.5. As the ice becomes more substantial, the temperature of the skeletal layer decreases, together with the thickening of the parallel lamellae. The lamellae eventually connect by forming bridges and consolidating into an interconnected sea ice. Brine is lost as the sea ice consolidates, while the fundamental crystal arrangement is retained during the ice growth. Ice grown without externally imposed current displays lamellae crystal structure while ice grown in current has the grain substructure [62].

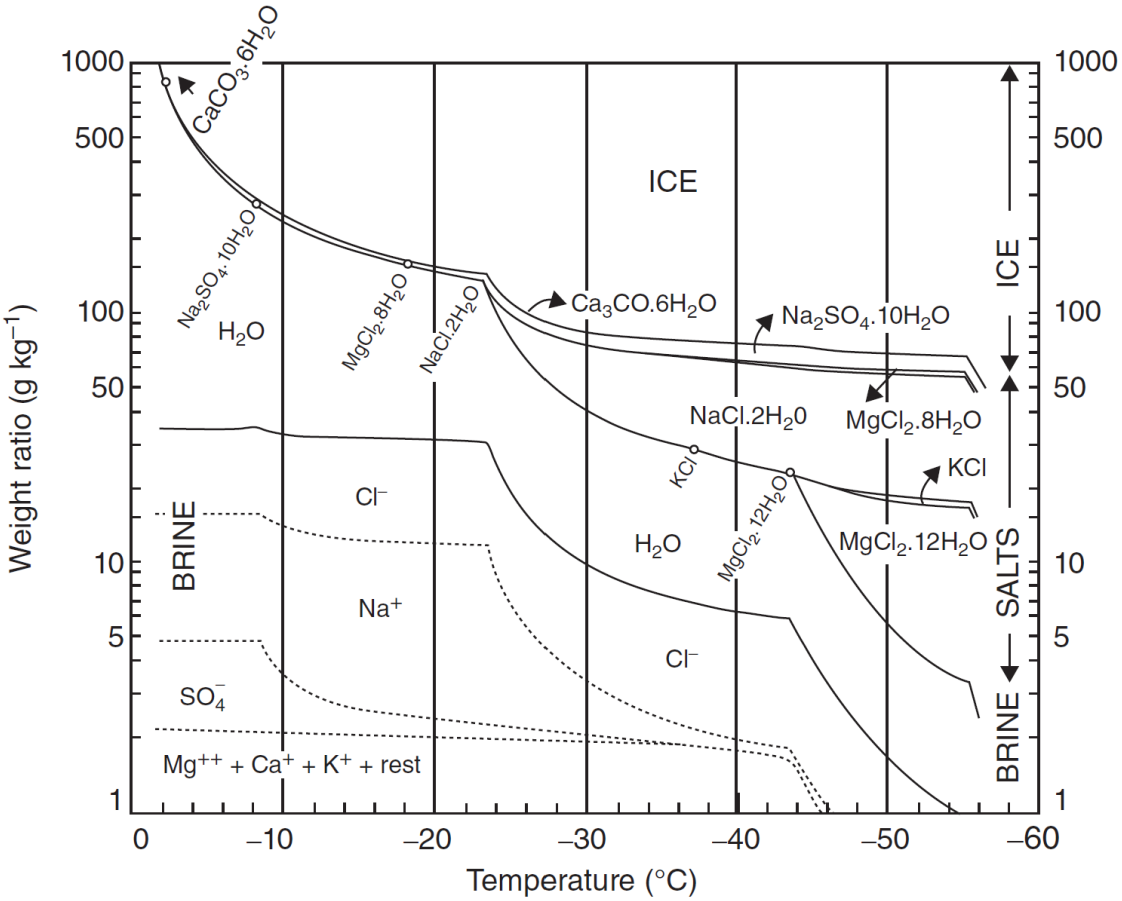

Figure 1.5: Phase diagram of sea ice from Assur (1960). The different curves indicate the mass fraction of solid ice (top), salts (middle)and liquid brine (bottom) present in a closed volume of standard seawater at different temperatures [62].

1.4 Sea ice salinity

1.4.1 Bulk salinity and brine movement

Ice salinity (S_i) refers to the fraction by weight of the salt in a unit mass. The unit is in per thousand or Practical Salinity Unit (PSU). Ice salinity measurement is usually done by taking an ice core sample and melting it in an air-tight container. Once the ice melts, the melt solution is measured with a salinometer for electrical conductivity. The ice salinity is obtained according to the conductivity and temperature. The speed is crucial in the salinity measurements since brine begins to drain once it is extracted from the field [76].
The method mentioned above measures the bulk salinity of the ice sample. In sea ice, normally, there is variation in salinity with depth. The depth dependence on the salinity happens when salts migrate downward through the ice during the freezing period [16]. Nevertheless,

the bulk salinity still gives the first insight into the salinity profile of the ice. Cox and Weeks [13] found a consistent correlation between bulk salinity (S_i) and ice thickness (h_i). Kovacs [44] then conducted more extensive experiments and came up with an empirical equation that relates the ice thickness and average salinity.

$$S_i = 5.369 + \frac{1646.132}{h_i^2} \tag{1.2}$$

Nakawo & Sinha [53] observed that steady-state bulk salinity is correlated to the ice growth rate. The equation from Petrich et al. [64] produced a good fit between growth rate and bulk steady-state salinity using data from Barrow, Alaska, 2008 as shown in Figure 1.6.

$$\frac{S_i}{S_0} = 0.14 \left(\frac{v}{1.35 \times 10^{-7}} \right)^{\frac{1}{3}} \tag{1.3}$$

Where S_i is the bulk salinity of ice, S_0 is the salinity of the ocean, and v is the growth rate of ice (m/day). It has been shown that the bulk salinity is well reproduced between 0.65 and 1.1 m.

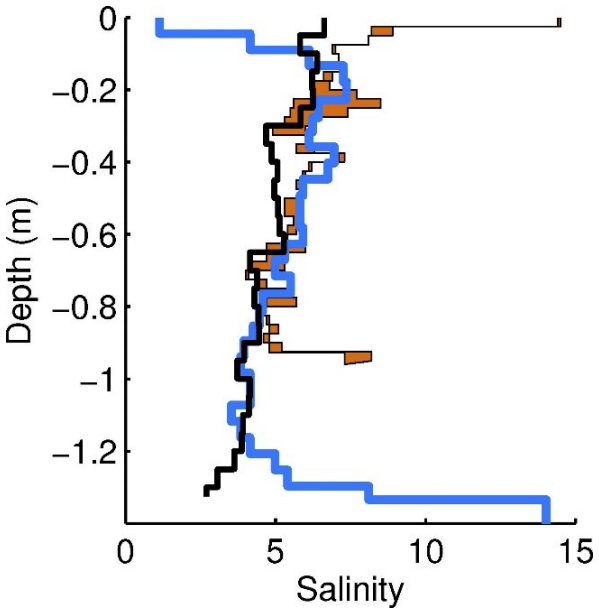

Figure 1.6: Bulk salinity profiles measured in Barrow, Alaska at the end of May (thick line), and two profiles measured 2 m apart in early February (thin lines, difference between profiles is shaded). The solid black line is the expected bulk salinity from Equation 1.3 [62].

The brine salinity at the top section of the sea ice is higher owing to low ice temperature. As brine flows downloads, the bulk salinity increases locally, which melts nearby ice to maintain thermodynamic equilibrium, forming brine channels. The melting of local ice by the super-heated brine from above is necessary to maintain thermodynamic equilibrium. Brine plumes are evident in the underlying seawater as brine leaves through brine channels [81, 30]. Due to

conservation of mass, the mass of brine entering the ice is equal to the mass of brine leaving the ice (neglecting density difference). The upward flow of brine is part of the process in brine channel formation [90] which reduces the local bulk salinity and porosity. The inflow and outflow of brine lead to the convective overturning, and the salinity difference causes the net desalination of the sea ice. Overall, desalination only happens at the bottom-most centimeters of the sea ice, possibly around 5 cm during winter and up to 10 – 20 cm during spring [63].

1.4.2 Desalination processes

Brine diffusion

Brine diffusion is a diffusive process first applied in sea ice by Untersteiner [77]. During winter, atmospheric temperature is significantly lower than seawater, causing a temperature gradient throughout the ice. To maintain thermodynamic equilibrium, salinity will vary in response to the temperature gradient. That results in the brine salinity in ice at the upper portion being higher than the lower portion. The salinity gradient will cause salt diffusion, which results in a gradual descent into the brine pocket. Eventually, some of the brine might leave the ice-ocean interface. However, both empirical and experimental studies show that the velocity of the downward diffusion is minimal to incur a substantial loss of salt from the ice [42, 34, 70]. Untersteiner [77] estimated the downward movement of brine is around 2 cm during winter, which is almost balanced by the upward diffusion as temperature rises.

Brine expulsion

Pure ice has a density about 10% lower than brine. As a result, as the local temperature inside the brine pocket varies, the volume of the brine pockets changes as well. The shift in brine volume results in the formation of a pressure gradient, which pushes the brine upwards or downwards. Bennington was the first to describe this brine drainage technique [5]. During winter, the temperature throughout the ice is lowered, leading brine to move downwards. However, Cox & Weeks [11] found that brine outflow cannot account for changes in sea ice salinity and that the primary contribution to sea ice desalination occurs during the early stages of sea ice development.

Gravity drainage

Two processes happen during the gravity drainage. First, sea ice has a lower bulk density than saltwater, resulting in increased freeboard as ice thickens. The freeboard height generates a hydrostatic head that drives brine downward through brine channels [22]. Such processes,

together with flushing, are the main contributors to low bulk salinity at the upper portion of multi-year ice [13].

During winter, the temperature is substantially lower in the top portion of sea ice than it is in the lower portion of sea ice. Thus, the brine density at upper section of the ice is highest, which results in the convective overturning of brine in the skeletal layer and exchange brine with underlying seawater [60]. Cox & Weeks [11] found a positive correlation between gravity drainage and increased temperature or density gradient. The brine flow within the brine channels is often oscillatory with an observed oscillation period of an hour made up of 8-15 minutes of inflow, and 45 minutes of outflow for 10 cm sea ice [22]. The mechanism of oscillatory motion is based on the density differential between brine and underlying ocean, in which seawater's buoyancy force interacts against the denser brine. A delicate equilibrium between these forces is achieved from the narrowing of brine channels that makes oscillation of brine flow possible.

Wettlaufer et al. [84]discovered that there is no salt loss from ice owing to gravity drainage until a certain thickness is achieved in their laboratory studies. This phenomena was described in terms of the mushy layer's Rayleigh number as shown in Equation 1.4.

$$Ra = \frac{gh\rho_{oc}\beta(S_{br} - S_{oc})\Pi(V_b)}{\mu\kappa} \tag{1.4}$$

Where h [m] is the thickness of the mushy layer, positive upward from ice bottom; g [ms^{-2}] is the acceleration due to gravity; ρ_{oc} is the density of seawater, taken as 1027 kgm^{-3}; β is the haline contraction coefficient; taken as 0.79×10^{-4} kgg^{-1}; S_{br} and S_{oc} [PSU] are the brine and ocean salinity respectively; $\Pi(V_b)$ [m^2] is ice permeability as function of brine volume and is calculated in accordance with Equation 2.4; κ is thermal diffusivity, taken as 1.2×10^{-7} ms^{-2} and μ is the dynamic viscosity of the liquid, taken as 2.55×10^{-3} kgms^{-1}.

Notz, Dirk and Worster, M. [60] conducted a tank experiment where 34 PSU NaCl solution with an initial temperature of -1°C was cooled from the top at a constant temperature of -10°C over 48 hours. The permeability of the NaCl ice was calculated using Equation 1.16. The local maximum salinity appears at around 8 cm as shown in Figure 1.7a. The shape of the salinity profile in Figure 1.7a resembles the figure of maximum Rayleigh number as shown in Figure 1.7c. For very thin ice, potential energy calculated by $g\Delta\rho h\beta$ is too little to surpass the dissipative effects caused by thermal diffusion κ and viscosity μ/Π. That explains why a critical thickness needs to be reached before gravity drainage can occur. Rayleigh number encapsulates a variety of phenomena, including initial gravity drainage delay and the development of numerous C-shaped salinity profiles.

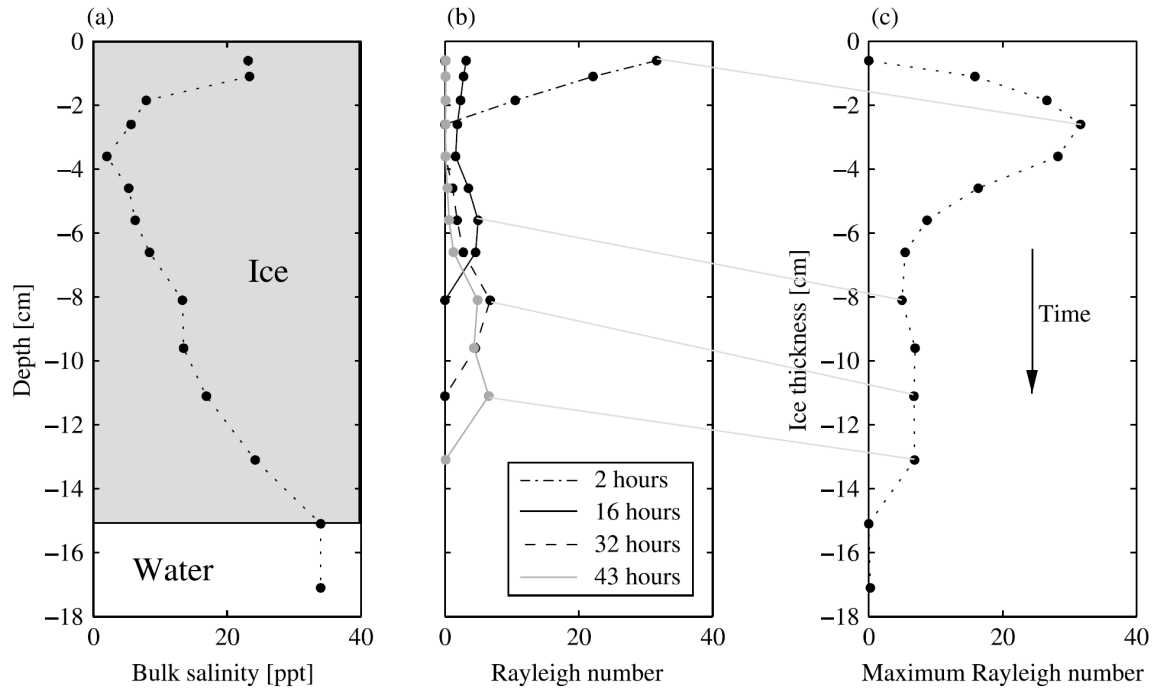

Figure 1.7: (a) Bulk salinity profile at the end of an experiment in which a NaCl solution with a concentration of 34 ppt was cooled from above with a constant temperature of $T_s = -10°C$. (b) Rayleigh number profiles at various times during the experiment. (c) Maximum Rayleigh number as a function of ice thickness as it evolves in time [60].

Flushing

Flushing is the main contribution to the desalination of the sea ice during summer. A surface melt pond formed due to increasingly higher temperature. The melt pond created a pressure overhead to drive the meltwater downward to "flush" out brine through brine channels and drastically reduce the bulk salinity of the sea ice. The magnitude of flushing can be quantified by Darcy's law. Notz, Dirk and Worster, M. [60] made a simple one-dimensional model to analyse the effect of flushing. The model only accounts for the vertical component of flushing and neglects the horizontal component. The duration of the simulation was one hour.

The model set-up is as follows. The permeability of the sea ice using equation 1.16. The sea ice is initially 0.9 m thick with a bulk salinity of 10 PSU, and the temperature increases linearly from -1.8°C at the ice-ocean interface to roughly -0.5°C at the melt pond interface. Meltwater has a temperature of 0°C and salinity of 0.5 PSU. The seawater under the sea ice is -1.8°C and has a salinity of 34 PSU.

Figure 1.8 shows the initial and final states of temperature, solid fraction, and salinity profiles.

At the finish of the simulation, the melt pond was almost completely drained and the bulk salinity of ice was lowered by more than 2 PSU. Downward percolation of meltwater also increased the temperature of ice throughout its entire thickness while the solid fraction almost remained constant.

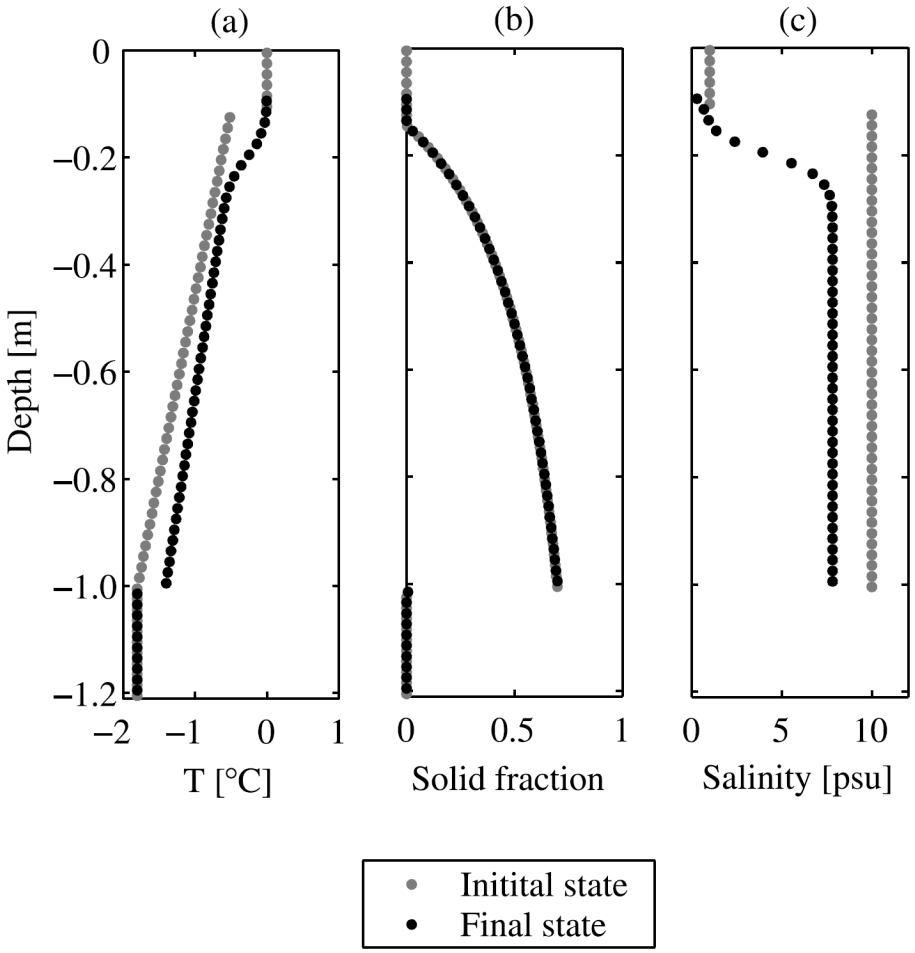

Figure 1.8: Vertical profiles of (a) temperature, (b) solid fraction, and (c) bulk salinity before and after a 1-hour model run with flushing [60].

1.4.3 Salinity in the old ice

Cox & Weeks [13] conducted salinity investigations for old ice at various Arctic and subarctic locations. The salinity distribution in old sea ice is highly variable and can be influenced by the ice topography which cannot be accurately characterized by a single average profile. Salinity profiles of melt hummocks demonstrated a consistent rise in salinity with depth, from 0 PSU at the top to about 4 PSU at the core bottom, as shown in Figure 1.9. In contrast, salinity profiles for melt depressions displayed significant irregular variations with salinity

values up to 6.3 PSU as shown in Figure 1.10. The depression profile's average salinity (3.9 PSU) is much more than that of the hummock profile (2.6 PSU). Low salinity (close to 0 PSU) at the upper portion of the hummocks may be due to flushing. The gravity-driven drainage forced the brine to drain through interconnected brine channels and pockets. Hydrostatic head produced by melt pond overcomes the capillary forces within the brine pockets. As a result, the salinity of the top layer of the ice is proportional to its freeboard height. Figure 1.11 demonstrates a substantial association between the average salinity of the top meter of ice and its freeboard height (r = 0.88). It also gives a possible explanation of why salinity profiles for melt depression showed large variations.

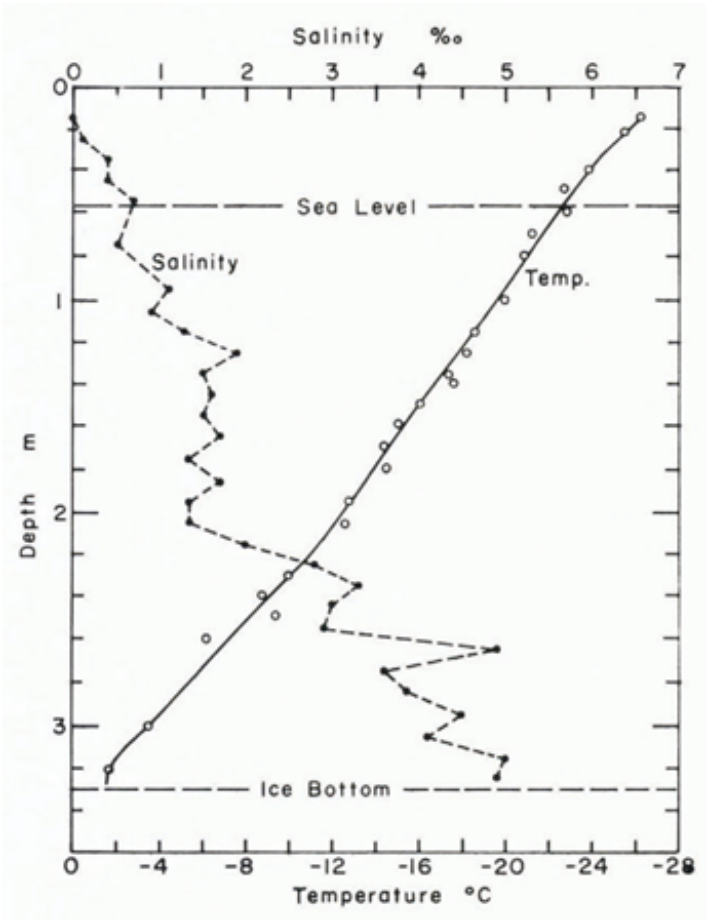

Figure 1.9: Typical hummock salinity profile (profile S1) and temperature profile [13].

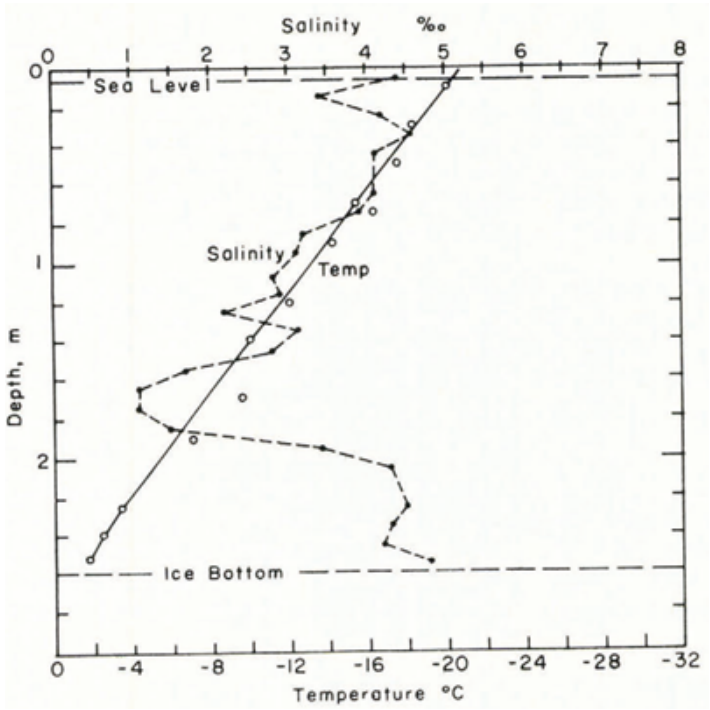

Figure 1.10: Depression salinity S5b and temperature profile [13].

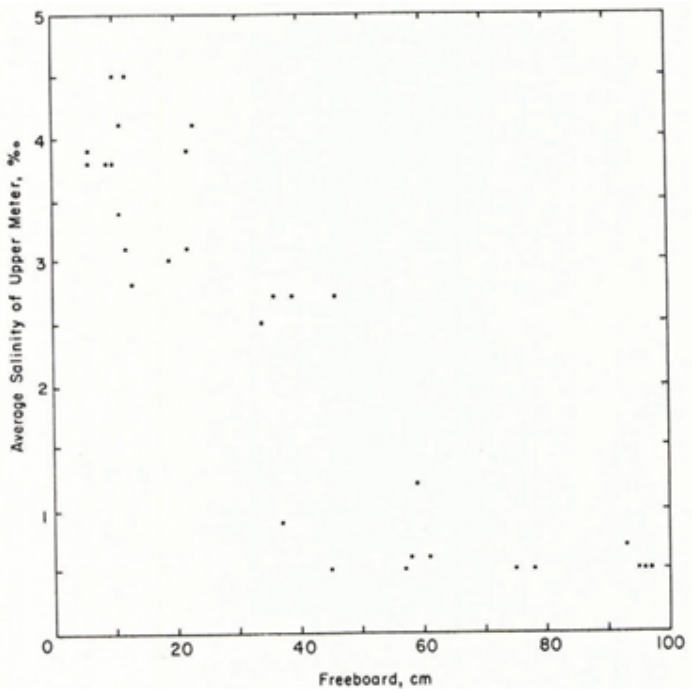

Figure 1.11: Plot of average salinity of the upper meter of the ice versus the freeboard height [13].

Salinity measurements taken from sea ice of various thicknesses and ages revealed a substantial connection between the average salinity S and the ice thickness h as shown in Figure 1.12. Two linear equations may be used to depict the salinity profile of ice samples obtained at the end of the growth season:

$$S = 14.24 - 19.39h(h = 0.4m); S = 7.88 - 1.59h(h > 0.4m) \tag{1.5}$$

At 0.4m, there is a difference in salinity slope, which may be owing to the major brine drainage mechanism shifting from brine expulsion to gravity drainage. Linear regression was also applied to melt ice and gives a single linear equation:

$$S = 1.58 + 0.18h. \tag{1.6}$$

Thus, it demonstrates that there are annual cyclic variations in average salinity in old ice. At the end of the growth (cold) season, the average salinity is highest, and at the end of the melt season, it is lowest. Such a phenomenon can be explained concerning brine drainage. During melt season, the sea ice deteriorates, and brine pockets start to melt, which incur considerable brine drainage. Additionally, during the growth season, the brine cavities at the bottom freeze, resulting in a maximum salinity.

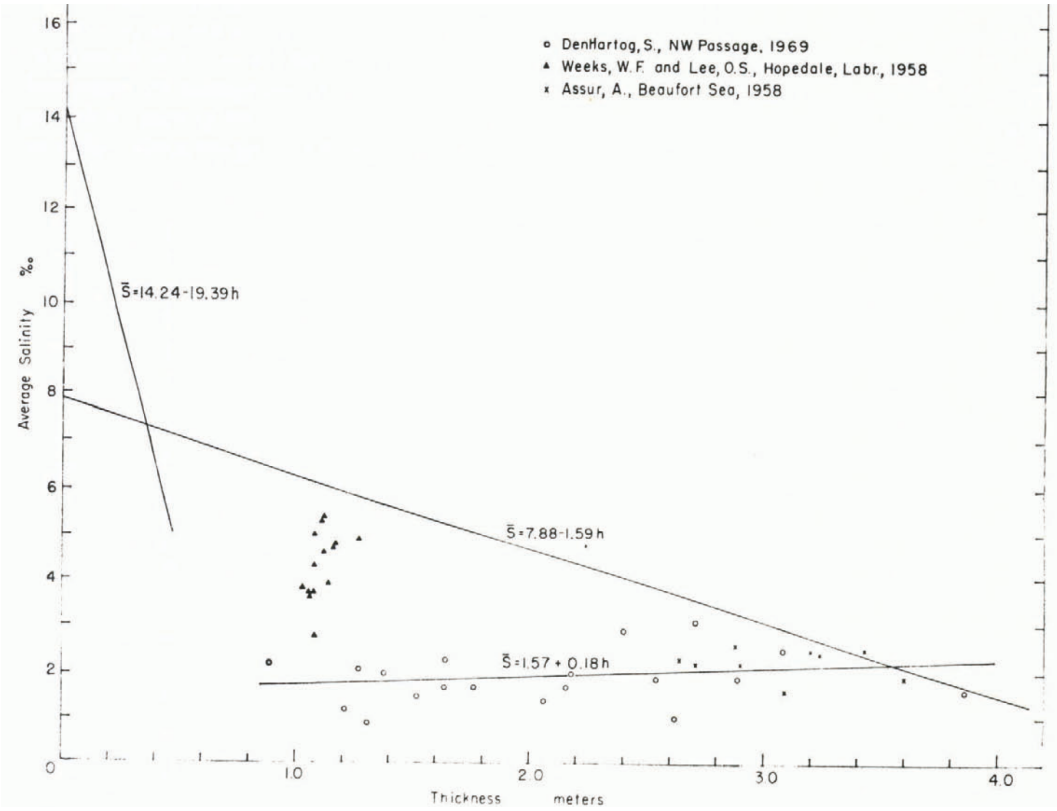

Figure 1.12: Average salinity of sea ice as a function of ice thickness for warm sea ice sampled during or at the end of the melt season [13].

Kovacs [44] also proposed an empirical equation for estimating the salinity of multi-year ice from floe thickness (h_{Fi}):

$$S_i = 1.85 + (\frac{80217.9}{h_{Fi}^2}) \tag{1.7}$$

Where the floe thickness is in cm, and the upper limit is 900 cm. However, there is a greater scatter in measured data compared to first-year ice (correlation coefficient, r^2 for multi-year ice salinity estimation is 0.22 compared to 0.73 found in the first-year ice) [13].

1.5 Sea ice porosity

The total porosity (V_T) of sea ice can be expressed as brine volume (V_b) and air volume (V_a). The brine volume is the liquid contained inside the ice. Frankenstein and Garner [24] proposed a set of equations that relates the temperature and salinity to the brine volume. Note that these equations do not apply for the ice during the spring period (i.e. decaying ice) or old ice since the majority of the salt within the ice has been drained already, thus leading to much lower salinity ranging between 0.5 to 2 PSU.

$$\frac{V_b}{V} = \frac{1}{1000} S_i \left(\frac{52.56}{|T|} - 2.28 \right) for -0.5°C \geqslant T \geqslant -2.06°C \tag{1.8}$$

$$\frac{V_b}{V} = \frac{1}{1000} S_i \left(\frac{45.917}{|T|} + 0.930 \right) for -2.06°C \geqslant T \geqslant -8.2°C \tag{1.9}$$

$$\frac{V_b}{V} = \frac{1}{1000} S_i \left(\frac{43.795}{|T|} + 1.189 \right) for -8.2°C \geqslant T \geqslant -22.9°C \tag{1.10}$$

There is another less accurate but covers the temperature between $-0.5°C \geqslant T \geqslant -22.9°C$:

$$\frac{V_b}{V} = \frac{1}{1000} S_i \left(\frac{49.185}{|T|} + 0.532 \right) \tag{1.11}$$

Where $\frac{V_b}{V}$ is the brine volume (-), S_i is the bulk salinity (PSU) and T is the temperature (°C).

Cox and Weeks [15] proposed a more sophisticated temperature-dependent method based on experimental results to estimate the brine and gas volume.

$$\frac{V_b}{V} = \left(1 - \frac{V_a}{V} \right) \frac{(\rho_i/1000) S_i}{F_1(T) - (\rho_i/1000) S_i F_2(T)} \tag{1.12}$$

Where $\frac{V_b}{V}$ is the brine volume (-); V is the bulk volume (m^3); V_a is the air volume (m^3); ρ_i is the density of pure ice: ρ_i = 917 - 0.1403T (kgm^{-3}); S_i is the bulk salinity (PSU) and

F_1, F_2 are the empirical functions of temperature. $F_1(T)$ and $F_2(T)$ are empirical polynomial functions $F_i(T) = a_i + b_i T + c_i T^2 + d_i T^3$, based on the phase relations. The coefficients for different temperature intervals are listed in Table 1.1.

Table 1.1: For functions $F_1(T)$ and $F_2(T)$ for different temperature intervals [15].

T, °C	a_1	b_1	c_1	d_1
$0 \geq T > -2$	-0.041221	-18.407	0.58402	0.21454
$-2 \geq T \geq -22.9$	-4.732	-22.45	-0.6397	-0.01074
$-22.9 > T \geq -30$	9899	1309	55.27	0.7160
T, °C	a_2	b_2	c_2	d_2
$0 \geq T > -2$	0.090312	-0.016111	1.2291×10^{-4}	1.3603×10^{-4}
$-2 \geq T \geq -22.9$	0.08903	-0.01763	-5.330×10^{-4}	-8.801×10^{-6}
$-22.9 > T \geq -30$	8.547	1.089	0.04518	5.819×10^{-4}

Brine salinity S_{br} is obtained from the empirical polynomial function (Equation 1.13) using the coefficients from Table 1.2.

$$S_{br} = a_3 + b_3 T + c_3 T^2 + d_3 T^3 \tag{1.13}$$

Table 1.2: Coefficients for functions $F_1(T)$, $F_2(T)$ and $F_3(T)$ for different temperature intervals [14, 15].

T (°C)	a_3	b_3	c_3	d_3
$0 \geq T > -2$	–0.031 6891	–18.3801	0.327 828	0.213 819
$-2 \geq T \geq -22.9$	–3.9921	–22.700	–1.0015	–0.019 956
$-22.9 > T \geq -30$	206.24	–1.8907	–0.060 868	–0.001 0247

The air volume fraction is usually considered negligible except for in snow ice where the air fraction will be significant. Nevertheless, Cox and Week [15] also derived the formula for estimation of air volume fraction from experimental data:

$$\frac{V_a}{V} = 1 - \frac{\rho}{\rho_i} + \rho S_i \frac{F_2(T)}{F_1(T)} \tag{1.14}$$

Where $\frac{V_a}{V}$ is the air volume (-); ρ_i is the density of pure ice: (kgm^{-3}); ρ is the density of sea ice (kgm^{-3}); S_i is the bulk salinity (PSU) and F_1, F_2 are the empirical functions of temperature as shown in Table 1.1.

Sea ice decays rapidly during spring once temperature increases which results in reducing ice

thickness and strength. When the air temperature falls below -8°C, the bulk of the solid salt in sea ice melts into the liquid form. As the ambient temperature continues to rise, the brine pockets within the ice quickly enlarge and interconnect each other to form brine channels. The brine channels dramatically increase the ice permeability. [18] and help to drain brine solution resulting in desalination of ice [46, 8]. Higher temperature frequently results in the surface pond, which makes the ice cover thinner and weaker.

There is no complete quantitative analysis of the evolution of pore microstructure during freezing and melting despite its importance. Nevertheless, Petrich, Chris and Eicken, Hajo [62] have attempted to explain it by linking the observations to the hypotheses to understand the general process in a piecemeal manner and discussed the desalination process of columnar ice during freezing. Columnar ice consists of thin vertical sheets of ice blade called ice lamellae. The spacing of the ice lamellae is around 0.3-0.5 mm. Figure 1.13 shows the images of brine layers with respect to the temperature. The lamellae develop and extend as the temperature drops, releasing the salt from the ice. Additionally, the lamellae interact by producing bridges with porosities ranging from 0.1 to 0.3.

During the melt season, the most prevalent mode of brine migration is the flushing of surface meltwater [77]. Hydrostatic pressure caused by meltwater may result in vertical and lateral movement through the ice, and up to 25% of meltwater produced annually can be stored within the ice cover. Thus, on multi-year ice, this desalination process results in exceptionally low bulk salinity. (typically around 2-3 PSU).

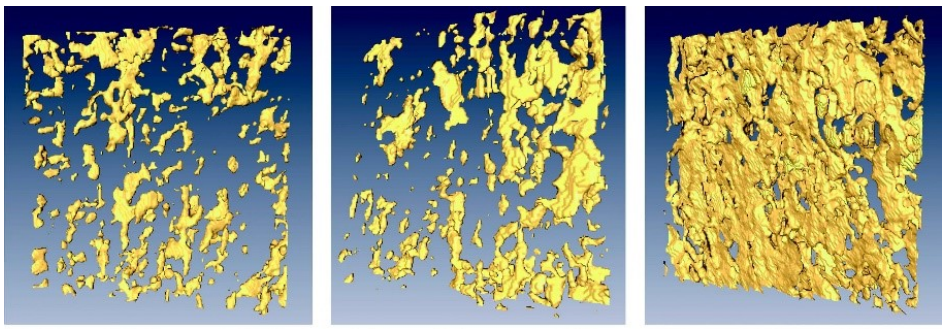

Figure 1.13: X-ray microtomography images of brine layers in sea-ice single crystals as a function of temperature [28].

1.6 Permeability of sea ice

1.6.1 Darcy's law

Fluid passing through sea ice encounters resistance owing to both micro obstructions in the flow route (which contribute to the tortuosity of the flow path) and viscous drag along the pore walls. The reciprocal of resistance is permeability Π, measured in m^2. The flux q through a homogeneous flow through homogeneous porous medium can be expressed by Darcy's law assuming the flow is laminar [62]. Where μ is the dynamic viscosity(Pa.s); $\frac{\partial p}{\partial x}$ is the pressure gradient in the direction of the flow; Π is the intrinsic permeability (m^2) and q is the flow flux ($m^3 s^{-1} m^{-2}$).

$$q = \frac{-\Pi}{\mu} \frac{\partial p}{\partial x} \tag{1.15}$$

1.6.2 Porosity-permeability relation

Sea ice permeability is directly proportional to its porosity or brine volume. Freitag [25] proposed an empirical permeability–porosity relationship for growing sea ice from the lab experiment. Where Π is the intrinsic permeability(m^2) and V_b is the brine volume(-).

$$\Pi = 10^{-17} (10^3 V_b)^{3.1} \tag{1.16}$$

On the other hand, Golden et al [28] introduced a permeability–porosity relationship based on the effective medium theory assuming spherical grains.

$$\Pi = 3 V_b^3 \times 10^{-8} \tag{1.17}$$

Petrich and Eicken [62] introduced a porosity-permeability relation. Where Π intrinsic permeability(m^2); Π_0 Permeability constant, taken as 2×10^{-8} for anisotropic sea ice or 10^{-8} for isotropic sea ice(-) and V_b brine volume(-).

$$\Pi = \Pi_0 \times {V_b}^3 \tag{1.18}$$

Furthermore, the permeability of sea ice is generally directional dependent. The permeability in the vertical direction can be up to 2 order magnitudes higher than in the lateral direction [38].

1.7 Measurement of sea ice permeability

1.7.1 Liquid permeability of the sea ice

Bail test

The bail test is a typical in-situ test in measuring the permeability of sea ice. The thickness of the ice is measured before drilling a 115 mm diameter hole into the ice and sealing it with PVC pipe (P) to prevent lateral movements of water as shown in Figure 1.14. The rising of the floater (F) is continuously recorded to plot the head versus time graph. The laminar flow through a porous media is defined by Darcy's law as shown in Equation 1.15. Assuming the specific discharge is linearly proportional to the applied force, the recovery curve can be derived by applying Darcy's law. The experimental data is then fitted through the exponential curve of Equation 1.19. The permeability can be extrapolated from the exponent of the exponential curve [41].

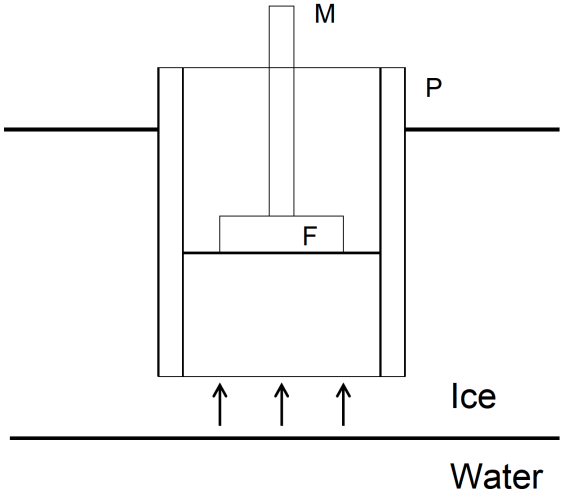

Figure 1.14: Schematic drawing of experimental set-up of permeability measurement. P: PVC pipe, F: floater, M: ruler used to measure the height of water level [41].

$$h(t) = h(t_0)e^{(-\Pi g\rho/\mu L)t} \tag{1.19}$$

Where $h(t_0)$ is the initial hydraulics head (m); Π is the intrinsic permeability (m^2); g is the acceleration due to gravity(m/s^2); ρ is the density of the fluid (kg/m^3); μ is the dynamic viscosity of fluid ($kgm^{-1}s^{-1}$) and L is the thickness underneath the borehole (m).

Falling head test

For this thesis, the high-density snow permeameter is shown in Figure 1.15 [45]. Kerosene was chosen liquid for the test. The hydraulic conductivity k can be calculated by:

$$k = \frac{2.3dA'}{tA} log_{10}\left(\frac{H_1}{H_2}\right) \tag{1.20}$$

Where A' is the internal area of the tube (mm^2); A is the area of the ice core sample (mm^2); H_1 is the initial head (mm); H_2 is the final head (mm); t is the duration of the experiment (s) and d is the thickness of the ice core sample (mm).

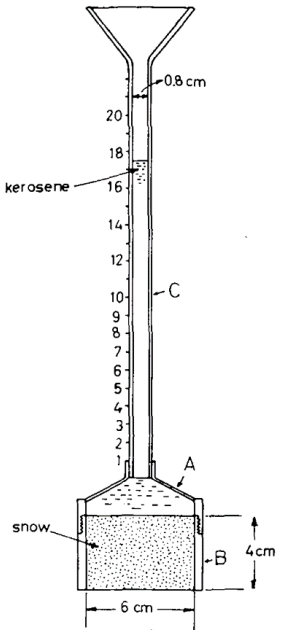

Figure 1.15: Falling head permeameter [45].

Bail test is the most common technique in measuring sea ice permeability [65, 18, 26] with no sophisticated equipment required. However, there are two limitations associated with the bail test. Firstly, since the bail test measures the inflow rate of water approaching sea level, it is impossible to measure sea ice permeability above sea level. Furthermore, the borehole needs to be at a sufficient depth below sea level to allow inflow rate measurement at satisfactory accuracy, further reducing measurable thickness. For example, the shallowest borehole that Eicken et al. [65] conducted his bail test was 25 cm. Secondly, permeability measurement of an intermediate ice layer cannot be achieved since ice thickness is measured from the ice bottom to the bottom of the borehole. The falling head test does not have the limitations mentioned above, but it has its constraints. Firstly, extracting core samples from the ice sheet and cutting cores into the required dimension will inevitably introduce brine drainage.

By comparing other non-destructive measurements, Notz et al. [58] found underestimation in bottom ice salinity ranging from 1 to 5 PSU. Secondly, the core samples are cooled as they are extracted from the ice sheet, resulting in underestimating brine volume and permeability. Combining both measuring methods could lead to a more comprehensive understanding of sea ice permeability.

1.7.2 Air permeability of ice

Traditionally, a single-tube sample holder is used to perform a gas permeability test. However, such a sample holder has the inherent disadvantage of causing leakage along the wall of the sample holder. To resolve such an issue, Shimizu [69] designed a gas permeameter for snow testing, which includes a double-cylinder sample to account for the edge effects as shown in Figure 1.16 [3]. The double-cylinder sampler holder consists of an inner and outer cylinder, each attached to a pressure transducer and connected to a vacuum compressor. The flow rate can be adjusted with the flow meter connected to the inner cylinder. Once the vacuum compressor starts, the air flows through the snow sample from the bottom of the sample holder. Ideally, the pressure measured by the inner and outer cylinder should be identical. However, due to the leakage flow at the inner cylinder's wall, the pressure at the inner and outer cylinder will be different. To compensate for the edge effect, the flow meter is used to adjust the airflow of the inner cylinder until the inner and outer pressures are matched.

Albert and Perron [2] modified the double-cylinder sample holder to make it suitable for ice layers. The holder, in particular, included an interior wall made of an inflated rubber membrane. After inserting the ice sample, fitting the double-cylinder head onto the ice sample from above, and fitting a cylindrical spacer ring below the sample, the rubber membrane was inflated to produce a form-fitting seal with the perimeter of the ice sample, enabling airflow solely through the ice sample. Then, using Darcy's law, the air permeability of the ice layer is calculated using the recorded flow rate and pressure differentials. By Darcy's law, the resulting permeability should be a straight line on the plot of flow rate vs pressure drop. Only linear flow rates are utilized.

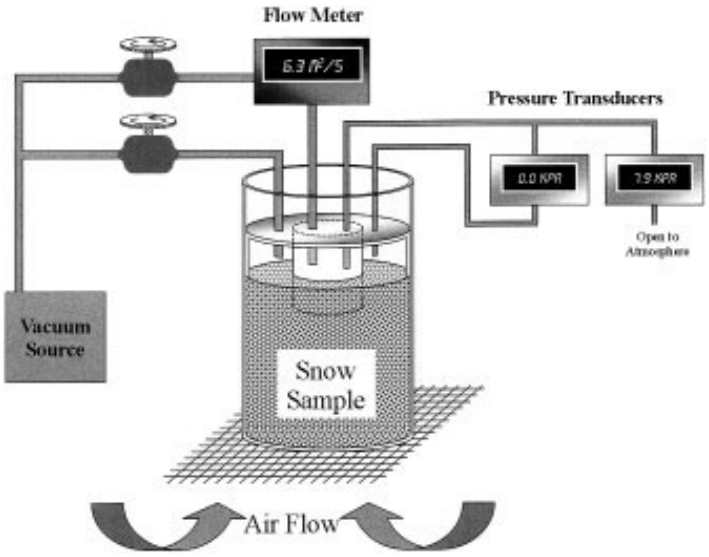

Figure 1.16: Schematics of snow air permeameter [2].

Fortin et al. [23] devised a method for concurrently determining the air permeability and gas diffusion through natural ice layers.. The air permeability obtained ranged from 0.5×10^{-10} to 12.9×10^{-10} m^2 which coincides with the values measured by Albert and Perron [2], 0.5×10^{-10} to 19×10^{-10} m^2. Hemmingsten [33] measured the permeability of artificial ice layers and obtained the values of 0.03 to 1.14×10^{-10} m^2. Figure 1.17 shows the permeability against ice thickness for the experiments mentioned above. No clear indication was found between ice thickness and permeability.

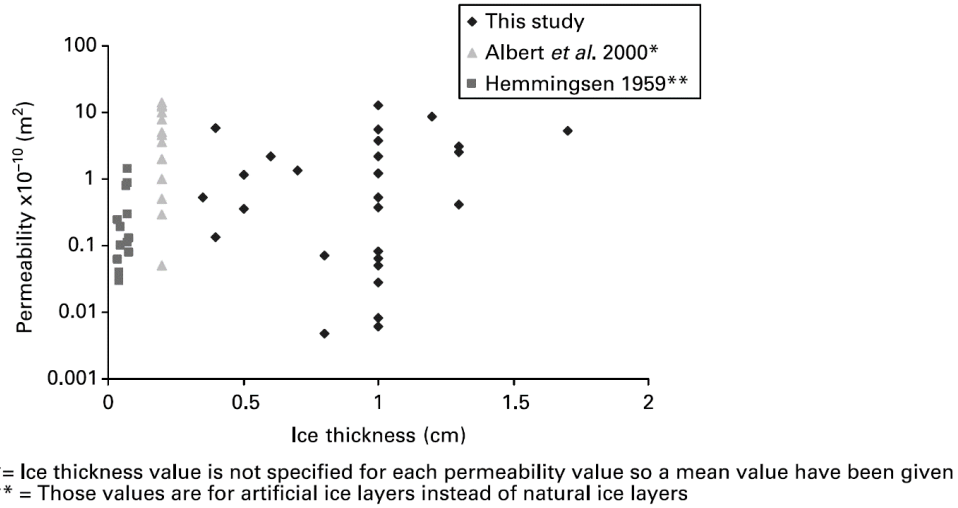

Figure 1.17: Comparison of ice layers permeability from various sources including those collected with the apparatus [23].

In the validation process of air permeameter designed by Fortin et al. [23], spherical glass beads of known diameters were used to simulate the theoretical permeability of natural ice layers. The diameter of the glass beads range between 0.25 - 0.177; 0.15 - 0.105; 0.09 – 0.063mm, which are similar to natural crystals. By simply reorganising the same beads resulted in a 200% variation in permeability values. Natural ice layers have a far more complicated structure than spherical glass beads. Thus, it demonstrates the critical role of structural features of ice layers on permeability, such as porosity, tortuosity, and void distribution. However, the author did not further investigate the effect of structural parameters quantitatively.

1.7.3 Gas and liquid permeability correlation

In an ideal scenario, a solid's permeability should be independent of the kind of fluid employed. This implies that gases and liquids should have the same permeability value. So far, no literature has investigated the variations between gas permeability and liquid permeability on sea ice. However, several experiments on rocks [87, 57, 86] have shown the inconsistency between gas and liquid permeability. Gas permeability is many orders of magnitude to one degree more than water permeability. This phenomena may be connected to the fact that gas permeability is pressure-dependent, commonly known as the Klinkenberg effect [43]. The flow in porous media is often considered a laminar flow described by Darcy's law. The maximum fluid flow velocity occurs at the centre of the pores and decreases linearly towards the pore wall. The velocity at the pore wall is considered to be zero. Klinkenberg [43] observed that gas permeability is greater than liquid permeability, which he attributes to "slip flow" between gas molecules passing through pore walls. That means, the velocity at the pore walls is not zero. Collisions between gas molecules and pore walls grow when the pore radius approaches the mean free path of gas molecules. As a result, extra flux is created at solid pore walls, a phenomenon known as "slip flow." This effect increases both the flow rate and the permeability of the gas [74].
Klinkenberg effect can be expressed as follows:

$$k_g = K_l(1 + \frac{4cl}{r}) = K_l(1 + \frac{c\kappa T}{\pi\sqrt{2}r^3 P}) = k_l(1 + \frac{b}{P}) \tag{1.21}$$

$$b = \frac{c\kappa T}{\sqrt{2}r^3} \tag{1.22}$$

Where k_g is the gas permeability (m^2); K_l is the permeability of the medium to liquid (m^2); l is the mean free path of the gas molecules (m); r is the pore radius (m); κ is Boltzmann's constant (J/K); T is the temperature (K); c is a dimensionless constant; P is the pore pressure (Pa) and b is the Klinkenberg slip factor(Pa).

The value of the parameter l is given by:

$$l = \frac{\kappa T}{4\sqrt{2}\pi r^2 P}$$

The mean free path of the gas molecules is directly correlated to pore radius, temperature and pressure. As pore radius and pressure get larger and the temperature lowers, k_g gets closer to k_l. Therefore, Brace, Walsh and Frangos [6], Zoback and Byerlee [74] performed the gas permeability experiment using high pressure, between 5 to 15 MPa on granite to minimise the Klinkenberg effect.

1.8 Ice thickness

1.8.1 First-year ice

The thickness of ice is a important engineering feature. The thickness of the ice has a direct impact on the loading capacity and the speed with which ice breakers can penetrate ice coverings. The thickness of first-year ice is dependent on the ambient air temperature, the freezing point of the water, the kind of snow, the wind speed, the ocean heat flux, and the balance of surface radiation [76]. A common way to determine the thickness of first-year ice is through the freezing degree method [4]. A few assumptions are made in this method. The assumption is that the system is in a steady state, and that heat transfer between water and ice is low. Wind speed is disregarded, and the temperature at the ice's surface is considered to be equal to the ambient air temperature. The impact of snow cover and ocean heat flow are not taken into account.

Based on the foregoing assumptions, the growth rate of the ice-water interface may be estimated using the energy balance.

$$h = \sqrt{\frac{2k_i}{p_i L}}\sqrt{(T_a - T_b)t} \tag{1.23}$$

Where h is the expected ice thickness (m); k_i is the thermal conductivity of ice (W/mK); p_i is the ice density (kg/m^3); L is the latent heat of fusion of ice (J/kg); T_a is the temperature at top of ice, assumed to be ambient air temperature (°C); T_b is the temperature at bottom of the ice (°C) and t is the freezing time (day).

This equation is commonly quoted as the Stefan equation. Due to the aforementioned assumptions, direct application of this equation will always result in an overestimation of ice thickness. For instance, snow cover insulates the top of the ice, keeping it warmer than the surrounding air temperature. The wind speed may have an effect on the rate of heat transfer at the ice's surface. The ocean heat flux is not taken into account, which has an effect on

heat transfer at the growth surface. Thus, an empirical factor α is introduced to account for these effects. By substituting appropriate parameters into the Stefan equation, the equation can then be simplified.

$$h = 0.035\alpha \left[\sum (T_b - T_a)\right]^{\frac{1}{2}} \tag{1.24}$$

Since the temperature varies with time, the sum of the number of freezing days is used for ice thickness calculation. Please note that α must be less than 1, and the value of α is determined by comparing the actual thickness of ice in that region. This equation takes the thermodynamics of ice growth into account, but not the thickening caused by mechanical deformation. The upper limit of thermodynamic growth's applicability to ice is around 2 m.

1.8.2 Old ice

The term "old ice" refers to ice that has lasted more than one summer melt season. Old ice can be further characterised as second-year ice and multi-year ice. The typical thickness of second-year ice does not exceed 2.5m and is in a layered form in which new ice is underneath old ice from last year. When it comes to measuring the physical qualities of second-year ice and multi-year ice, there is no obvious differentiation between the two [40]. Second-year ice is commonly mistaken for multi-year ice because of this problem. Old ice has a lower salinity than first-year ice, by a large margin. Old ice is also stronger than first-year ice with little porosity. The old ice is closer to freshwater ice than to first-year with the inclusion of minimal salts.

The growth and thickness of old ice are highly correlated to meteorological and mechanical conditions, which are reflected by the microstructure of the ice. Cox et al. [12] and Richter Menge and Cox [68] made thin sections on old ice samples. The sections reveal high variations in grain structures that consisted of granular ice, mixed granular and columnar ice, and pulverised brecciated ice. The disordered granular structure results from mechanical deformation such as ice ridging and rubbing and thermal growth. The columnar ice is inclined within the ice sample, which is one of the signs of deformation. Furthermore, the chaotic nature of the grain structures often results in the old ice being isotropic, unlike anisotropic properties of first-year ice.

1.9 Melt pond formation

Melting of sea ice surface typically starts in late spring in the Arctic region, producing meltwater overlying sea ice, often referred to as melt pond. Melt pond drastically decreases the albedo by reducing the backscattering of sunlight from sea ice [61, 66]. The inflow and outflow of meltwater primarily control the evolution of melt pond coverage. The constrained

discharge of meltwater results in a melt pond above sea level before drainage holes forms from constant warming of sea ice [66].

First-year sea ice melt ponds may seem paradoxical since they are very porous near to their melting temperature [82]. The water level of the melt pond can be determined using Equation 1.19 following Darcy's law. For example, the viscosity of the meltwater is taken as $\mu = 1.79 \times 10^{-3}$ kgm^{-1}s^{-1}, it will give an e-folding time of 3 minutes to 300 minutes for sea ice with 1m thickness with permeability ranging between 1×10^{-9} m^2 to 1×10^{-11} m^2. For context, Eicken et al. [18] conducted in situ permeability testing on summer Arctic sea ice in the northern Chukchi Sea during the early ponding period. The permeability values ranged between 8×10^{-11} m^2 and 3×10^{-10} m^2 with an overall geometric mean of 2×10^{-11} m^2. Such permeability values are slightly lower than all-summer geometric means of 8×10^{-10} m^2 in 1995 and 4×10^{-10} m^2 in 1996 for Arctic sea ice by Freitag and Eicken [26]. Therefore, first-year ice is unlikely to retain melt ponds above sea level during the melting season for an extensive period.

Several explanations have been put forward to explain such a phenomenon. Firstly, different ice structures have distinctive critical porosity thresholds; below such threshold, the ice is considered impermeable. It is around 5 % for columnar ice [27] and 10 % for granular ice [29]. The upper portion of sea ice is typically granular, hence, reduced pore connectivity and lowered permeability. Secondly, forming a layer of impermeable ice as meltwater freezes overlays the existing sea ice surface. Thirdly, meltwater predominately comes from snowmelt which has low salinity, hence higher freezing point (i.e., Equation 1.1) than underlying sea ice. When the meltwater percolates into the pore structure of sea ice, the meltwater freezes and forms water plugs, blocking pathways in ice from further percolation of meltwater, reducing its permeability [28, 17, 26, 66]. Each of the aforementioned mechanisms impacts the permeability of sea ice. Still, at least the first two mechanisms cannot fully explain the evolution of melt ponds above sea level during the melt season. It has been observed that porosity exceeding the critical threshold of 10 % [29] for granular ice prior onset ponding as well as partial removal of superimposed ice layer before pond drainage [66, 47].

Polashenski et al. [65] conducted an in-depth investigation in the southern Chukchi Sea and concluded that percolation blockage of pathways in ice during melt season is the primary factor contributing to the formation of melt ponds above sea level. Polashenski et al. [65] measured the permeability of ice by slug test, which is analogous to bail test as discussed in Chapter 1.7.1. Instead of measuring the inflow rate of water into the borehole for the bail test, the slug test adds additional water to the borehole. It records the water drainage rate until the water level reaches sea level. In doing that, colouring can be added to trace the water penetration in ice. A displacement tube is employed to reduce the volume of water needed and improve the sensitivity of the permeability measurements, as shown in Figure 1.18. The site averages permeability values increase from 5×10^{-12} m^2 to 9×10^{-12} m^2 for ice colder than -2°C, to 2×10^{-11} m^2 to 1×10^{-10} m^2 for ice warmer than -2°C [65].

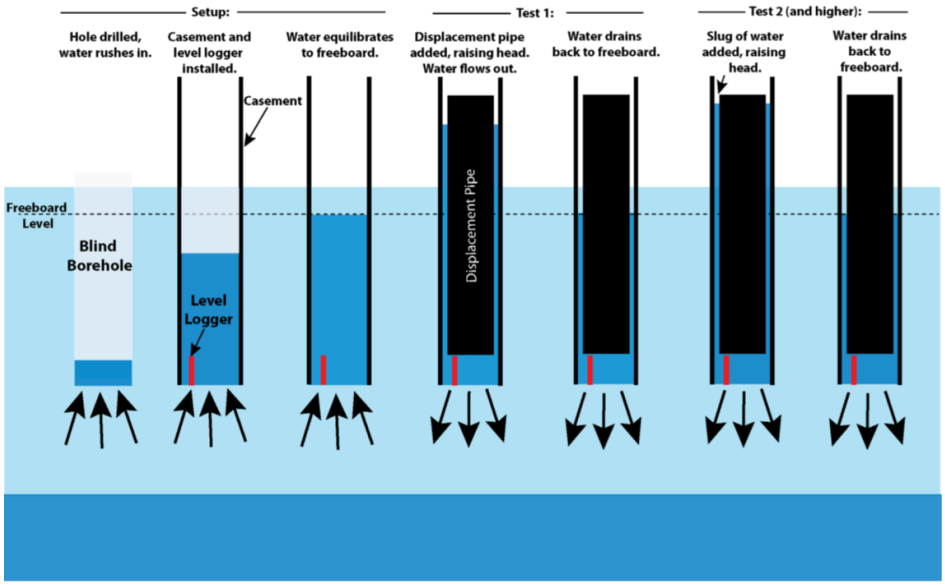

Figure 1.18: A schematic of the experimental apparatus used to test permeability of the sea ice. Light blue indicates sea ice, dark blue indicates ocean and water standing in the boreholes. (left) Borehole flooding during setup stages occurred quickly (<1 min). (middle) The addition of a displacement pipe raised the head and drove the same water that flowed during setup back out (Test 1) as a test of existing permeability. (right) Subsequent tests involved adding water, whose salinity was varied as an experimental factor [65].

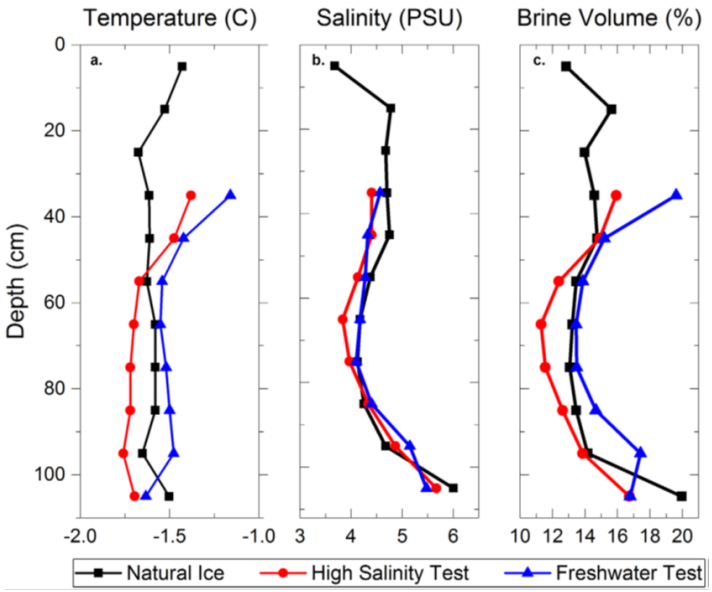

Figure 1.19: Properties of the ice before and after conducting percolation tests. Panes from left to right are (a) temperature, (b) bulk salinity, and (c) derived bulk porosity [24]. Natural ice (black) properties are observed several meters from the test site in the same ice type, to represent a "before" case. High salinity (red) and freshwater test (blue) properties are determined from coring ice beneath the test boreholes after test completion [65].

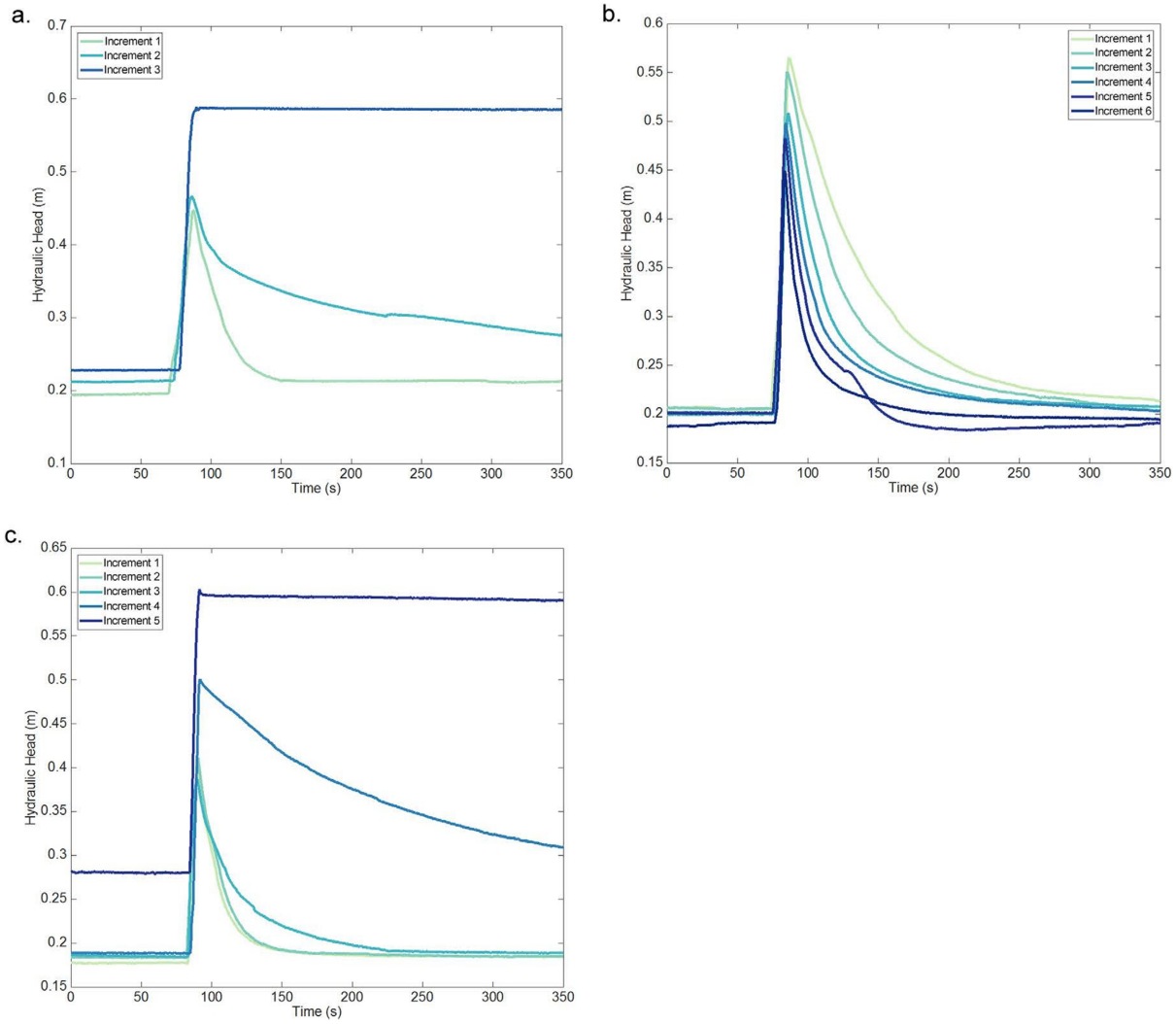

Figure 1.20: (a) Plot of hydraulic head versus time for multiple additions of 750 mL increments of 0.3 PSU water at its freezing point, conducted 26 May 2014. Note that only three increments of water are possible before no more drainage occurs. (b) Plot of hydraulic head versus time for multiple additions of 750 mL increments of 57 PSU water at its freezing point, conducted on 26 May 2014. Note that each subsequent test in the same hole results in an acceleration of drainage. An increase in drainage rate during test 5 may represent the formation or enlargement of a new connective pathway. (c) Plot of hydraulic head versus time, for freshwater added to the borehole used in experiment (b), after the saline water addition tests were complete. Despite the enlargement of the connective drainage pathways, the 3 freshwater still rapidly blocks percolation [65].

A slug test was conducted on 1.19 m thick first-year ice with a pair of boreholes positioned 3.5 m apart to demonstrate whether meltwater can block critical pathways in ice. Water increment with a volume of 750 mL and salinity of 0.3 PSU and 57 PSU were added at their salinity-determined freezing point into each borehole. Figure 1.20a shows the hydraulic head

versus time after adding three increments of water at a salinity of 0.3 PSU. The water level falls exponentially at the first water increment as water percolates through the ice and lowers its hydraulic head to sea level, illustrating highly porous ice just before the ponding period. The subsequent additions of water slows the drainage rate and blocks critical pathways that results in a water level above sea level for an extensive period. In contrast, hydraulic head falls more rapidly as subsequent addition of highly saline water into the borehole as shown in Figure 1.20b, indicating cold, highly saline water can erode and enlarge pathways, making the ice more permeable [65]. Lastly, freshwater was added into the borehole that was previously being conducted using highly saline water. Despite enlarged pathways after the high salinity test, the freshwater could block further percolation, as shown in Figure 1.20c.

Ice temperature and salinity profiles were measured before and after the percolation test using freshwater and high salinity water. The brine volume is determined from Frankenstein and Garner relationship [24] as illustrated in Figure 1.19. It demonstrates little change in ice's bulk properties after the percolation test with brine volume more significant than 10 %, meaning that the ice is sufficiently permeable, and ponding should not occur. The discrepancy between the percolation test and brine volume implies current porosity-permeability relation does not capture the effect of meltwater intrusion. When melting water freezes and becomes insoluble, it stops the vital connecting channels that run deep inside an ice sheet, which is exactly what Polashenski et al. [65] hypothesized was happening. The underlying assumption of random ice pore distribution from which the porosity-permeability relationship is formed is fundamentally altered by the closure of critical connective channels.

Chapter 2

Material and method

2.1 Sample collection

The 2019 SCALE Winter Cruise began on July 18th, 2019 with the departure of the SA Agulhas II from Cape Town. The ship entered the ice around 1 pm on the 26th of July 2019 and departed at 8:30 pm on the 28th. The station layout was intended to address the gradient of sea ice characteristics from the wide ocean to more condensed circumstances. The order of the stations has been altered as a result of flexibility and efficiency considerations. When MIZ1 and MIZ3 were renamed, the naming convention was extended to retain their original geographic distribution [71]. The 2019 SCALE Spring Cruise took place from 11th October 2019 to 18th November 2019 onboard the SA Agulhas II. Consolidated pack ice was cored at stations SMIZ2,3,5,6 and 7 while brash ice was collected at SMIZ 8 and 9. SMIZ 4 was abandoned since the ice was too thin to ensure safe operations. Figure 2.1 and Figure 2.2 illustrate the cruise paths and locations of the MIZ stations for Winter and Spring Cruise, respectively. The naming convention and corresponding coordinates are listed in Table 2.1.

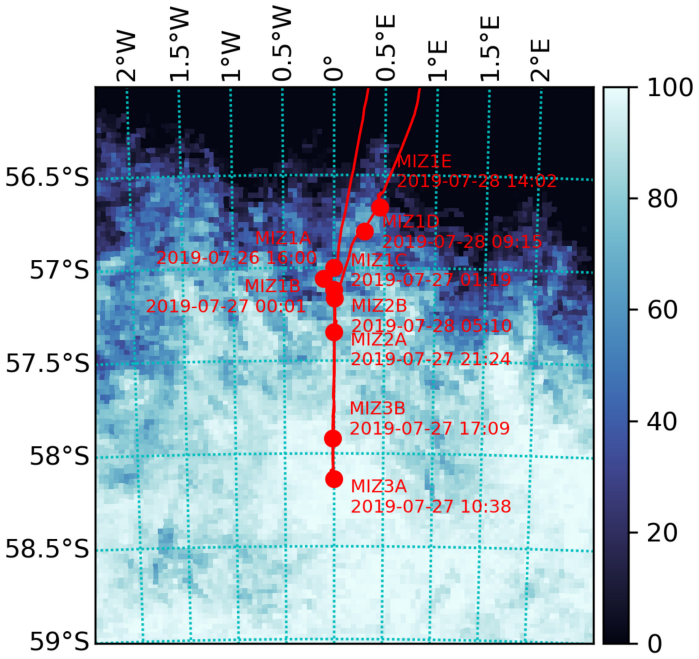

Figure 2.1: Map of the Winter Cruise ice stations with date and hour of the initiation of operations. The ship began its journey from the west and ended it from the east. According to University of Hamburg ASI-AMSR2 processing, the sea ice concentration chart for July 26, 2019, was acquired [71]

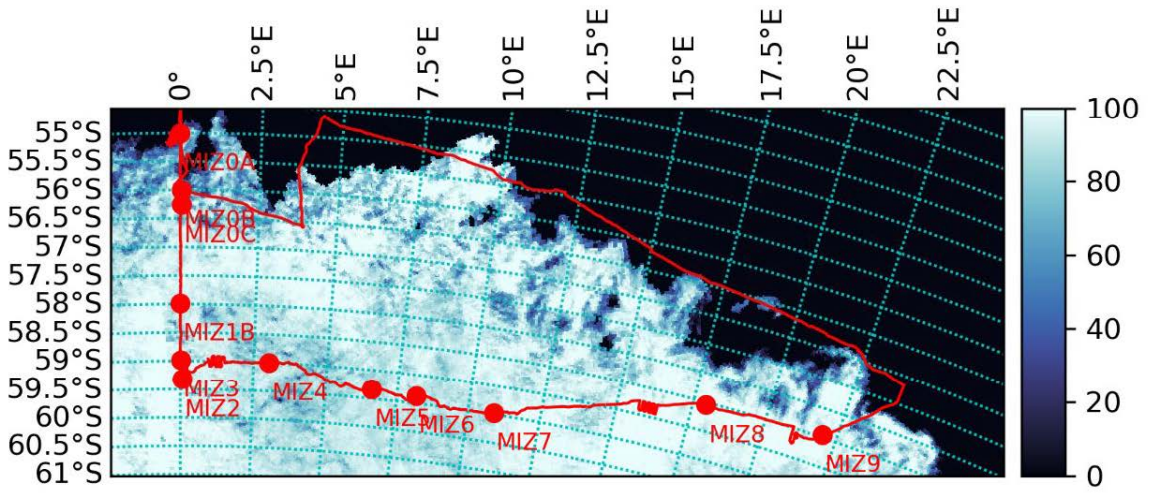

Figure 2.2: Map of the Spring Cruise MIZ stations. Sea ice concentration is from the 28th October 2019.

Table 2.1: List of ice sampling stations [71].

Station	Start Date & Time	Latitude	Longitude
MIZ3A (winter)	27/07/2019 10:38am (UTC)	58.13783 S	0.00442 W
MIZ1D (winter)	28/07/2019 09:15am (UTC)	56.80178 S	0.30262 E
SMIZ 2 (spring)	24/10/2019 13:30pm (UTC)	59.3248 S	0.06662 E
SMIZ 3 (spring)	25/10/2019 11:00am (UTC)	58.98332 S	0.01188 E
SMIZ 6 (spring)	29/10/2019 10:15pm (UTC)	59.3645 S	8.15892 E
SMIZ 7 (spring)	30/10/2019 11:30am (UTC)	59.47255 S	10.88933 E
SMIZ 8 (spring)	1/11/2019 13:16pm (UTC)	58.5488 S	17.93818 E
SMIZ 9 (spring)	3/11/2019 11:33am (UTC)	58.44913 S	21.99735 E

Fieldwork operation for consolidated pack ice during the Winter and Spring Cruise took place on 27 July and 24-30 October 2019 respectively. The coring procedure and core temperature measurement occurred overboard on a block of consolidated pancake ice off the starboard bow as shown in Figure 2.3 and 2.4. Refer Sebastian et al. [71] for detailed sea ice observation and sampling procedures. A total of 26 and 61 consolidated pack ice cores were collected during the Winter Cruise and Spring Cruise, respectively, each for a dedicated type of testing, with the core IDs and corresponding names found in Appendix A1 and B1, respectively.

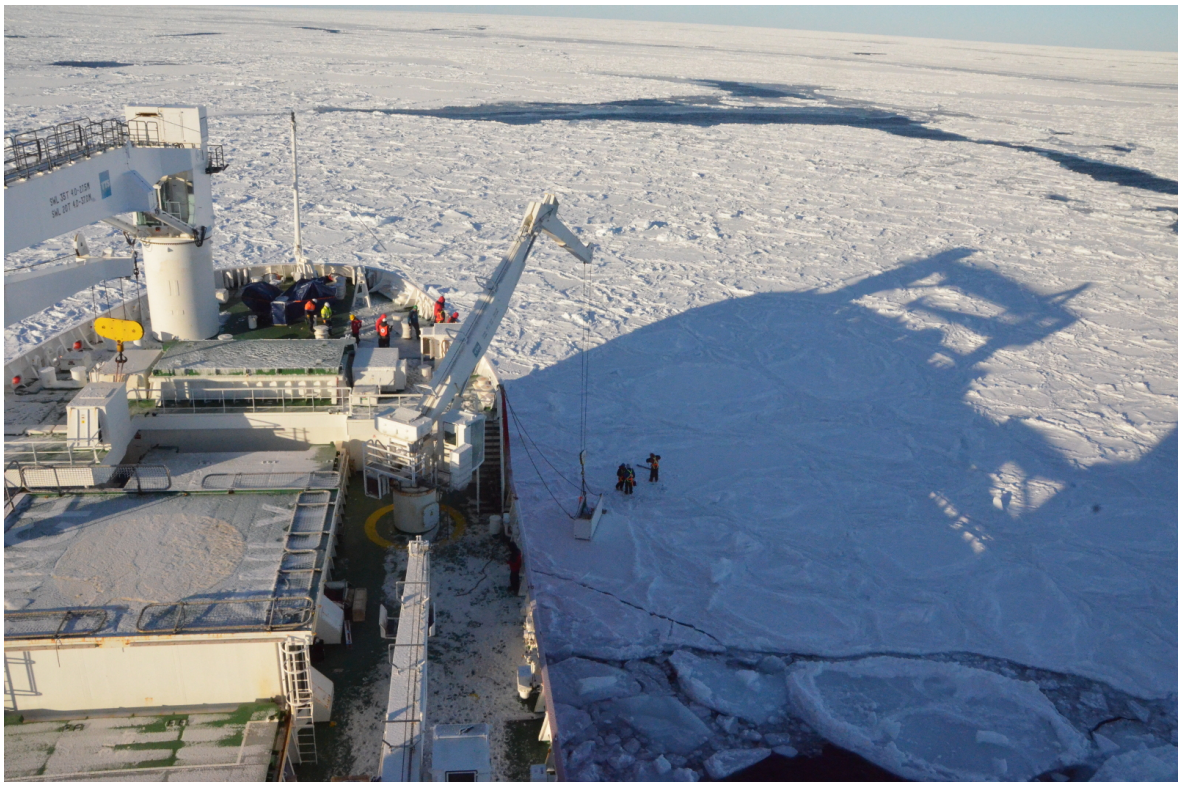

Figure 2.3: Coring field at winter MIZ3A showing the cemented pancakes with sizes varying between 3 and 15 m [71].

Figure 2.4: Coring operations during Spring Cruise at station SMIZ2.

The pancake floes collection during Winter Cruise took place at MIZ1D North ([56,802 - 56,803] °S [0.030 - 0,303]°E) on 28th July 2019 between 10:45 am – 4 pm (UTC). Four pancake ice floes, labeled A through D, were gathered and set on separate wooden grids, as shown in Figure 2.5, to facilitate coring and minimize contamination by the ship deck. Table 2.2 represents information on the various pancake dimensions. All of the pancakes obtained had rafted edges, snow layers, and no obvious biologically active layers. Following that, each pancake ice floe yielded between 17 and 23 cores. Appendix A2 has the corresponding coring layout, complete with core IDs and names.

Figure 2.5: Pancake ice floes on the helideck of the ship: Pancake A (top left), Pancake B (top right), Pancake C (bottom left), and Pancake D (bottom right) fractured into six huge pieces upon removal from the net [71].

Table 2.2: Overview of winter pancake ice floe dimensions [71].

Pancake ice floe		A	B	C	D
Dimensions [m]	Height	0.40	0.37	0.45	0.37
	Length	2.42	2.49	2.40	2.95
	Width	1.83	2.33	2.33	2.51

During the Spring Cruise, two brash ice floes were collected at SMIZ8 and one brash ice floe at SMIZ 9 on 1st and 3rd November 2019 between 11 am – 2 pm (UTC) as shown in

Figure 2.6. The ambient temperature ranged between 1 °C and 3 °C, significantly warmer than the Winter Cruise. The brash ice floes were at the melting stage with the presence of discolouration just below the freeboard, as shown in Figure 2.7. Details on the different brash ice floe dimensions are given in Table 2.3. Between 14 and 24 cores were obtained from each brash ice floe. The corresponding coring layout with core IDs and corresponding names can be found in Appendix B2.

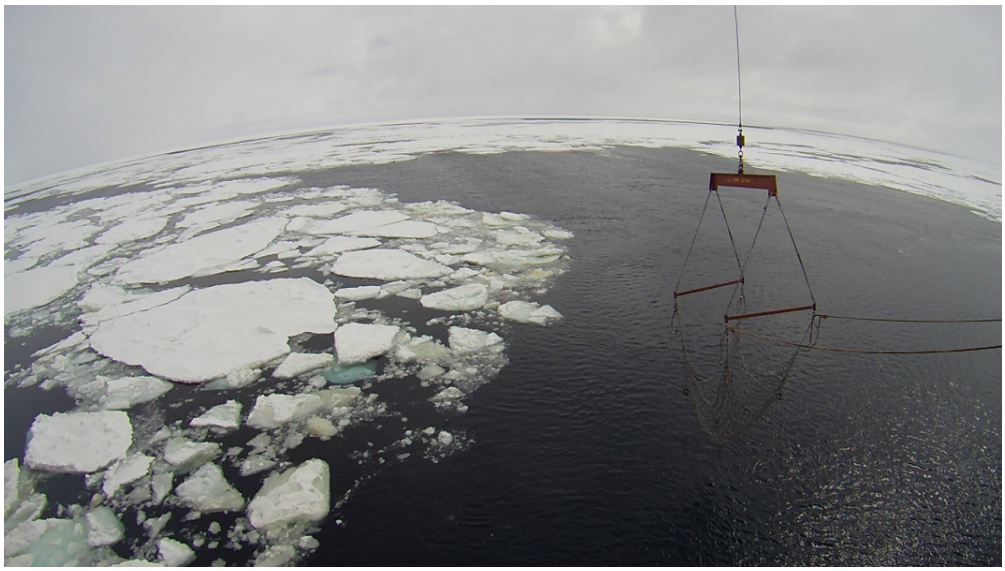

Figure 2.6: Sea ice conditions at SMIZ8 during the floe lifting operations during Spring Cruise.

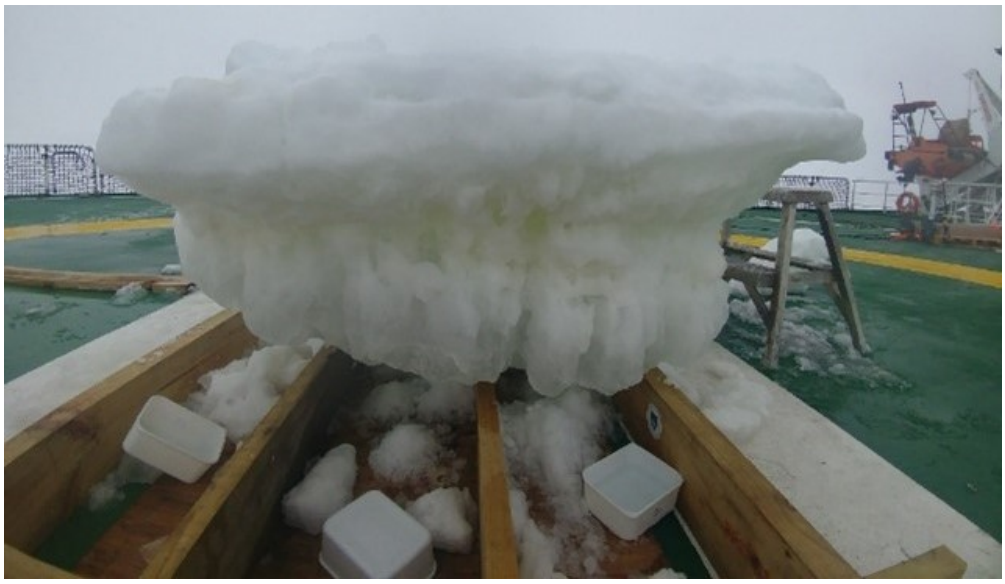

Figure 2.7: Floe B collected at spring SMIZ8.

Table 2.3: Overview of spring brash ice floe dimensions. Floe A and B were extracted from SMIZ8 and floe C was cored from SMIZ 9.

Brash ice floe		A	B	C
Dimensions [m]	Height	0.45	0.81	0.50
	Length	2.40	2.22	3.90
	Width	-	1.70	2.70

2.2 Testing of physical properties

The ice cores from the spring and Winter Cruise were cut into 5 – 10 cm segments with a stainless steel band saw, and subsequently, the vertical temperature profiles were plotted. Segments of ice core were packed inside Ziploc bags and melted in a refrigerator set to 5°C. After melting, the samples' volume was determined using a graduated beaker, and the bulk salinity was determined using a Portasal salinometer [71].

The brine volume is computed using Frankenstein and Garner empirical relations based on the temperature and salinity data collected [24], where V_b denotes brine volume [−], S_i [PSU] the bulk salinity and T [°C] the temperature.

$$V_b = \frac{1}{1000} S_i \left(\frac{52.56}{|T|} - 2.28 \right) for - 0.5°C \geqslant T \geqslant -2.06°C \tag{2.1}$$

$$V_b = \frac{1}{1000} S_i \left(\frac{45.917}{|T|} + 0.930 \right) for - 2.06°C \geqslant T \geqslant -8.2°C \tag{2.2}$$

$$V_b = \frac{1}{1000} S_i \left(\frac{43.795}{|T|} + 1.189 \right) for - 8.2°C \geqslant T \geqslant -22.9°C \tag{2.3}$$

Once the brine volume is obtained, the permeability is computed from porosity-permeability relation by Petrich et al. [62] as shown in Equation 2.4, where Π denotes permeability [m^2], Π_0 [−] the permeability coefficient and V_b [−] the brine volume. The value of Π_0 is in the order of $1 - 3 \times 10^{-8}$ depending on whether to consider unidirectional flow or an isotropic permeability which is often taken of a geometric mean of individual permeability tensor. Π_0 is taken as 1×10^{-8} since it results in a high degree of agreement between experimental results and computational fluid dynamics models [64].

$$\Pi = \Pi_0 \times {V_b}^3 \tag{2.4}$$

A falling head permeability test using kerosene [45] was made in-house by Hasham Taujoo [75] to determine sea ice in situ permeability during Spring Cruise. Kerosene has a freezing point of -40°C with similar kinematic viscosity to the brine, thus, indirectly measuring the brine permeability of the ice. The equipment (Figure 2.8) consists of an 8 mm ID Perspex pipe, 110 mm to 50 mm PVC pipe reducer, adaptor from the Perspex pipe to the 50 mm end of the reducer, custom silicone sleeve (Figure 2.9 for dimensions), band saw, kerosene, retort stand with clamps, stopwatch, marker, bucket, two funnels. The ice core was cut into several samples along the length of the core, with the following dimensions: 4.5 cm x 4.5 cm x 5.5 cm and placed in the silicone sleeve as depicted in Figure 2.10. The following experiment is performed on the ship deck because kerosene is too hazardous to be used inside the Mobile Polar Lab. Each sample is placed in the silicone sleeve. The sleeve is placed in the apparatus, which is subsequently filled with kerosene. The initial and final height of the kerosene in the pipe were logged before and after the 120 s experiment.

Figure 2.8: Experimental setup of falling head test [75].

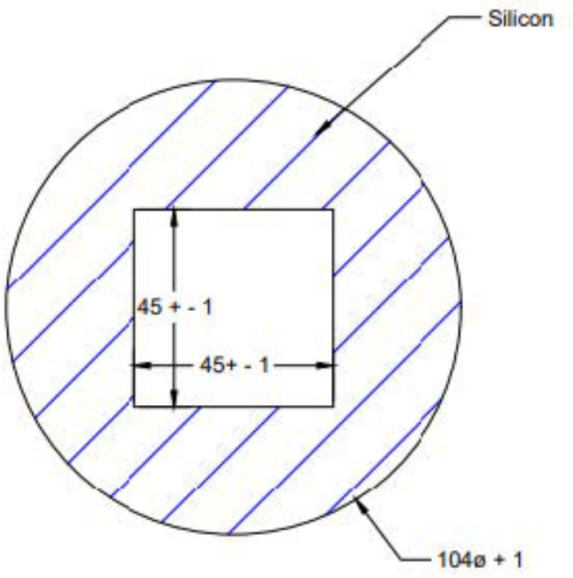

Figure 2.9: Dimensions of custom silicone sleeve (mm) [75].

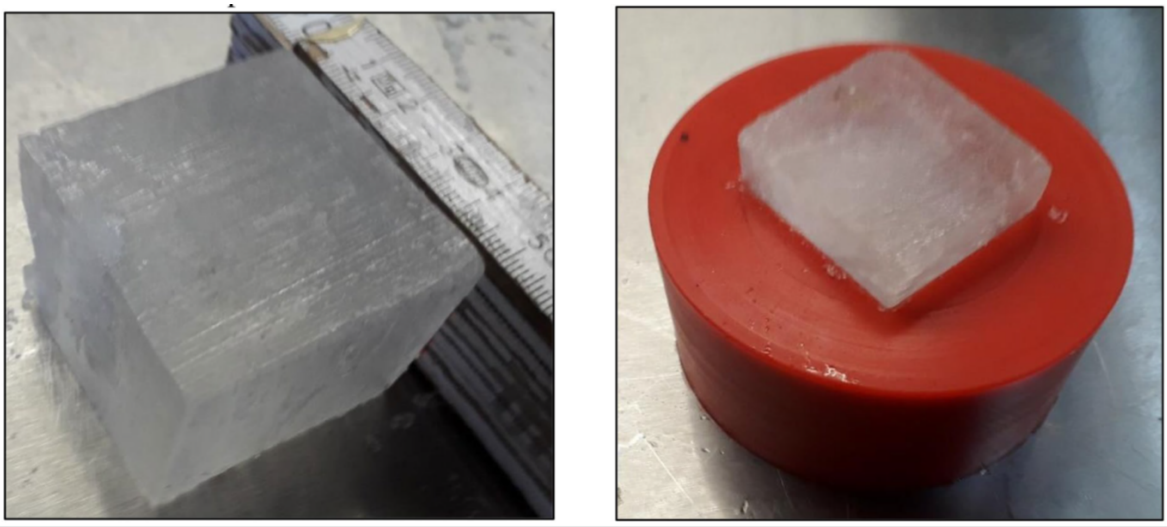

Figure 2.10: Processed ice sample after cutting operations and sample in silicone sleeve [75].

The hydraulic conductivity k of an ice sample is calculated by Equation 2.5 where k denotes hydraulic conductivity [m/s], A' is the internal area of the tube [mm^2], A is the area of the ice core sample [mm^2], H_1 is the initial head [mm], H_2 is the final head [mm], t is the duration of the experiment [s], and d is is the thickness of the ice core sample [m].

$$k = \frac{2.3dA'}{tA} log_{10}\left(\frac{H_1}{H_2}\right) \tag{2.5}$$

The hydraulic conductivity is correlated with the intrinsic permeability by Equation 2.6 where k denotes hydraulic conductivity [m/s], k_i is the intrinsic conductivity [m^2], u is the dynamic viscosity of kerosene [$kgm^{-1}s^{-1}$], and γ is the unit weight of kerosene [$kgm^{-2}s^{-2}$].

$$k = k_i \frac{\gamma}{u} \tag{2.6}$$

During the winter, the temperature at the top of the sea ice is substantially lower than at the bottom. Thus, the brine density is greatest at the ice's surface, resulting in convective overturning of brine in the skeletal layer and brine exchange with the underlying ocean [60]. Wettlaufer et al. [84] suggested Rayleigh number for mushy layer to quantify the intensity of gravity drainage as shown in Equation 2.7.

$$Ra = \frac{gh\Delta\rho\Pi(V_b)}{\mu\kappa} \tag{2.7}$$

In practice, the density difference between brine and sea water $\Delta\rho = \rho_{br} - \rho_{oc}$ is often assumed to be linear in relation to the salinity difference between brine and sea water [79]. Thus, Equation 2.7 can be simplified into

$$Ra = \frac{gh\rho_{oc}\beta(S_{br} - S_{oc})\Pi(V_b)}{\mu\kappa} \tag{2.8}$$

Where h [m] is the thickness of ice, positive upward from ice bottom, g [ms^{-2}] is the acceleration due to gravity, ρ_{oc} is the density of seawater, taken as 1027 kgm^{-3}, β is the haline contraction coefficient, taken as 0.79×10^{-4} kgg^{-1}, S_{br} and S_{oc} [PSU] are the brine and ocean salinity respectively, $\Pi(V_b)$ [m^2] is ice permeability as a function of brine volume and is calculated in accordance with Equation 2.4, κ is thermal diffusivity, taken as 1.2×10^{-7} ms^{-2} and μ is the dynamic viscosity of the liquid, taken as 2.55×10^{-3} $kgms^{-1}$.

The Rayleigh number may be thought of as the ratio of the potential energy $gh\rho_{oc}(S_{br} - S_{oc})$ driving convection to the energy density $\kappa\mu/\Pi(V_b)$ lost during convection due to thermal diffusion and internal friction caused by the brine's viscosity [79]. Therefore, convection can only occur once critical Rayleigh number Ra_c is reached which is around $Ra_c = 10$ [89]. While the brine salinity affects potential energy, the convecting brine's salinity is determined by the thermal field. Brine salinity S_{br} is obtained from the empirical polynomial function (Equation 2.9) using the coefficients from Table 2.4.

$$S_{br} = a_3 + b_3 T + c_3 T^2 + d_3 T^3 \tag{2.9}$$

Table 2.4: Coefficients for functions $F_1(T)$, $F_2(T)$ and $F_3(T)$ for different temperature intervals [14, 15].

T (°C)	a_3	b_3	c_3	d_3
$0 \geq T > -2$	–0.031 6891	–18.3801	0.327 828	0.213 819
$-2 \geq T \geq -22.9$	–3.9921	–22.700	–1.0015	–0.019 956
$-22.9 > T \geq -30$	206.24	–1.8907	–0.060 868	–0.001 0247

The morphology of winter and spring sea ice samples was investigated in terms of crystal structure, stratigraphy, and texture. During the extraction process, the ice cores were visually scrutinized to identify noticeable physical aspects such as the thickness of the snow covering, layers in the texture of the ice, and probable faults such as fractures. The cores were initially cut into 10 cm segments, and longitudinal sections with a thickness of 8 mm were cut from the center of these segments using a stainless steel band saw at −10°C laboratory temperature, as illustrated in Figure 2.11. These 8mm-thick pieces were then sliced using a thermal macrotome to form thin 1mm-thick slices, which were then imaged via cross-polarised sheets. The cross-polarised pictures were then examined for their ice textures and crystal sizes. Stratigraphy diagrams were created using these pictures to allow for simple visual comparison of cores and average crystal sizes [39]. Cross-polarisation was conducted on-board during the Spring Cruise, approximately 12-24 hours after ice extraction. On the other hand, the cores from the Winter Cruise were then carried immediately to the ship's storage facility and analysed at the University of Cape Town six months after being collected and held at −20°C.

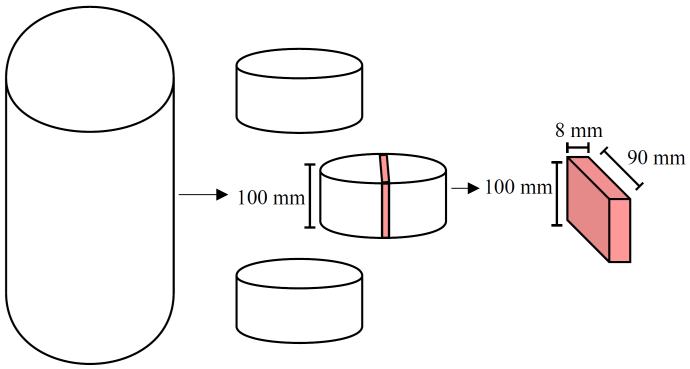

Figure 2.11: Schematic diagram showing how a core sample was cut to produce a thick section [39].

Chapter 3

Results and discussions

3.1 Temperature and salinity

The vertical temperature profiles of winter and spring sea ice exbibit a linear temperature distribution [10, 31] with depth as illustrated in Figure 3.1 and 3.2 [71], substantially larger than winter pack ice floes due to the lower atmospheric temperature, as shown in Table 3.1. Similarly, higher ice temperature is observed in spring sea ice due to elevated temperature during spring. In contrast, pancake C (Winter Cruise) displayed a near-vertical temperature profile and a relatively high temperature on the upper and middle portion of the ice, as shown in Figure 3.1c. One possible explanation is the overwashing and subsequent vertical infiltration of warmer seawater during the collection of pancake C. The snow layer overlaying the pancake ice floes was measured at a temperature of -2.8 ± 0.1°C, reaffirming the possible occurrence of flooding since the ambient temperature was recorded at -11°C. Additionally, ice temperature is associated with the ambient temperature rather than snow temperature except for pancake ice floe C. It has been reported that considerable heat propagation occurred as a result of storm-caused ice floe flooding activities, elevating ice temperature from -8.5°C at the top surface to roughly 3°C at 70 cm deep [67].

Table 3.1: Ambient temperature and wind speed of ice sampling stations for Winter and Spring Cruise.

Station	Date & Time	Temperature (°C)	Wind Speed (m/s)
MIZ3A (winter)	27/07/2019 10:38am (UTC)	-19	15
MIZ1D (winter)	28/07/2019 09:15am (UTC)	-11	10
SMIZ 2 (spring)	24/10/2019 13:30pm (UTC)	-7	9
SMIZ 3 (spring)	25/10/2019 11:00am (UTC)	-5	6
SMIZ 6 (spring)	29/10/2019 10:15pm (UTC)	-9	14
SMIZ 7 (spring)	30/10/2019 11:30am (UTC)	-8	4
SMIZ 8 (spring)	1/11/2019 13:16pm (UTC)	-1	8
SMIZ 9 (spring)	3/11/2019 11:33am (UTC)	-3	15

Data repository for Winter Cruise can be found at https://doi.org/10.25375/uct.14900361 [72]. Data repository for Spring Cruise is not yet publicly available.

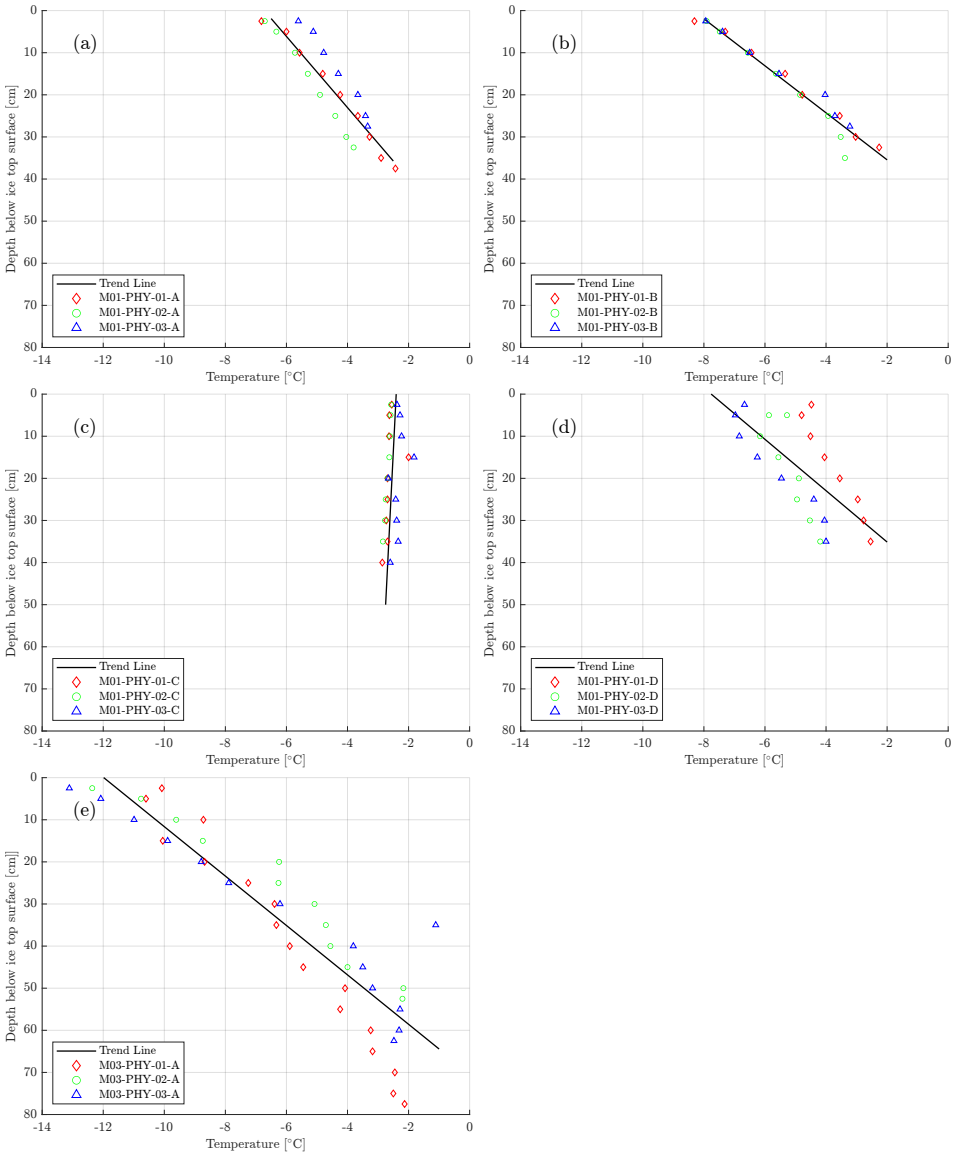

Figure 3.1: Plots of temperature over winter sea ice depth for the four pancake ice floes (cores M01-PHY-01-A/B/C/D, M01-PHY-02-A/B/C/D, M01-PHY-03-A/B/C/D) and for the consolidated pack ice (cores M03-PHY-01-A, M03-PHY-02-A and M03-PHY-03-A), respectively [72].

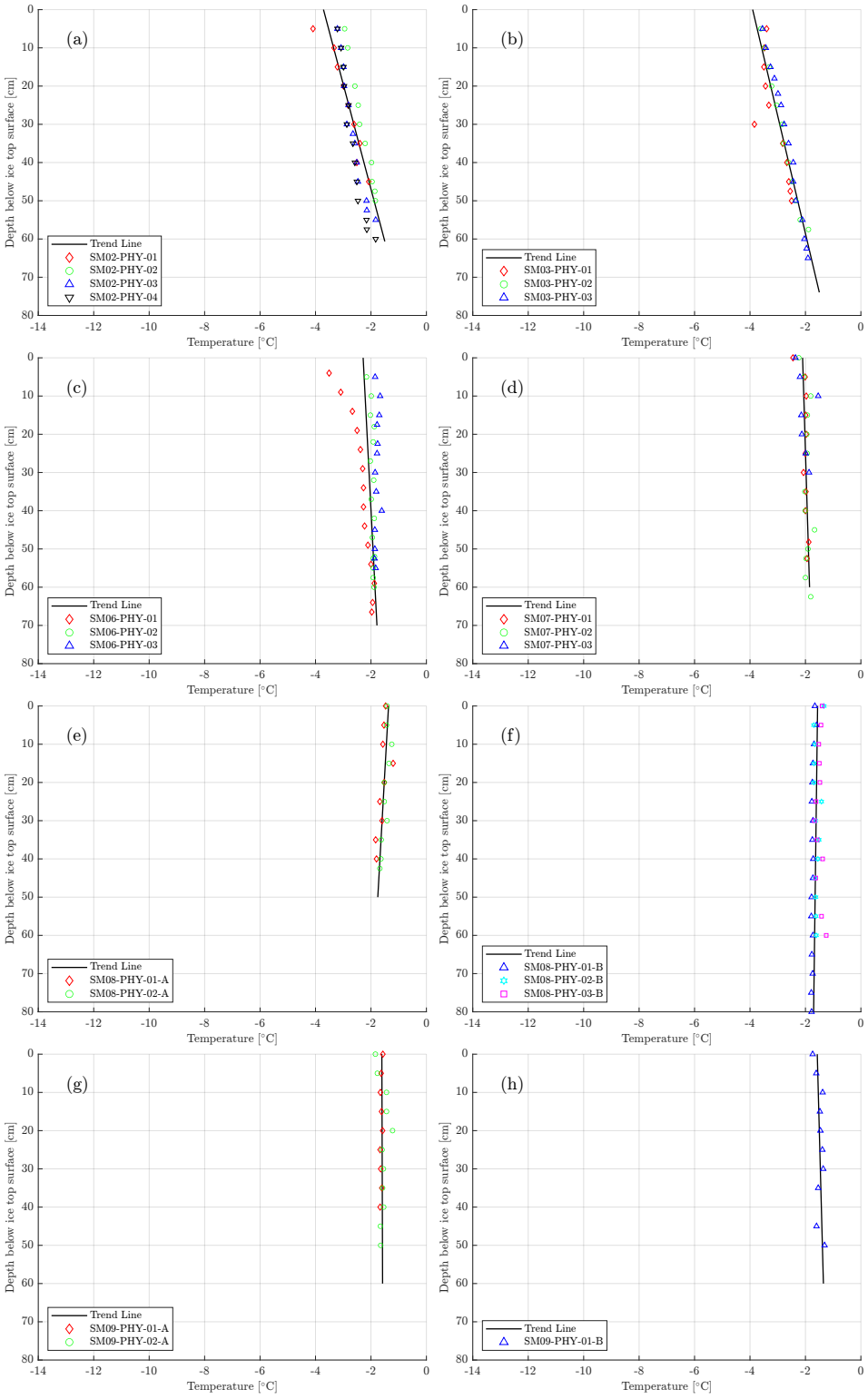

Figure 3.2: Plots of temperature over spring sea ice depth for the four consolidated pack ice floes (cores SM02-PHY-01/02/03, SM03-PHY-01/03, SM06-PHY-01/02/03 and SM07-PHY-01/02/03) and for four pancake ice floes (cores SM08-PHY-01/02-A, SM08-PHY-01/02/03-B, SM09-PHY-01/02-A and SM09-PHY-01-B), respectively.

The shape of the salinity profiles of winter pancake ice floe and spring pack ice exbibit upper half of the characteristic "C-shape" with higher salinity at the top (winter pancake ice: 12.76 ± 5.06 PSU, spring pack ice: 9.66 ± 2.67 PSU) than at the lower depth of ice (winter pancake ice: 5.82 ± 1.05 PSU, spring consolidated pack ice: 5.02 ± 1.69 PSU) [71]. Nakawo & Sinha [53] discovered that the steady-state bulk salinity is inversely dependent on the rate of ice development. A high growth rate at the initial formation of sea ice leads to high salinity towards the uppermost of the ice. Furthermore, Gough et al. [31] conducted a series of salinity measurements on Antarctic winter sea ice and determined that, when growth rate is taken into consideration, granular ice has a somewhat greater salinity than columnar ice. The ice morphology confirms that pancake ice floe A, B, and C are entirely granular ice. Eicken and Hajo [19] analysed the salinity and ^{18}O data together with simulations which demonstrate that upward brine expulsion and flooding play a significant role in rising top salinities, apart from the growth rate and ice temperature. On the other hand, Wettlaufer et al. [84] proposed the Rayleigh number for the mushy layer to estimate the strength of convective overturning of brine and discovered that there is no salt loss from ice owing to gravity drainage until a certain thickness is achieved in their laboratory studies. The delay in salt release prior to gravity drainage could explain relatively high salinity toward the ice surface.

The average salinity of winter consolidated pack ice is 6.18 ± 1.47 PSU, linearly increasing with depth. Notz and Worster [59] conducted in situ measurements in Arctic sea ice and found that high salinity values of thin frazil ice decreased dramatically due to gravity drainage. This might account for the comparatively low salinity at the top of winter-consolidated pack ice where the granular ice is 5 cm and followed by a columnar ice layer. Furthermore, Eicken and Hajo [19] collected salinity data from 128 cores from the Weddell Sea and determined four distinct profile shapes: C-, S-, I-, and?-type profiles. Winter consolidated pack ice has a salinity profile resembling a "?-shape," with the lowest salinity at the top and the highest at the bottom. Low top salinities are thought to be characteristic of ice undergoing retexturing and differential desalination.

The snow depth and salinity measurements of spring pancake ice floes are shown in Table 3.2. The snow salinity of pancake ice floes A, B, and D are much higher than their ice salinity suggesting the presence of surface flooding, which has been found for Weddell Sea [19]. The snow and ice salinity of pancake floe C is similar to the surface flooding and infiltration that may connect during the collection.

Table 3.2: Overview of pancake ice floe snow depth and salinity [72].

Pancake Ice Floe	A	B	C	D
Snow depth (cm)	2.5	3.5	3.6	3.5
Salinity (PSU)	24.74	18.43	9.68	14.26

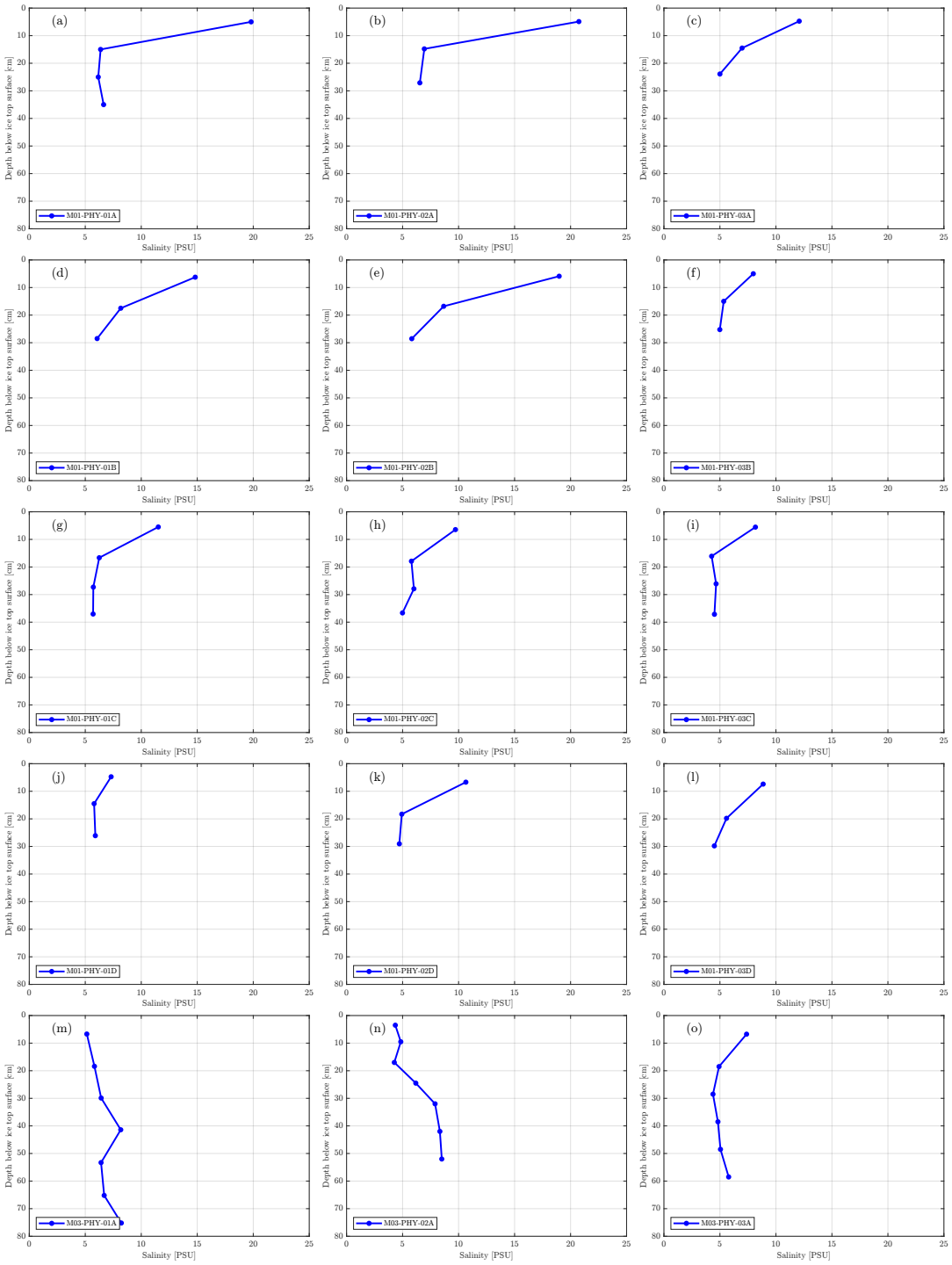

Figure 3.3: Plots of salinity over winter sea ice depth for the four pancake ice floes (cores M01-PHY-01-A/B/C/D, M01-PHY-02-A/B/C/D, M01-PHY-03-A/B/C/D) and for the consolidated pack ice (cores M03-PHY-01-A, M03-PHY-02-A and M03-PHY-03-A), respectively [72].

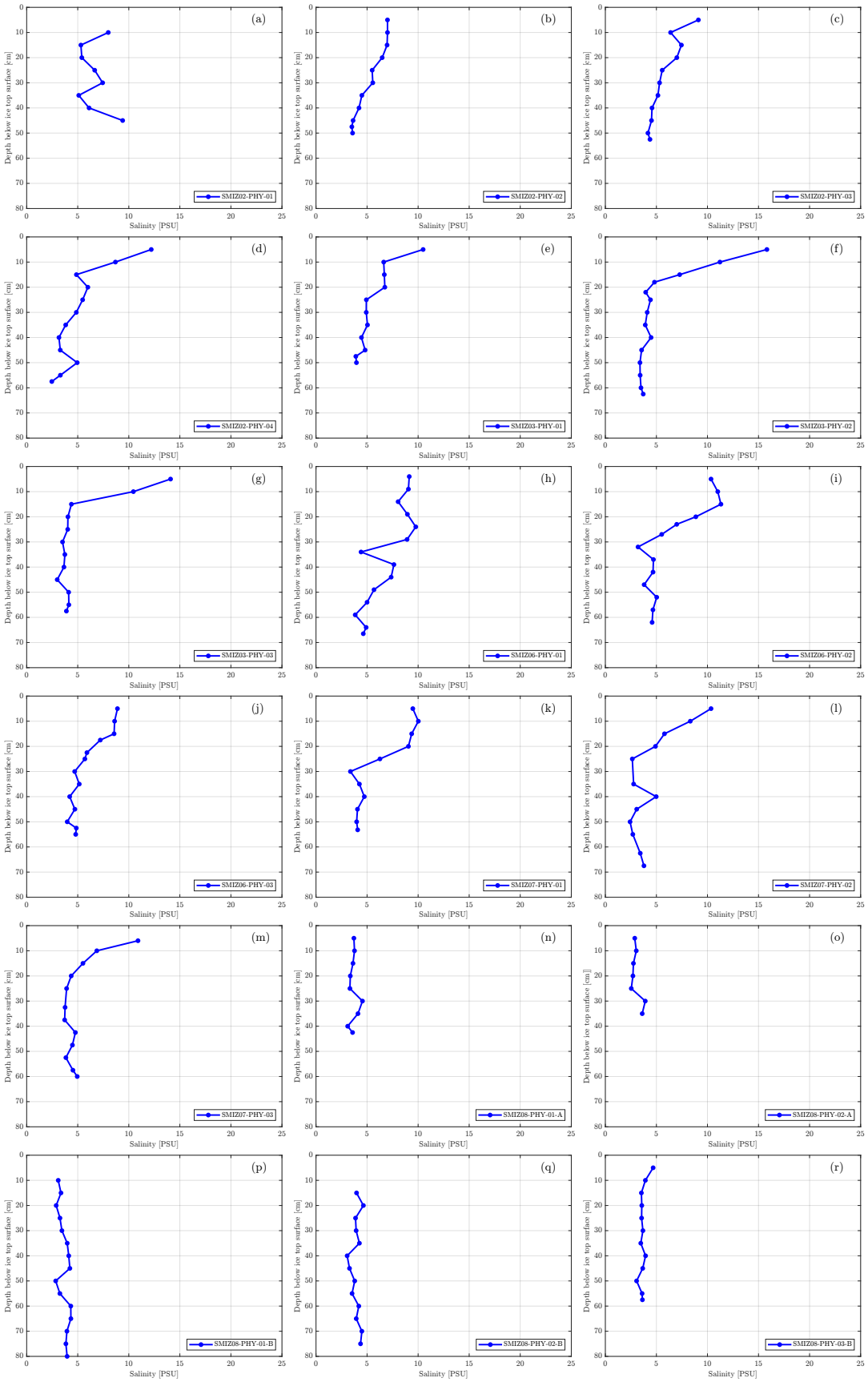
(a)
SMIZ02-PHY-01
(b)
SMIZ02-PHY-02
(c)
SMIZ02-PHY-03
(d)
SMIZ02-PHY-04
(e)
SMIZ03-PHY-01
(f)
SMIZ03-PHY-02
(g)
SMIZ03-PHY-03
(h)
SMIZ06-PHY-01
(i)
SMIZ06-PHY-02
(j)
SMIZ06-PHY-03
(k)
SMIZ07-PHY-01
(l)
SMIZ07-PHY-02
(m)
SMIZ07-PHY-03
(n)
SMIZ08-PHY-01-A
(o)
SMIZ08-PHY-02-A
(p)
SMIZ08-PHY-01-B
(q)
SMIZ08-PHY-02-B
(r)
SMIZ08-PHY-03-B
Depth below ice top surface [cm]
Salinity [PSU]

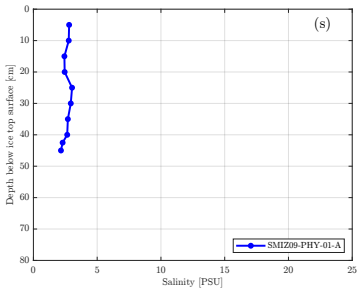

Figure 3.5: Plots of salinity over spring sea ice depth for the four consolidated pack ice floes (cores SM02-PHY-01/02/03/04, SM03-PHY-01/02/03, SM06-PHY-01/02/03 and SM07-PHY-01/02/03) and for three solitary ice floes (cores SM08-PHY-01/02-A, SM08-PHY-01/02/03-B, SM09-PHY-01-A), respectively.

Signs of desalination are evident by comparing salinity profiles of winter pancake ice floes and spring consolidated pack ice. The salinity of the uppermost ice core of spring pancake ice is 9.66±2.67 PSU, lower than winter consolidated pack ice in the same region with 12.76+/-5.06 PSU. The trend continues with lower portion ice with the salinity of 5.02 ± 1.69 PSU and 5.82 ± 1.05 PSU for spring consolidated pack ice and winter pancake ice floes, respectively. Desalination decreases the mean bulk salinity while retaining the characteristic "C-shape," but to a lesser extent [10]. The extreme case of desalination occurred on the spring brash ice floes, which displayed a near-vertical salinity profile with an average salinity of 3.43 ± 0.83 PSU, significantly lower than the salinity of spring consolidated pack ice with an average salinity of 5.02 ± 1.69 PSU. The low salinity values found in spring brash ice floes are likely attributed to the flushing of surface meltwater due to a high ambient temperature ranging between 1°C and 3°C. The brash ice floe was undergoing constant deterioration as indicated by the presence of discolouration just below the freeboard, as shown in Figure 2.7.

Rayleigh number for mushy layer was calculated (Equation 2.8) to estimate the intensity of sea ice gravity drainage. Plots of mushy Rayleigh number versus depth of winter and spring sea ice are shown in Figure 3.6 and 3.7 respectively. Notz and Worster [59] proposes that convection may occur when the Rayleigh number exceeds a threshold amount, generally 10. The value of the Rayleigh number of lower parts of winter and spring sea ice was well below 5, suggesting that minimal convection occurs at the ice-water interface. In comparison, the highest section of winter pancake ice floes and spring consolidated pack ice had a supercritical Rayleigh number. However, the supercritical Rayleigh number at the top of the ice was assumed to be fictitious, since the actively convecting zone appears only in the lowest few centimetres of natural sea ice [59, 7].

Carnat et al. [7] collected Arctic first-year sea ice core samples between November 2007 and June 2008 and found the maximum calculated Rayleigh number was 6.1, well below the critical Rayleigh number of 10. Gough et al. [31] observed similar low bottom-ice Rayleigh numbers (Ra is approximately 2) in field experiments in McMurdo Sound, Antarctica. On the other hand, Notz and Worster [59] measured salinity and temperature evolution of young

sea ice in the Arctic from initial formation to a thickness of around 20 cm during the course of a few days. Gravity drainage occurs in their studies at a critical Rayleigh number of roughly 10, which is consistent with previous empirical and experimental research.

The following hypothesis could explain the difference in Rayleigh numbers. During the first stages of sea ice growth, the sea ice rejects the most of salt into the underlying ocean by convective overturning of saltwater. The rapid ice growth rate leads to intense gravity drainage, characterised by the supercritical Rayleigh number. As the ice becomes thicker, the growth rate reduces, resulting in less intense gravity drainage and significantly reducing the Rayleigh number.

Several other factors may also explain the low bottom-ice Rayleigh number found in winter and spring sea ice. Taking ice core samples only provides a snapshot of sea ice properties, not the complete evolution of sea ice. According to Vancoppenolle et al. [78] one-dimensional sea ice model, vertical convective instabilities may take several weeks to form. By comparison, the crucial Rayleigh number may disappear in as little as two days. Calculating the Rayleigh number from the core samples collected during winter and Spring Cruise can neglect the temporal variation of Rayleigh number. Extracting core samples from the ice sheet and cutting cores into the required dimensions will inevitably introduce brine drainage. Notz et al. [58] reported an underestimating of bottom ice salinity ranging from 1 to 5 PSU by comparing it to other non-destructive measures. Underestimation in bulk salinity leads to reduction of Rayleigh number ranging from 2 to 10. Lastly, some parameters used in Rayleigh number computations are not well constrained (e.g., permeability).

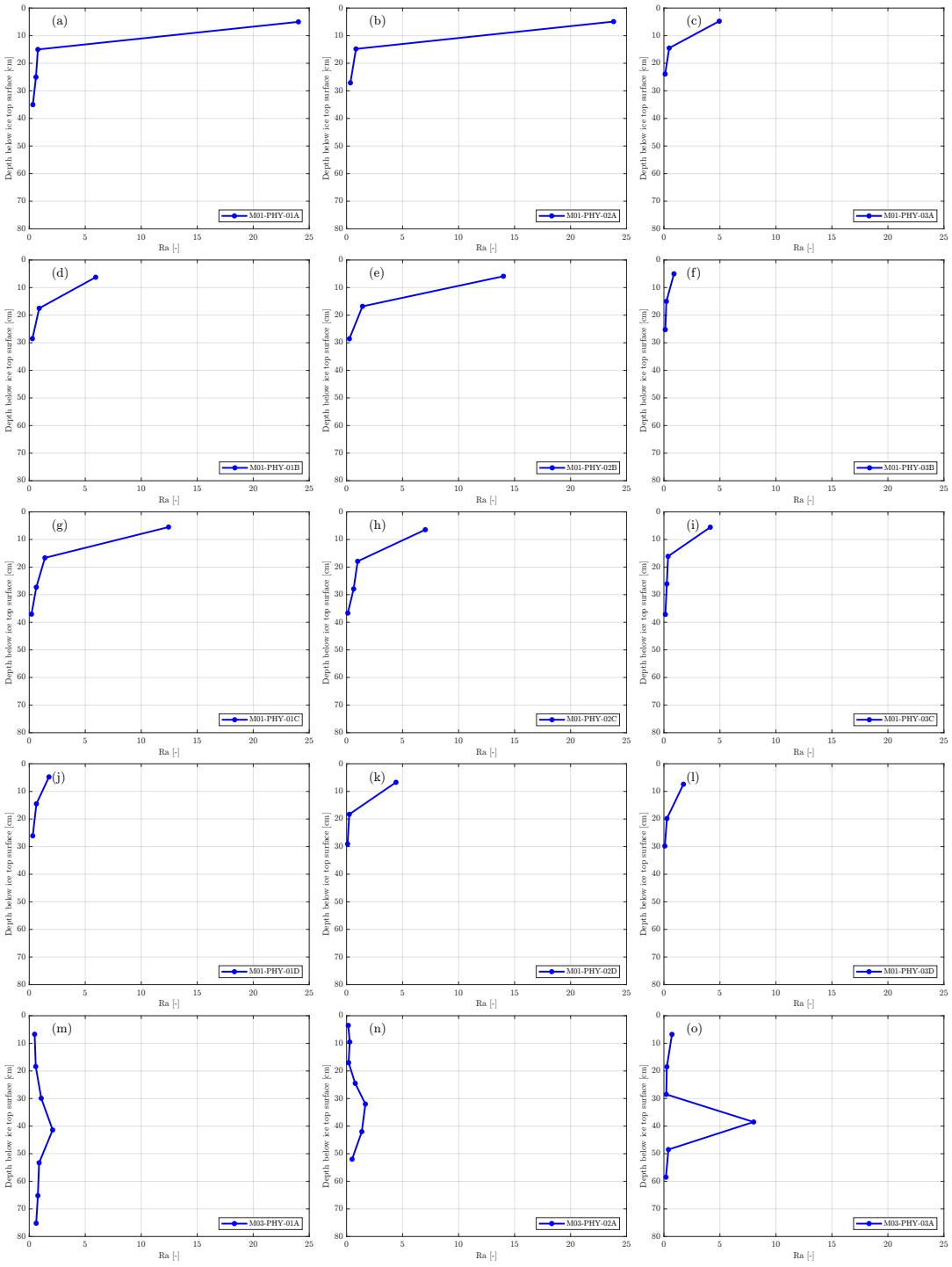

Figure 3.6: Plots of mushy Rayleigh number over winter sea ice depth for the four pancake ice foes (cores M01-PHY-01-A/B/C/D, M01-PHY-02-A/B/C/D, M01-PHY-03-A/B/C/D) and for the consolidated pack ice (cores M03-PHY-01-A, M03-PHY-02-A and M03-PHY-03-A), respectively [72].

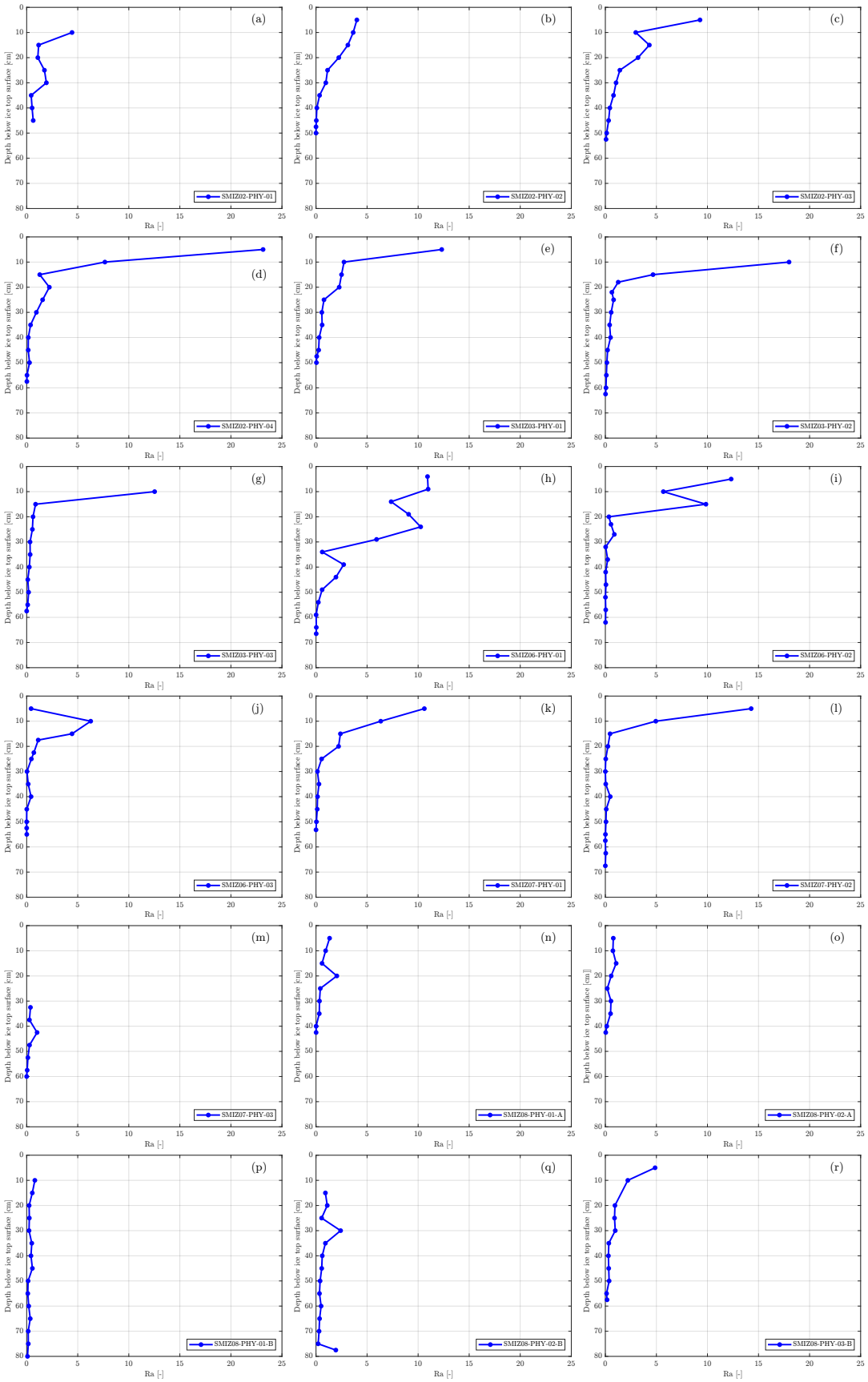
(a)
SMIZ02-PHY-01
(b)
SMIZ02-PHY-02
(c)
SMIZ02-PHY-03
(d)
SMIZ02-PHY-04
(e)
SMIZ03-PHY-01
(f)
SMIZ03-PHY-02
(g)
SMIZ03-PHY-03
(h)
SMIZ06-PHY-01
(i)
SMIZ06-PHY-02
(j)
SMIZ06-PHY-03
(k)
SMIZ07-PHY-01
(l)
SMIZ07-PHY-02
(m)
SMIZ07-PHY-03
(n)
SMIZ08-PHY-01-A
(o)
SMIZ08-PHY-02-A
(p)
SMIZ08-PHY-01-B
(q)
SMIZ08-PHY-02-B
(r)
SMIZ08-PHY-03-B
Depth below ice top surface [cm]
Ra [-]

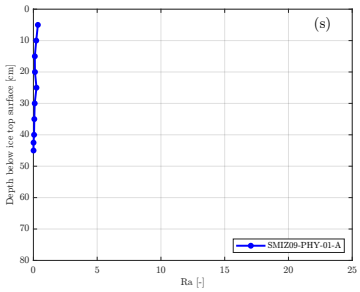

Figure 3.7: Plots of mushy Rayleigh number over spring sea ice depth for the four consolidated pack ice floes (cores SM02-PHY-01/02/03/04, SM03-PHY-01/02/03, SM06-PHY-01/02/03 and SM07-PHY-01/02/03) and for three brash ice floes (cores SM08-PHY-01/02-A, SM08-PHY-01/02/03-B, SM09-PHY-01-A), respectively.

3.2 Texture and fabrics

This section of work is summarised from the Master's thesis by Siobhan Johnson. More in-depth morphological analysis can be found in her work [39]. Granular, columnar and transitional are the three ice textures identified from the core samples collected during the Winter and Spring Cruise. Granular ice is further divided into two sub-categories, namely polygonal granular and orbital granular ice. Polygonal granular ice is formed by incorporating snow and ocean water [21]. Fluctuations in temperature during spring and winter may result in snow melting and percolating through the ice before it refreezes. Frequent flooding on the pancake ice floes is another factor of polygonal granular ice formation, which is often overserved Ross, Amundsen, Bellingshausen, and Weddell seas [37, 20, 73]. Polygonal granular ice is formed under slow freezing condition [37] with an average grain size of 5 mm, slightly larger than orbital granular ice [36]. Orbital granular ice is generated when frazil ice agglomerates and freezes in the presence of a continuous wave and wind activity [21]. It is also formed through the deformational activity of large ice floes, such as rafting and ridging. Columnar ice textures exhibit elongated ice crystals with a horizontal c-axis, and transitional ice displays a mixture of granular and columnar ice. Ice crystals start to elongate into the distinctive columnar ice.

A summary of the fraction of ice textures and their representative crystal sizes are shown in Table 3.3 and 3.4 respectively. The stratigraphy diagrams (Figure 3.8 and 3.9) illustrated the vertical layering of ice textures of sea ice samples. The winter pancake ice floes (WMIZ1 in Figure 3.8) were comprised entirely of orbital granular ice, which is expected for pancake ice floes at the edge of the Antarctic marginal ice zone where the growing environment is hostile, and winter is characterized by tumultuous wave activity [48]. The spring brash ice collected at SMIZ 8 and 9 consists primarily of orbital granular ice but a slightly larger grain size than winter pancake ice floes. The smaller crystal size found in pancake ice floes is attributed to the colder environment and increased growth rate [39].

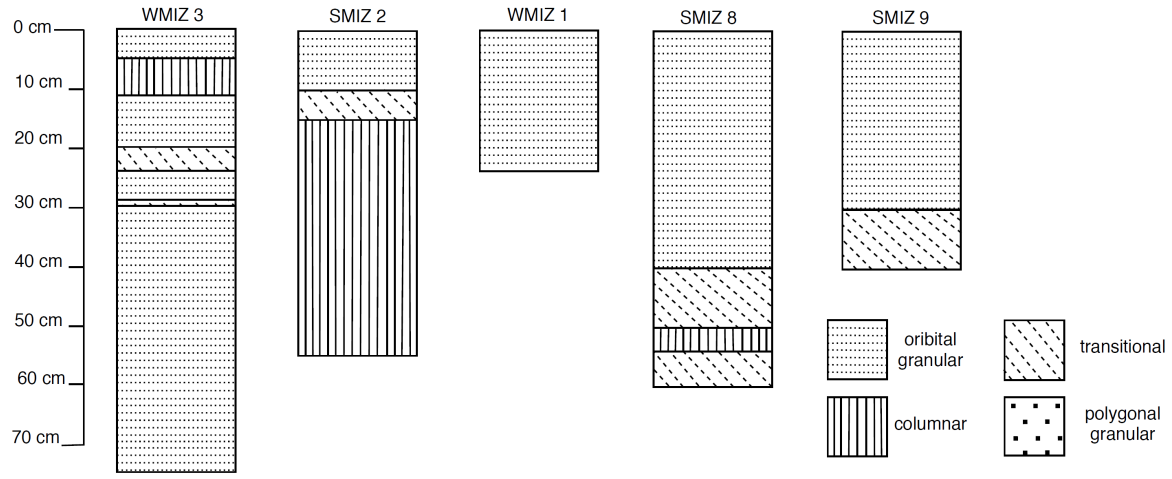

Figure 3.8: Stratigraphy diagrams for winter consolidated pack ice core M03-01A(WMIZ 3), winter pancake ice floes M01-01-A/B/C/D (WMIZ 3), spring consolidated ice cores at SMIZ 2 and spring brash ice cores at SMIZ 8 and 9 respectively [39].

Table 3.3: Summary of the sea ice core textures. u specifies the 95-percentile confidence intervals [39].

Station	Core Length (cm)	Polygonal Granular		Orbital Granular		Transitional		Columnar	
		Fraction (%)	Crystal Size (mm)	Fraction (%)	Crystal Size (mm)	Fraction (%)	Crystal Size (mm)	Fraction (%)	Crystal Size (mm)
SMIZ 3	68,0	-	-	14,7	2,83	14,7	9,37	70,6	18,6
SMIZ 5	70,0	-	-	28,6	2,87	20,0	10,55	51,4	30,1
SMIZ 6	90,0	7,80	4,64	41,1	2,27	15,6	9,35	35,5	23,4
SMIZ 7	80,0	-	-	50,0	2,30	25,0	8.35	25,0	25,6
95 % Confidence Interval				2,30≤μ≤2,80		8,29≤μ≤10,0		20,9≤μ≤25,7	

Table 3.4: Summary of the sea ice core textures. u specifies the 95-percentile confidence intervals [39].

Station Name	Core Length (cm)	Orbital Granular		Transitional		Columnar	
		Fraction (%)	Crystal Size (mm)	Fraction (%)	Crystal Size (mm)	Fraction (%)	Crystal Size (mm)
WMIZ 3	75,0	84,0	2,58	6,70	7,55	9,30	15,6
SMIZ 2	55,0	18,2	2,43	9,10	6,70	72,7	16,1
95 %Confidence Intervals		2,28≤μ≤2,73		6,41≤μ≤7,62		13,9≤μ≤17,8	
WMIZ 1	23,0	100	2,31	-	-	-	-
SMIZ 8	60,0	66,7	2,82	26,7	6,74	6,70	15,5
SMIZ 9	40,0	75,0	2,99	25,0	10,5	-	-
95 %Confidence Intervals		2,53≤μ≤2,89		7,13≤μ≤9,75		-	

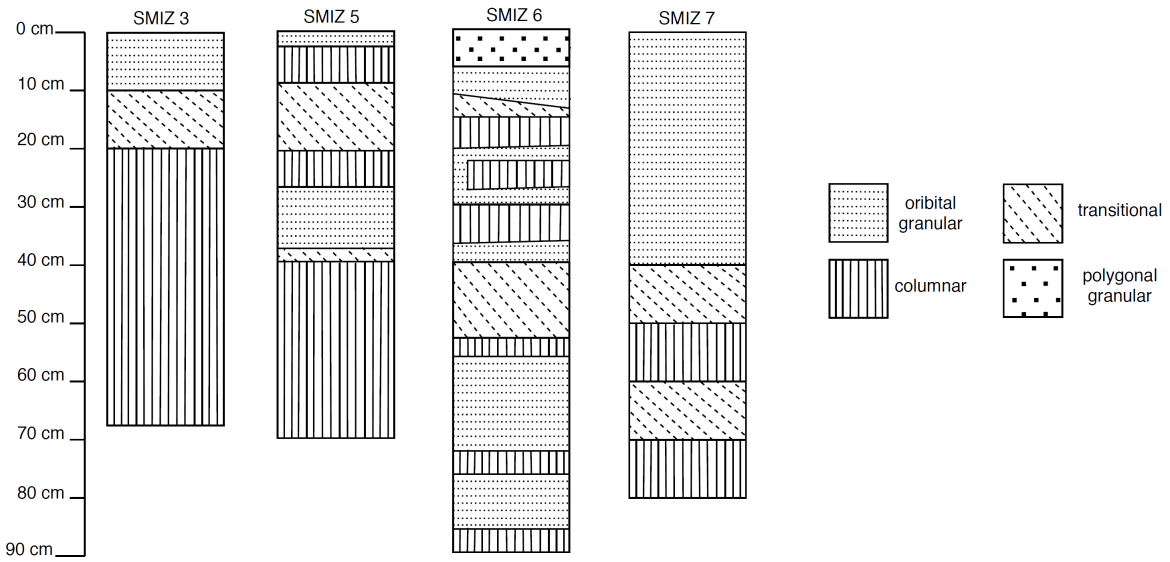

Figure 3.9: Stratigraphy diagrams for spring consolidated ice cores at SMIZ 3, 5, 6 and 7 respectively [39].

It is interesting to compare stratigraphy diagrams of winter (WMIZ3 in Figure 3.8) and spring (SMIZ3 in Figure 3.9) consolidated pack ice since the SMIZ3 has moved about 80 km to the South with respect to the winter location. The winter consolidated pack ice comprised 84 % granular ice with transitional and columnar ice textures sandwiched in between. Highly dynamic ocean environment interrupted the steady ice growth and compelled the ice to regrow from frazil ice accumulation, causing the ice crystals to vary in type, size, and orientation [48, 7]. In contrast, SMIZ 3 illustrated the typical stratigraphy diagram, suggesting no deformation has taken place, and the ocean was relatively clammed to allow continuous growth of columnar ice.

3.3 Brine volume and permeability

Porosity or brine volume for winter and spring sea ice is derived from temperature and salinity by Frankenstein and Garner empirical relations [24] as shown in Figure 3.10 and 3.11. The upper section of winter pack ice ($r = 0.653, n = 20, p = 0.0018$) has lower brine volume than winter pancake ice since pack ice ($r = -4.035, n = 40, p = 0.0098$) has lower ice temperature and lower salinity due to brine drainage. The brine volume of spring pack ice was much higher than the winter pack primarily due to increased ambient temperature.

The permeability is computed from porosity-permeability relation by Petrich, Chris and Eicken, Hajo [62] as shown in Equation 2.4. Large scatter in permeability results is apparent, as illustrated in Figure 3.12 and 3.13 respectively. Similarly, Polashenski et al. [65] observed a one-order-of-magnitude variation in permeability values, with one site report-

ing a three-order-of-magnitude variation in apparently identical thermodynamically grown first-year ice. Such scatter in permeability is believed to be attributed to the considerable heterogeneity in sea ice brine structures [9, 8]. The mean permeability of spring consolidated pack ice ($r = -0.4605, n = 149, p = 0$) is $2.6 \times 10^{-11} \pm 3.67 \times 10^{-11}$ m^2, marginally higher than the winter pack ice ($r = 0.354, n = 20, p = 0.126$) with its mean permeability of $1.1 \times 10^{-11} \pm 2.3 \times 10^{-11}$ m^2. Such permeability is expected since Spring Cruise takes place in the early spring season when the ambient temperature remains relatively low (see Table 3.1).

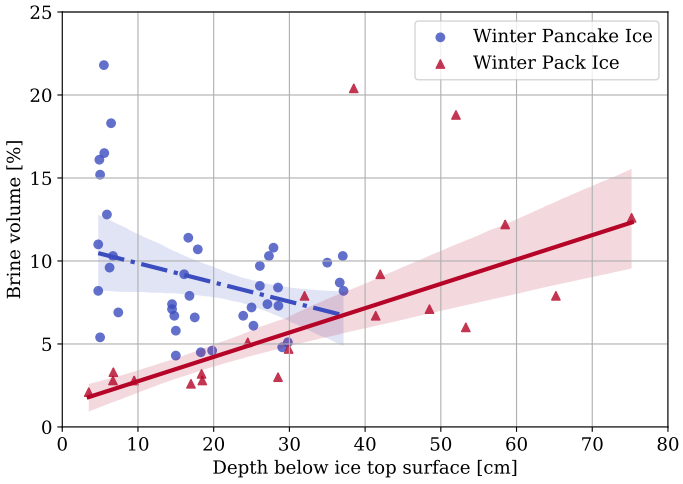

Figure 3.10: Brine volume of winter sea ice as a percentage of the total volume as a function of depth for pancake ice floes and consolidated pack ice at stations, MIZ1D and MIZ3A, respectively.The shading indicates the 90-percentile confidence intervals [72].

In comparison, Eicken et al. [18] conducted in situ permeability testing on early summer Arctic sea ice in the northern Chukchi Sea during the early ponding period. The permeability values range between 8×10^{-11} m^2 to 3×10^{-10} m^2 with an overall geometric mean of 2×10^{-10} m^2. Such permeability values are slightly lower than all-summer geometric means of 8×10^{-10} m^2 to 4×10^{-10} m^2 in 1996 for Arctic sea ice by Freitag and Eicken [26]. Polashenski et al. [65] also investigated in situ permeability of Arctic sea ice in the southern Chukchi Sea during the late spring and early summer period. The site averages permeability values increase from 5×10^{-12} m^2 to 9×10^{-12} m^2 for ice colder than -2°C, to 2×10^{-11} m^2 to 1×10^{-10} m^2 for ice warmer than -2°C. A continuous trend of increase in permeability is apparent with seasonal progressions and a rise in ice temperature. The effect of ice temperature on permeability is also evident by comparing the permeability of winter and spring pack ice, as illustrated in Figure 3.14. The permeability of the upper portion of winter pack ice is significantly lower (up to two orders of magnitude) than the spring pack ice due to extremely low ambient temperature during the winter period (see Table 3.1). The permeability trendlines intersect at the depth just over 50 cm, which corresponds to approximate ice temperatures of -3°C and -2°C for winter pack ice and spring pack ice, respectively, further emphasising the influence

of ice temperature.

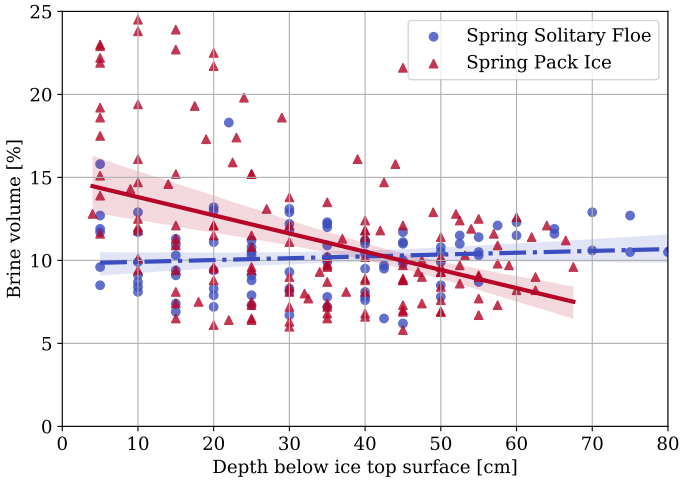

Figure 3.11: Brine volume of spring sea ice as a percentage of the total volume as a function of depth for consolidated pack ice (SMIZ2/3/6/7) and pancake ice floes (SMIZ8/9) respectively. The shading indicates the 90-percentile confidence intervals.

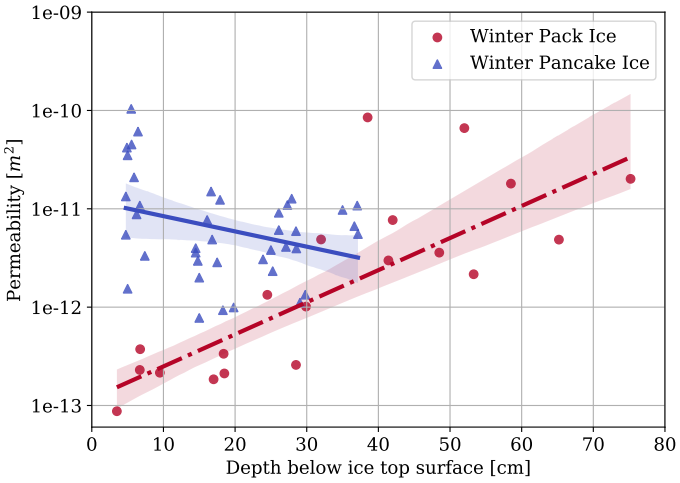

Figure 3.12: Permeability of winter sea ice as a function of depth for pancake ice floes and consolidated pack ice at stations, MIZ1D and MIZ3A, respectively. The shading indicates the 90-percentile confidence intervals [72].

Table 3.5: Empirical permeability and experimental permeability from the falling head test.

	Permeability range (m^2)	Average permeability (m^2)
Winter pack ice (empirical)	2×10^{-13} to 1×10^{-10}	1.1×10^{-11}
Winter pancake ice (empirical)	1×10^{-12} to 1×10^{-10}	1.3×10^{-11}
Spring pack ice (empirical)	2×10^{-12} to 2×10^{-10}	2.6×10^{-11}
Spring pack ice (experimental)	1×10^{-12} to 8×10^{-11}	1.5×10^{-11}
Spring brash ice floe (empirical)	3×10^{-12} to 4×10^{-11}	1.4×10^{-11}
Spring brash ice floe (experimental)	3×10^{-10} to 8×10^{-12}	2.0×10^{-10}

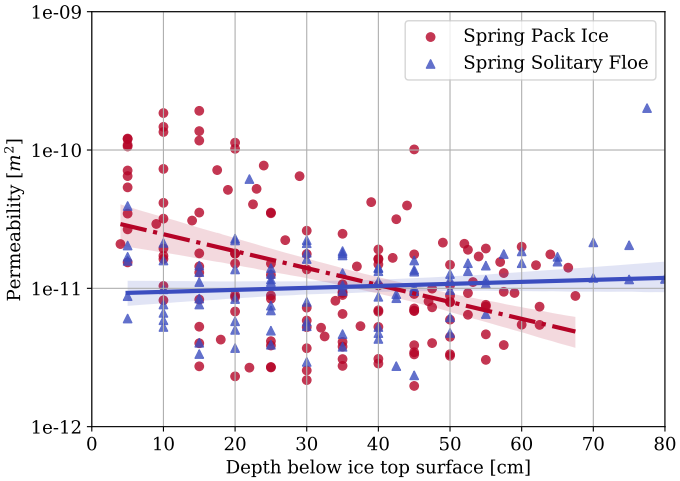

Figure 3.13: Permeability of winter sea ice as a function of depth for consolidated pack ice (SMIZ2/3/6/7) and pancake ice floes (SMIZ8/9) respectively.The shading indicates the 90-percentile confidence intervals.

The comparison between empirical (from porosity-permeability relation) and experimentally determined permeability of spring consolidated pack ice is illustrated in Figure 3.15. The experimentally determined permeability of spring pack ice was reasonably consistent with the empirical permeability exhibiting a decline in permeability with depth. The mean experimentally determined permeability of the spring pack ($r = -0.22, n = 55, p = 0.107$) is 1.5×10^{-11} m^2 $\pm 1.41 \times 10^{-11}$ m^2, slightly lower than the mean empirical permeability of $2.6 \times 10^{-11} \pm 3.67 \times 10^{-11}$ m^2.

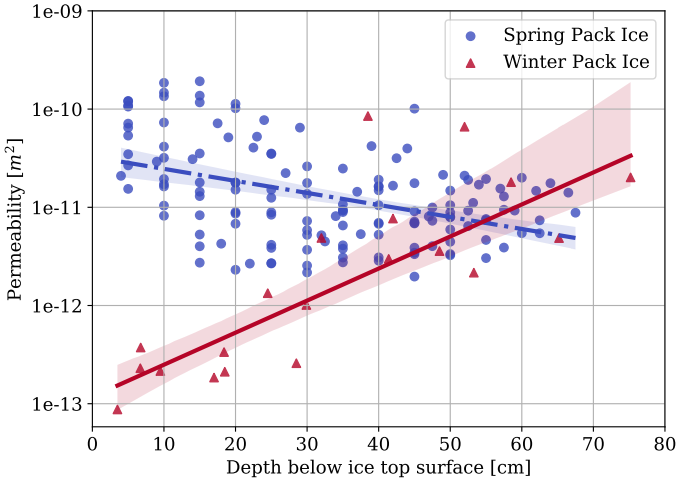

Figure 3.14: Permeability as a function of depth for winter pack ice (MIZ3A) and spring pack ice (SMIZ2/3/6/7) respectively. The shading indicates the 90-percentile confidence intervals [72].

During spring brash ice floes collection, the average ambient temperature was -2°C, and ice was undergoing constant deterioration as indicated by the presence of discolouration just below the freeboard, as shown in Figure 2.7. As tabulated in Table 3.5, the mean empirical permeability of spring brash ice floes is $1.4 \times 10^{-11} \pm 2.1 \times 10^{-11}$ m^2, about one order of magnitude lower than the experimentally determined permeability of $2 \times 10^{-10} \pm 3.4 \times 10^{-10}$ m^2. The majority of the falling head tests conducted on the spring brash ice floes were unsuccessful due to large holes and cracks in the ice samples.

Literature rarely examines the discrepancy between in-situ permeability measurements and permeability obtained from porosity-permeability relation [62], especially in the melting sea ice. Two possible explanations could explain the differences between empirical and experimental permeability of the spring brash ice floes. Firstly, current porosity-permeability relations [25, 28, 62] assume Darcy's law is valid. During the melting season, brine channels in sea ice widen, flow through wide channels may not be fully laminar, when the importance of momentum conservation in draining water becomes evident [66].

Secondly, Polashenski et al. [65] conducted a slug test and found that meltwater intrusion can either block or enlarge the critical drainage pathways in sea ice depending on the meltwater salinity. The critical threshold is brine salinity. Meltwater with salinity higher than brine salinity will enlarge the brine channels to maintain thermodynamic equilibrium, making it more permeable. Likewise, meltwater with salinity lower than brine salinity water will block the pathways. The experiment suggests that the actual permeability of ice can deviate from the empirical permeability determined from brine volume due to meltwater intrusion. Polashenski et al. [65] hypothesised that the closing of the critical connective pathways violates the basic assumption of random pore distribution in ice, which is the basis for the porosity-

permeability relation.

For spring brash ice floes, the average ice temperature was around -1.6℃, corresponding to brine salinity of 29 PSU (Equation 2.9) [62]. The brine salinity of brash ice floes is lower than seawater, suggesting that surface flooding can potentially enlarge the brine channels, creating highly porous ice with little impact on the brine volume and underestimating the actual permeability of ice. It is inconclusive which of the mechanism mentioned above may play a significant role in explaining the deviation of experimentally determined permeability from the permeability derived from brine volume. More research is necessary to validate the applicability of porosity-permeability relation in melting sea ice.

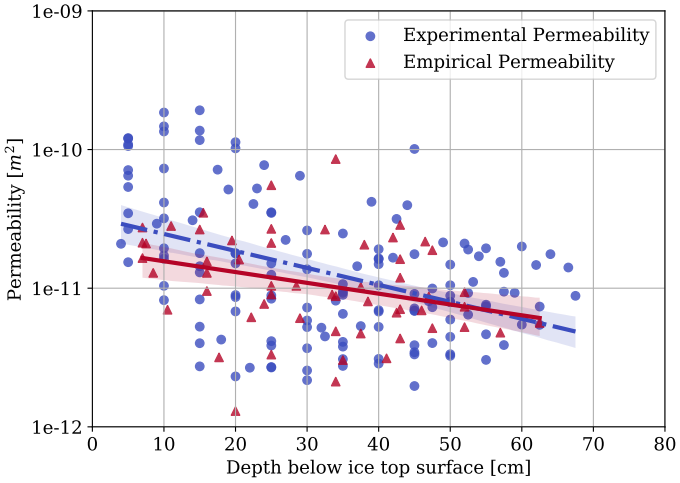

Figure 3.15: Comparison of experimental permeability and empirical permeability as a function of depth for spring consolidated pack ice (SMIZ2/3/6/7). The shading indicates the 90-percentile confidence intervals.

Conclusion

The ice samples collected during winter and Spring Cruise exhibit a linear temperature profile with depth. The slope of the spring temperature profile is steeper than in winter due to the elevated ambient temperature. The only exception is the winter pancake ice floe C with a near-vertical temperature profile, likely due to overwashing and infiltration of flood during collection. The shape of the salinity profiles of winter pancake ice floe and spring pack ice exbibit the upper half of the characteristic "C-shape" with higher salinity at the top than the lower depth of ice. The average salinity of winter consolidated pack ice is 6.18 ± 1.47 PSU, linearly increasing with depth. Low salinity was found in spring solitary brash ice floes, likely due to the flushing of meltwater. Rayleigh number for the mushy layer was calculated to estimate the intensity of sea ice gravity drainage. The results indicate that minimum convective overturning occurs at the ice-ocean interface since the calculated Rayleigh number was close to zero. Even though brine drainage during extraction and frequency of the salinity measurements will affect the accuracy of Rayleigh number, the low ice growth rate is likely to be the major contributor to the minimal convective overturning found at the bottom-ice. Rapid convective overturning takes place at the initial stage of ice formation where ice is relatively thin. As ice thickness increases, the ice growth rate decreases and slows down the overturning. Since the sampled ice cores have a length ranging between 30 cm and 80 cm, a low Rayleigh number at ice-bottom is expected.

The winter consolidated ice and pancake ice floes were comprised almost entirely from orbital granular ice due to harsh and turbulent wave actions is prevalent during winter. In contrast, spring consolidated pack ice illustrated the typical stratigraphy diagram, suggesting no deformation has taken place, and the ocean was relatively calmed to allow continuous growth of columnar ice. The permeability is computed from porosity-permeability relation by Petrich, Chris and Eicken, Hajo [62] with large scatter in the permeability results. Comparing the permeability values of spring and winter consolidated pack ice shows a continuous increase in permeability with seasonal progressions and a rise in ice temperature. The experimentally determined permeability values of spring consolidated pack ice were consistent with the permeability estimated empirically from the porosity-permeability relation. However, the permeability values of spring brash ice floes determined from porosity-permeability relation deviate from field observations due to the presence of large holes and cracks in the ice samples. Currently, the porosity-permeability relations only account for the ice temperature and bulk salinity without considering the effect of different ice textures on sea ice permeability. Previous studies have shown that granular ice has lower permeability than columnar ice since granular ice crystals have a random c-axis compared to the horizontal c-axis found in columnar ice [27, 28]. Incorporating sea ice textures into the porosity-permeability relation may yield better estimations of sea ice permeability.

Future research

Improvement of the falling head test

Due to constrained funding and time, the falling head permeability prototype has the following limitations which can be improved on in future iterations:

- Kerosene has a pungent smell, and it is flammable, which is dangerous for experimental operations. A viable alternative fluid could be water mixing with anti-freeze.
- The silicone sleeve that holds the ice sample is susceptible to getting damaged by the sharp corners of the ice sample. Furthermore, the ice sample is unrestrained at the bottom, which leads to the ice sample slipping out of the silicone sleeve. A possible solution is to divide the silicone sleeve into two halves and support it with metal mesh.
- The falling head equipment should be verified by alternative liquid permeability tests such as bail test with lab-grown NaCl ice before conducting on natural sea ice.

Effect of sea ice microstructure on the permeability

Currently, the brine volume is calculated as a function of the ice temperature and salinity. After that, the permeability is then estimated via the porosity-permeability relation. However, the only input to the porosity-permeability relation is the brine volume, neglecting the potential impact of sea ice microstructure on the permeability. In future research, NaCl ice samples with the same temperature and salinity but varying microstructures are grown in the lab. The permeability of the lab-grown NaCl ice is then measured using the bail or falling head test. The effect of sea ice microstructure on permeability can then be quantified by examining the permeability results from the bail or falling head test.

Appendix A: Pancake and consolidated pack ice core lists for Winter Cruise

A1 Winter consolidated pack ice data

Table A1: Overview of winter pack ice core IDs, corresponding core names, testing designation, and date and time when cored.

Core ID	Core Name	Test Designation	Date Cored	Time Cored
1	M03-TM-01-A	Trace metal	27th July 2019	10am-4pm (UTC)
2	M03-TM-02-A	Trace metal	27th July 2019	10am-4pm (UTC)
3	M03-TM-03-A	Trace metal	27th July 2019	10am-4pm (UTC)
4	M03-TM-04-A	Trace metal	27th July 2019	10am-4pm (UTC)
5	M03-TM-05-A	Trace metal	27th July 2019	10am-4pm (UTC)
6	M03-BGC-01-A	Isotope	27th July 2019	10am-4pm (UTC)
7	M03-BGC-02-A	Isotope	27th July 2019	10am-4pm (UTC)
8	M03-PHY-01-A	Temperature	27th July 2019	10am-4pm (UTC)
9	M03-PHY-02-A	Temperature	27th July 2019	10am-4pm (UTC)
10	M03-PHY-03-A	Temperature	27th July 2019	10am-4pm (UTC)
11	M03-CPUT-01-A	Biology	27th July 2019	10am-4pm (UTC)
12	M03-CPUT-02-A	Biology	27th July 2019	10am-4pm (UTC)
13	M03-BIO-01-A	Bio-cultivation	27th July 2019	10am-4pm (UTC)
14	M03-CT-01-A	MicroCT	27th July 2019	10am-4pm (UTC)
15	M03-CT-02-A	MicroCT	27th July 2019	10am-4pm (UTC)
16	M03-CP-01-A	Morphology	27th July 2019	10am-4pm (UTC)
17	M03-CP-02-A	Morphology	27th July 2019	10am-4pm (UTC)
18	M03-US-01-A	Elasticity	27th July 2019	10am-4pm (UTC)
19	M03-US-02-A	Elasticity	27th July 2019	10am-4pm (UTC)
20	M03-US-03-A	Elasticity	27th July 2019	10am-4pm (UTC)
21	M03-DE-01-A	Compression strength	27th July 2019	10am-4pm (UTC)
22	M03-DE-02-A	Compression strength	27th July 2019	10am-4pm (UTC)
23	M03-DE-03-A	Compression strength	27th July 2019	10am-4pm (UTC)

A2 Winter pancake ice cores

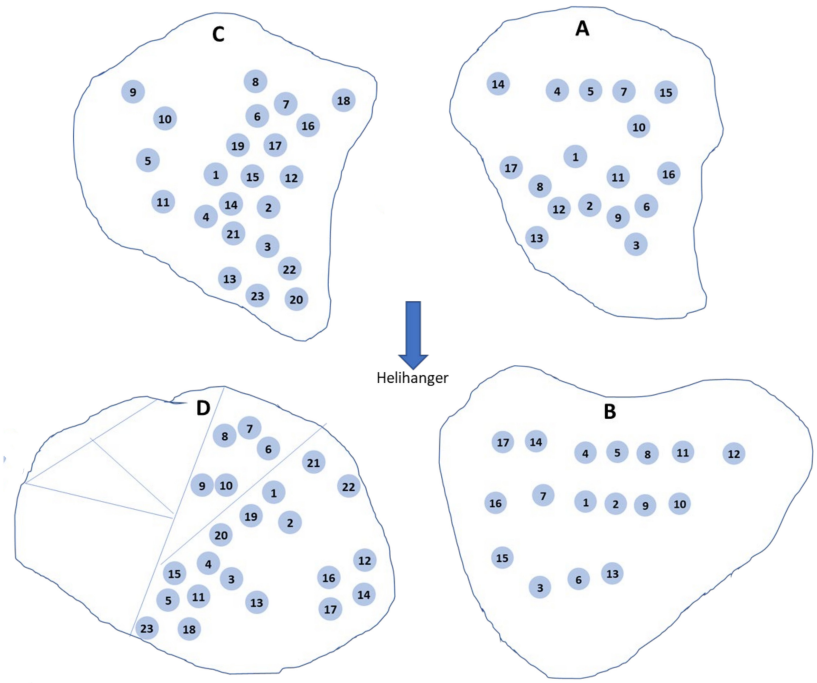

Figure A1: Coring layout for winter pancake ice floes A, B, C and D, respectively.

Table A2: Overview of core IDs of winter pancake A, corresponding core names, testing designation, and date and time when cored.

Core ID	Core Name	Test Designation	Date Cored	Time Cored
1	M01-PHY-01-A	Temperature	28th July 2019	10:50am (UTC)
2	M01-BGC-01-A	Isotope	28th July 2019	11:05am (UTC)
3	M01-PHY-02-A	Temperature	28th July 2019	11:10am (UTC)
4	M01-BGC-02-A	Isotope	28th July 2019	11:12am (UTC)
5	M01-PHY-03-A	Temperature	28th July 2019	11:15am (UTC)
6	M01-CPUT-01-A	Biology	28th July 2019	11:30am (UTC)
7	M01-CPUT-02-A	Biology	28th July 2019	11:32am (UTC)
8	M01-CT-01-A	MicroCT	28th July 2019	11:50am (UTC)
9	M01-CT-02-A	MicroCT	28th July 2019	11:52am (UTC)
10	M01-CP-01-A	Morphology	28th July 2019	12:01pm (UTC)
11	M01-CP-02-A	Morphology	28th July 2019	12:05pm (UTC)
12	M01-US-01-A	Elasticity	28th July 2019	12:06pm (UTC)
13	M01-US-02-A	Elasticity	28th July 2019	12:11pm (UTC)
14	M01-US-03-A	Elasticity	28th July 2019	12:13pm (UTC)
15	M01-DE-01-A	Compression strength	28th July 2019	12:18pm (UTC)
16	M01-DE-02-A	Compression strength	28th July 2019	12:19pm (UTC)
17	M01-DE-03-A	Compression strength	28th July 2019	12:22pm (UTC)

Table A3: Overview of core IDs of winter pancake B, corresponding core names, testing designation, and date and time when cored.

Core ID	Core Name	Test Designation	Date Cored	Time Cored
1	M01-PHY-01-B	Temperature	28th July 2019	11:05am (UTC)
2	M01-BGC-01-B	Isotope	28th July 2019	11:18am (UTC)
3	M01-PHY-02-B	Temperature	28th July 2019	11:20am (UTC)
4	M01-BGC-02-B	Isotope	28th July 2019	11:24am (UTC)
5	M01-PHY-03-B	Temperature	28th July 2019	11:26am (UTC)
6	M01-CPUT-01-B	Biology	28th July 2019	11:35am (UTC)
7	M01-CPUT-02-B	Biology	28th July 2019	11:40am (UTC)
8	M01-CT-01-B	MicroCT	28th July 2019	11:57am (UTC)
9	M01-CT-02-B	MicroCT	28th July 2019	11:59am (UTC)
10	M01-CP-01-B	Morphology	28th July 2019	12:35pm (UTC)
11	M01-CP-02-B	Morphology	28th July 2019	12:47pm (UTC)
12	M01-US-01-B	Elasticity	28th July 2019	12:50pm (UTC)
13	M01-US-02-B	Elasticity	28th July 2019	12:52pm (UTC)
14	M01-US-03-B	Elasticity	28th July 2019	1:38pm (UTC)
15	M01-DE-01-B	Compression strength	28th July 2019	2:06pm (UTC)
16	M01-DE-02-B	Compression strength	28th July 2019	2:09pm (UTC)
17	M01-DE-03-B	Compression strength	28th July 2019	2:11pm (UTC)

Table A4: Overview of core IDs of winter pancake C, corresponding core names, testing designation, and date and time when cored.

Core ID	Core Name	Test Designation	Date Cored	Time Cored
1	M01-PHY-01-C	Temperature	28th July 2019	1:05pm (UTC)
2	M01-BGC-01-C	Isotope	28th July 2019	1:06pm (UTC)
3	M01-PHY-02-C	Temperature	28th July 2019	1:18pm (UTC)
4	M01-BGC-02-C	Isotope	28th July 2019	1:22pm (UTC)
5	M01-PHY-03-C	Temperature	28th July 2019	1:26pm (UTC)
6	M01-TM-01-C	Trace metal	28th July 2019	1:47pm (UTC)
7	M01-TM-02-C	Trace metal	28th July 2019	1:53pm (UTC)
8	M01-TM-03-C	Trace metal	28th July 2019	1:56pm (UTC)
9	M01-TM-04-C	Trace metal	28th July 2019	2:14pm (UTC)
10	M01-TM-05-C	Trace metal	28th July 2019	2:18pm (UTC)
11	M01-CP-01-C	Morphology	28th July 2019	2:23pm (UTC)
12	M01-CPUT-01-C	Biology	28th July 2019	3:40pm (UTC)
13	M01-CPUT-02-C	Biology	28th July 2019	3:42pm (UTC)
14	M01-CT-01-C	MicroCT	28th July 2019	3:44pm (UTC))
15	M01-CT-02-C	MicroCT	28th July 2019	3:45pm (UTC)
16	M01-CP-02-C	Morphology	28th July 2019	3:47pm (UTC)
17	M01-US-01-C	Elasticity	28th July 2019	3:50pm (UTC)
18	M01-US-02-C	Elasticity	28th July 2019	3:51pm (UTC)
19	M01-US-03-C	Elasticity	28th July 2019	3:53pm (UTC)
20	M01-DE-01-C	Compression strength	28th July 2019	3:57pm (UTC)
21	M01-DE-02-C	Compression strength	28th July 2019	3:58pm (UTC)
22	M01-DE-03-C	Compression strength	28th July 2019	4:00pm (UTC)

Table A5: Overview of core IDs of winter pancake D, corresponding core names, testing designation, and date and time when cored.

Core ID	Core Name	Test Designation	Date Cored	Time Cored
1	M01-PHY-01-D	Temperature	28th July 2019	1:13pm (UTC)
2	M01-BGC-01-D	Isotope	28th July 2019	1:16pm (UTC)
3	M01-PHY-01-D	Temperature	28th July 2019	1:30pm (UTC)
4	M01-PHY-02-D	Isotope	28th July 2019	1:35pm (UTC)
5	M01-PHY-03-D	Temperature	28th July 2019	1:40pm (UTC)
6	M01-TM-01-D	Trace metal	28th July 2019	2:34pm (UTC)
7	M01-TM-02-D	Trace metal	28th July 2019	2:36pm (UTC)
8	M01-TM-03-D	Trace metal	28th July 2019	2:36pm (UTC)
9	M01-TM-04-D	Trace metal	28th July 2019	2:42pm (UTC)
10	M01-TM-05-D	Trace metal	28th July 2019	2:44pm (UTC)
11	M01-CPUT-01-D	Biology	28th July 2019	2:52pm (UTC)
12	M01-CPUT-02-D	Biology	28th July 2019	2:55pm (UTC)
13	M01-CT-01-D	MicroCT	28th July 2019	2:59pm (UTC)
14	M01-CT-02-D	MicroCT	28th July 2019	3:02pm (UTC)
15	M01-US-01-D	Elasticity	28th July 2019	3:07pm (UTC)
16	M01-US-02-D	Elasticity	28th July 2019	3:11pm (UTC)
17	M01-US-03-D	Elasticity	28th July 2019	3:14pm (UTC)
18	M01-CP-01-D	Morphology	28th July 2019	3:19pm (UTC)
19	M01-CP-02-D	Morphology	28th July 2019	3:20pm (UTC)
20	M01-DE-01-D	Compression strength	28th July 2019	3:22pm (UTC)
21	M01-DE-02-D	Compression strength	28th July 2019	3:26pm (UTC)
22	M01-DE-03-D	Compression strength	28th July 2019	3:30pm (UTC)
23	M01-CPUT-03-D	Biology	28th July 2019	3:35pm (UTC)

Appendix B: Brash ice and consolidated pack ice core lists for Spring Cruise

B1 Spring consolidated pack ice data

Table B1: Overview of core IDs of spring pack ice on station MIZ2, corresponding core names, testing designation, and date when cored. The table only includes the cores that were brought back to University of Cape Town.

Core ID	Core Name	Test Designation	Date Cored	Time Cored
1	SMIZ2-CMP-07	Compression	24th October 2019	10am-4pm (UTC)
2	SMIZ2-CMP-08	Compression	24th October 2019	10am-4pm (UTC)
3	SMIZ2-CMP-09	Compression	24th October 2019	10am-4pm (UTC)
4	SMIZ2-BGC-13	Isotope	24th October 2019	10am-4pm (UTC)
5	SMIZ2-BGC-14	Isotope	24th October 2019	10am-4pm (UTC)
6	SMIZ2-BGC-15	Isotope	24th October 2019	10am-4pm (UTC)
7	SMIZ2-BGC-16	Isotope	24th October 2019	10am-4pm (UTC)
8	SMIZ2-BGC-17	Isotope	24th October 2019	10am-4pm (UTC)
9	SMIZ2-BGC-18	Isotope	24th October 2019	10am-4pm (UTC)
10	SMIZ2-US-07	Ultrasound	24th October 2019	10am-4pm (UTC)
11	SMIZ2-US-08	Ultrasound	24th October 2019	10am-4pm (UTC)
12	SMIZ2-US-09	Ultrasound	24th October 2019	10am-4pm (UTC)
13	SMIZ2-MRI-03	MRI	24th October 2019	10am-4pm (UTC)
14	SMIZ2-CT-05	CT Scanning	24th October 2019	10am-4pm (UTC)
15	SMIZ2-CP-03	Cross-Polarisation	24th October 2019	10am-4pm (UTC)

Table B2: Overview of core IDs of spring pack ice on station MIZ3, corresponding core names, testing designation, and date when cored. The table only includes the cores that were brought back to University of Cape Town.

Core ID	Core Name	Test Designation	Date Cored	Time Cored
1	SMIZ3-CMP-11	Compression	25th October 2019	10am-4pm (UTC)
2	SMIZ3-CMP-12	Compression	25th October 2019	10am-4pm (UTC)
3	SMIZ3-US-12	Ultrasound	25th October 2019	10am-4pm (UTC)
4	SMIZ3-BGC-19	Isotope	25th October 2019	10am-4pm (UTC)
5	SMIZ3-BGC-20	Isotope	25th October 2019	10am-4pm (UTC)
6	SMIZ3-BGC-21	Isotope	25th October 2019	10am-4pm (UTC)
7	SMIZ3-BGC-22	Isotope	25th October 2019	10am-4pm (UTC)
8	SMIZ3-BGC-23	Isotope	25th October 2019	10am-4pm (UTC)
9	SMIZ3-BGC-24	Isotope	25th October 2019	10am-4pm (UTC)
10	SMIZ3-MRI-04	MRI	25th October 2019	10am-4pm (UTC)
11	SMIZ3-US-10	Ultrasound	25th October 2019	10am-4pm (UTC)
12	SMIZ3-US-11	Ultrasound	25th October 2019	10am-4pm (UTC)
13	SMIZ3-CP-04	MRI	25th October 2019	10am-4pm (UTC)
14	SMIZ2-CT-05	CT Scanning	25th October 2019	10am-4pm (UTC)
15	SMIZ3-CP-04	Cross-Polarisation	25th October 2019	10am-4pm (UTC)

Table B3: Overview of core IDs of spring pack ice on station MIZ6, corresponding core names, testing designation, and date when cored. The table only includes the cores that were brought back to University of Cape Town.

Core ID	Core Name	Test Designation	Date Cored	Time Cored
1	SMIZ4-MRI-05	MRI	29th October 2019	10am-4pm (UTC)
2	SMIZ4-CMP-13	Compression	29th October 2019	10am-4pm (UTC)
3	SMIZ4-CMP-14	Compression	29th October 2019	10am-4pm (UTC)
4	SMIZ4-CMP-15	Compression	29th October 2019	10am-4pm (UTC)
5	SMIZ4-NTS	Nutrients	29th October 2019	10am-4pm (UTC)
6	SMIZ4-CT-09	CT Scanning	29th October 2019	10am-4pm (UTC)
7	SMIZ4-CT-09	CT Scanning	29th October 2019	10am-4pm (UTC)
8	SMIZ4-US-13	Ultrasound	29th October 2019	10am-4pm (UTC)
9	SMIZ4-US-14	Ultrasound	29th October 2019	10am-4pm (UTC)
10	SMIZ4-US-15	Ultrasound	29th October 2019	10am-4pm (UTC)
11	SMIZ4-BGC-25	Isotope	29th October 2019	10am-4pm (UTC)
12	SMIZ4-BGC-26	Isotope	29th October 2019	10am-4pm (UTC)
13	SMIZ4-BGC-27	Isotope	29th October 2019	10am-4pm (UTC)
14	SMIZ4-BGC-28	Isotope	29th October 2019	10am-4pm (UTC)
15	SMIZ4-BGC-30	Isotope	29th October 2019	10am-4pm (UTC)

Table B4: Overview of core IDs of spring pack ice on station MIZ7, corresponding core names, testing designation, and date when cored. The table only includes the cores that were brought back to University of Cape Town.

Core ID	Core Name	Test Designation	Date Cored	Time Cored
1	SMIZ5-CMP-16	Compression	30th October 2019	10am-4pm (UTC)
2	SMIZ5-CMP-17	Compression	30th October 2019	10am-4pm (UTC)
3	SMIZ5-CMP-17	Compression	30th October 2019	10am-4pm (UTC)
4	SMIZ4-CMP-18	Compression	30th October 2019	10am-4pm (UTC)
5	SMIZ5-BGC-31	Isotope	30th October 2019	10am-4pm (UTC)
6	SMIZ5-BGC-32	Isotope	30th October 2019	10am-4pm (UTC)
7	SMIZ5-BGC-33	Isotope	30th October 2019	10am-4pm (UTC)
8	SMIZ5-BGC-34	Isotope	30th October 2019	10am-4pm (UTC)
9	SMIZ5-BGC-35	Isotope	30th October 2019	10am-4pm (UTC)
10	SMIZ5-BGC-36	Isotope	30th October 2019	10am-4pm (UTC)
11	SMIZ5-US-16	Ultrasound	30th October 2019	10am-4pm (UTC)
12	SMIZ5-US-17	Ultrasound	30th October 2019	10am-4pm (UTC)
13	SMIZ5-US-18	Ultrasound	30th October 2019	10am-4pm (UTC)
14	SMIZ5-CT-07	CT Scanning	30th October 2019	10am-4pm (UTC)
15	SMIZ5-CT-11	CT Scanning	30th October 2019	10am-4pm (UTC)
16	SMIZ5-MRI-06	MRI	30th October 2019	10am-4pm (UTC)

B2 Spring brash ice cores

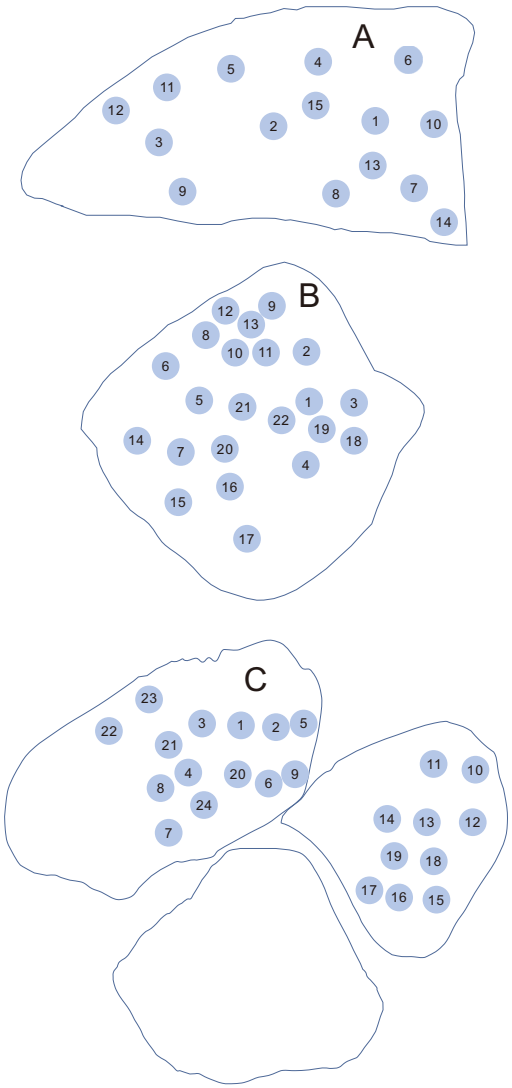

Figure B1: Coring layout for spring brash ice floes A, B (SMIZ 8) and C (SMIZ 9), respectively.

Table B5: Overview of core IDs of spring brash ice A on station SMIZ8, corresponding core names, testing designation, and date and time when cored.

Core ID	Core Name	Test Designation	Date Cored	Time Cored
1	SMIZ8-DE-03A	Compression Strength	1st Nov 2019	10am-4pm (UTC)
2	SMIZ8-PHY-01A	Temperature	1st Nov 2019	10am-4pm (UTC)
3	SMIZ8-PHY-02A	Temperature Strength	1st Nov 2019	10am-4pm (UTC)
4	SMIZ8-US-25A	Ultrasound	1st Nov 2019	10am-4pm (UTC)
5	SMIZ8-US-26A	Ultrasound	1st Nov 2019	10am-4pm (UTC)
6	SMIZ8-MRI-09A	MRI	1st Nov 2019	10am-4pm (UTC)
7	SMIZ8-US-27A	Ultrasound	1st Nov 2019	10am-4pm (UTC)
8	SMIZ8-CT-17A	CT Scanning	1st Nov 2019	10am-4pm (UTC)
9	SMIZ8-CT-18A	CT Scanning	1st Nov 2019	10am-4pm (UTC)
10	SMIZ8-CP-09A	Cross-Polarisation	1st Nov 2019	10am-4pm (UTC)
11	SMIZ8-DE-02A	Compression Strength	1st Nov 2019	10am-4pm (UTC)
12	SMIZ8-DE-01A	Compression Strength	1st Nov 2019	10am-4pm (UTC)
13	SMIZ8-PER-01A	Permeability	1st Nov 2019	10am-4pm (UTC)
14	SMIZ8-DMS-01	Dimethyl Sulphide	1st Nov 2019	10am-4pm (UTC)
15	SMIZ8-PER-02A	Permeability	1st Nov 2019	10am-4pm (UTC)

Table B6: Overview of core IDs of spring brash ice B on station SMIZ8, corresponding core names, testing designation, and date and time when cored.

Core ID	Core Name	Test Designation	Date Cored	Time Cored
1	SMIZ8-PHY-01B	Temperature	1st Nov 2019	10am-4pm (UTC)
2	SMIZ8-INC-01B	Incubation	1st Nov 2019	10am-4pm (UTC)
3	SMIZ8-NTS-01B	Nutrient	1st Nov 2019	10am-4pm (UTC)
4	SMIZ8-NTS-02B	Nutrient	1st Nov 2019	10am-4pm (UTC)
5	SMIZ8-PHY-02B	Temperature	1st Nov 2019	10am-4pm (UTC)
6	SMIZ8-NTS-03B	Nutrient	1st Nov 2019	10am-4pm (UTC)
7	SMIZ8-BGC-50A	Isotope	1st Nov 2019	10am-4pm (UTC)
8	SMIZ8-MRI-10D	MRI	1st Nov 2019	10am-4pm (UTC)
9	SMIZ8-PHY-03B	Temperature	1st Nov 2019	10am-4pm (UTC)
10	SMIZ8-BGC-49A	Isotope	1st Nov 2019	10am-4pm (UTC)
11	SMIZ8-RUAN-01B	Nitrogen	1st Nov 2019	10am-4pm (UTC)
12	SMIZ8-RUAN-02B	Nitrogen	1st Nov 2019	10am-4pm (UTC)
13	SMIZ8-CPUT-01B	Biology	1st Nov 2019	10am-4pm (UTC)
14	SMIZ8-CPUT-02B	Biology	1st Nov 2019	10am-4pm (UTC)

Table B7: Overview of core IDs of spring brash ice on station SMIZ9, corresponding core names, testing designation, and date and time when cored.

Core ID	Core Name	Test Designation	Date Cored	Time Cored
1	SMIZ9-PHY-01A	Temperature	3rd Nov 2019	10am-4pm (UTC)
2	SMIZ9-DE-01A	Compression Strength	3rd Nov 2019	10am-4pm (UTC)
3	SMIZ9-NTS-01A	Nutrient	3rd Nov 2019	10am-4pm (UTC)
4	SMIZ9-PHY-02A	Temperature	3rd Nov 2019	10am-4pm (UTC)
5	SMIZ9-DE-02A	Compression Strength	3rd Nov 2019	10am-4pm (UTC)
6	SMIZ9-DE-03A	Compression Strength	3rd Nov 2019	10am-4pm (UTC)
7	SMIZ9-PHY-02A	Temperature	3rd Nov 2019	10am-4pm (UTC)
8	SMIZ9-NTS-02A	Nutrient	3rd Nov 2019	10am-4pm (UTC)
9	SMIZ9-INC-01A	Incubation	3rd Nov 2019	10am-4pm (UTC)
10	SMIZ9-CMP-28A	Compression	3rd Nov 2019	10am-4pm (UTC)
11	SMIZ9-CMP-29A	Compression	3rd Nov 2019	10am-4pm (UTC)
12	SMIZ9-CMP-30A	Compression	3rd Nov 2019	10am-4pm (UTC)
13	SMIZ9-MRI-01A	MRI	3rd Nov 2019	10am-4pm (UTC)
14	SMIZ9-CT-01A	CT Scanning	3rd Nov 2019	10am-4pm (UTC)
15	SMIZ9-CT-02A	CT Scannin	3rd Nov 2019	10am-4pm (UTC)
16	SMIZ9-CP-01A	CT Scannin	3rd Nov 2019	10am-4pm (UTC)
17	SMIZ9-CMP-01A	Compression	3rd Nov 2019	10am-4pm (UTC)
18	SMIZ9-CMP-02A	Compression	3rd Nov 2019	10am-4pm (UTC)
19	SMIZ9-DMS-02A	Dimethyl Sulphide	1st Nov 2019	10am-4pm (UTC)
20	SMIZ9-PER-02A	Permeability	3rd Nov 2019	10am-4pm (UTC)
21	SMIZ9-PER-01A	Permeability	3rd Nov 2019	10am-4pm (UTC)
22	SMIZ9-BGC-59A	Isotope	3rd Nov 2019	10am-4pm (UTC)
23	SMIZ9-BGC-57A	Isotope	3rd Nov 2019	10am-4pm (UTC)
24	SMIZ9-DMS-01A	Dimethyl Sulphide	3rd Nov 2019	10am-4pm (UTC)

Bibliography

[1] Ackley, S. The growth, structure, and properties of sea ice. *CRREL Monog*, 82, 01 1991.

[2] Albert, M. R. and Perron Jr., F. E. Ice layer and surface crust permeability in a seasonal snow pack. *Hydrological Processes*, 14(18):3207–3214, 2000.

[3] Albert, M. R., Shultz, E. F., and Perron, F. E. Snow and firn permeability at siple dome, antarctica. *Annals of Glaciology*, 31:353–356, 2000.

[4] Ashton, G. D. *River and lake ice engineering*. Littleton, Colo., U.S.A. : Water Resources Publications, 1986.

[5] Bennington, K. Some crystal growth features of sea ice. *Journal of Glaciology - J GLACIOLOGY*, 4:669–688, 01 1963.

[6] Brace, W. F., Walsh, J. B., and Frangos, W. T. Permeability of granite under high pressure. *Journal of Geophysical Research (1896-1977)*, 73(6):2225–2236, 1968.

[7] Carnat, G., Papakyriakou, T., Geilfus, N., Brabant, F., Delille, B., Vancoppenolle, M., Gilson, G., Zhou, J., and Tison, J.-L. Investigations on physical and textural properties of arctic first-year sea ice in the amundsen gulf, canada, november 2007–june 2008 (ipy-cfl system study). *Journal of Glaciology*, 59(217):819–837, 2013.

[8] Cole, D. M. and Shapiro, L. H. Observations of brine drainage networks and microstructure of first-year sea ice. *Journal of Geophysical Research: Oceans*, 103(C10):21739–21750, 1998.

[9] Cole, D. M., Eicken, H., Frey, K., and Shapiro, L. H. Observations of banding in first-year arctic sea ice. *Journal of Geophysical Research: Oceans*, 109(C8), 2004.

[10] Cottier, F. Brine distribution in young sea ice (doctoral thesis). 05 1999.

[11] Cox, G. and Weeks, W. Brine drainage and initial salt entrapment in sodium chloride ice. *CRREL Res Rep*, 345:88, 12 1975.

[12] Cox, G. F. N., Richter, J. A., Weeks, W. F., and Mellor, M. A Summary of the Strength and Modulus of Ice Samples From Multi-Year Pressure Ridges. volume 107, pages 93–98, 03 1985.

[13] Cox, G. F. N. and Weeks, W. F. Salinity variations in sea ice. *Journal of Glaciology*, 13(67):109–120, 1974.

[14] Cox, G. and Weeks, W. Changes in the salinity and porosity of sea-ice samples during shipping and storage. *Journal of Glaciology*, 32(112):371–375, 1986.

[15] Cox, G., Weeks, W., Company, S. D., Service, U. S. M. M., Research, C. R., and (U.S.), E. L. *Equations for Determining the Gas and Brine Volumes in Sea Ice Samples*. CRREL report. US Army Corps of Engineers, Cold Regions Research & Engineering Laboratory, 1982.

[16] Cox, G. F. N. and Weeks, W. F. Numerical simulations of the profile properties of undeformed first-year sea ice during the growth season. *Journal of Geophysical Research*, 93:12449–12460, 1988.

[17] Eicken, H., Grenfell, T. C., Perovich, D. K., Richter-Menge, J. A., and Frey, K. Hydraulic controls of summer arctic pack ice albedo. *Journal of Geophysical Research: Oceans*, 109(C8), 2004.

[18] Eicken, H., Krouse, H. R., Kadko, D., and Perovich, D. K. Tracer studies of pathways and rates of meltwater transport through arctic summer sea ice. *Journal of Geophysical Research: Oceans*, 107(C10):SHE 22–1–SHE 22–20, 2002.

[19] Eicken, H. Salinity profiles of antarctic sea ice: Field data and model results. *Journal of Geophysical Research: Oceans*, 97(C10):15545–15557, 1992.

[20] Eicken, H., Fischer, H., and Lemke, P. Effects of the snow cover on antarctic sea ice and potential modulation of its response to climate change. *Annals of Glaciology*, 21:369–376, 1995.

[21] Eicken, H. and Lange, M. A. Development and properties of sea ice in the coastal regime of the southeastern weddell sea. *Journal of Geophysical Research: Oceans*, 94(C6):8193–8206, 1989.

[22] Eide, L. and Martin, S. The formation of brine drainage features in young sea ice. *Journal of Glaciology*, 14:137–154, 01 1975.

[23] Fortin, G., van Bochove, E., Jones, H., Thériault, G., and Bernier, M. The simultaneous determination of air permeability and gas diffusion through ice layers in the field. *Hydrology Research*, 38, 08 2007.

[24] Frankenstein, G. and Garner, R. Equations for determining the brine volume of sea ice from -0.5° to -22.9°c. *Journal of Glaciology*, 6(48):943–944, 1967.

[25] Freitag, J. Untersuchungen zur hydrologie des arktischen meereises : Konsequenzen den kleinskaligen stofftransport = the hydraulic properties of arctic sea-ice : implications for the small scale particle transport. 1999.

[26] Freitag, J. and Eicken, H. Meltwater circulation and permeability of arctic summer sea ice derived from hydrological field experiments. *Journal of Glaciology*, 49(166):349–358, 2003.

[27] Golden, K. M., Ackley, S. F., and Lytle, V. I. The percolation phase transition in sea ice. *Science*, 282(5397):2238–2241, 1998.

[28] Golden, K. M., Eicken, H., Heaton, A. L., Miner, J., Pringle, D. J., and Zhu, J. Thermal evolution of permeability and microstructure in sea ice. *Geophysical Research Letters*, 34(16), 2007.

[29] Golden, K. Critical behavior of transport in sea ice. *Physica B: Condensed Matter*, 338(1):274–283, 2003. Proceedings of the Sixth International Conference on Electrical Transport and Optical Properties of Inhomogeneous Media.

[30] Golovin, P. Structural features of sub-ice convection in winter arctic leads: Comparison of full-scale and laboratory experiments. *Russian Meteorology and Hydrology*, 01 2004.

[31] Gough, A. J., Mahoney, A. R., Langhorne, P. J., Williams, M. J. M., and Haskell, T. G. Sea ice salinity and structure: A winter time series of salinity and its distribution. *Journal of Geophysical Research: Oceans*, 117(C3), 2012.

[32] Harrison, J. and Tiller, W. Controlled freezing of water. *Ice and Snow*, page 1, 01 1962.

[33] Hemmingsen, E. Permeation of gases through ice. *Tellus*, 11(3):355–359, 1959.

[34] Hoekstra, P. and Osterkamp, T. The migration of liquid inclusions in single ice crystals. *Journal of Geophysical Research*, 70:5035–5041, 10 1965.

[35] Jaccard, C. P. v. hobbs ice physics. oxford, clarendon press, 1974. xvii, 837 p. £29. *Journal of Glaciology*, 17(75):155–156, 1976.

[36] Jeffries, M. O. and Weeks, W. F. Structural characteristics and development of sea ice in the western ross sea. *Antarctic Science*, 5(1):63–75, 1993.

[37] Jeffries, M. O., Shaw, R. A., Morris, K., Veazey, A. L., and Krouse, H. R. Crystal structure, stable isotopes (δ18o), and development of sea ice in the ross, amundsen, and bellingshausen seas, antarctica. *Journal of Geophysical Research: Oceans*, 99(C1):985–995, 1994.

[38] Johannes, F. and Hajo, E. Meltwater circulation and permeability of arctic summer sea ice derived from hydrological field experiments. *Journal of Glaciology*, 49(166):349–358, 2003.

[39] Johnson, S. Master's thesis: Evaluation of the changes in the crystal structure of antarctic sea ice from the marginal ice zone during winter and spring. 2020.

[40] Johnston, M. and Timco, G. Temperature changes in first year arctic sea ice during the decay process. In *Proceedings of the 16th IAHR International Symposium on Ice*, volume 2, page 194–202, Dunedin, New Zealand, 2009.

[41] Kawamura, T., Ishikawa, M., Takatsuka, T., Kojima, S., and Shirasawa, K. Measurements of permeability of sea ice. 01 2006.

[42] Kingery, W. D. and Goodnow, W. H. Brine migration in salt ice, in ice and snow: Properties, processes and applications. *MIT Press*, page 237– 247, 1963.

[43] Klinkenberg, L. J. The permeability of porous media to liquids and gases. 1941.

[44] Kovacs, A. *Sea Ice: Bulk salinity versus ice floe thickness.* Number pt. 1 in CRREL report. U.S. Army Cold Regions Research and Engineering Laboratory, 1996.

[45] Kuroiwa, D. Liquid permeability of snow. *Low Temperature Science*, 79, 01 1968.

[46] Lake, R. A. and Lewis, E. L. Salt rejection by sea ice during growth. *Journal of Geophysical Research (1896-1977)*, 75(3):583–597, 1970.

[47] Landy, J., Ehn, J., Shields, M., and Barber, D. Surface and melt pond evolution on landfast first-year sea ice in the canadian arctic archipelago. *Journal of Geophysical Research: Oceans*, 119(5):3054–3075, 2014.

[48] Lange, M. A. and Eicken, H. Textural characteristics of sea ice and the major mechanisms of ice growth in the weddell sea. *Annals of Glaciology*, 15:210–215, 1991.

[49] Langhorne, P. and Robinson, W. Alignment of crystals in sea ice due to fluid motion. *Cold Regions Science and Technology*, 12:197–214, 04 1986.

[50] Leonard, G. H., Purdie, C. R., Langhorne, P. J., Haskell, T. G., Williams, M. J. M., and Frew, R. D. Observations of platelet ice growth and oceanographic conditions during the winter of 2003 in mcmurdo sound, antarctica. *Journal of Geophysical Research: Oceans*, 111(C4), 2006.

[51] Martin, S. A field study of brine drainage and oil entrainment in first-year sea ice. *Journal of Glaciology*, 22(88):473–502, 1979.

[52] Maus, S. and De La Rosa, S. Salinity and solid fraction of frazil and grease ice. *Journal of Glaciology*, 58(209):594–612, 2012.

[53] Nakawo, M. and Sinha, N. K. Growth rate and salinity profile of first-year sea ice in the high arctic. *Journal of Glaciology*, 27(96):315–330, 1981.

[54] Nakowo, M. and Sinha, N. A note on brine layer spacing of first-year sea ice. *Atmosphere-Ocean*, 22, 06 1984.

[55] Naumann, A. K., Notz, D., Hvik, L., and Sirevaag, A. Laboratory study of initial sea-ice growth: properties of grease ice and nilas. *The Cryosphere*, 6(4):729–741, 2012.

[56] Neumann, G. and Pierson, W. *Principles of Physical Oceanography.* Prentice Hall, 1968.

[57] Noda, H. and Shimamoto, T. Thermal Pressurization and Slip-Weakening Distance of a Fault: An Example of the Hanaore Fault, Southwest Japan. *Bulletin of the Seismological Society of America*, 95(4):1224–1233, 08 2005.

[58] Notz, D., Wettlaufer, J. S., and Worster, M. G. A non-destructive method for measuring the salinity and solid fraction of growing sea ice in situ. *Journal of Glaciology*, 51(172):159–166, 2005.

[59] Notz, D. and Worster, M. In situ measurements of the evolution of young sea ice. *J. Geophys. Res*, 113, 03 2008.

[60] Notz, D. and Worster, M. Desalination processes of sea ice revisited. *J. Geophys. Res*, 114, 05 2009.

[61] Perovich, D. K. and Polashenski, C. Albedo evolution of seasonal arctic sea ice. *Geophysical Research Letters*, 39(8), 2012.

[62] Petrich, C. and Eicken, H. *Growth, Structure and Properties of Sea Ice*, chapter 2, pages 23–77. John Wiley & Sons, Ltd, 2009.

[63] Petrich, C., Langhorne, P., and Sun, Z. Modelling the interrelationships between permeability, effective porosity and total porosity in sea ice. *Cold Regions Science and Technology*, 44:131–144, 03 2006.

[64] Petrich C., L. P. and Eicken, H. Salinity development in growing sea ice. 2009.

[65] Polashenski, C., Golden, K. M., Perovich, D. K., Skyllingstad, E., Arnsten, A., Stwertka, C., and Wright, N. Percolation blockage: A process that enables melt pond formation on first year arctic sea ice. *Journal of Geophysical Research: Oceans*, 122(1):413–440, 2017.

[66] Polashenski, C., Perovich, D., and Courville, Z. The mechanisms of sea ice melt pond formation and evolution. *Journal of Geophysical Research: Oceans*, 117(C1), 2012.

[67] Provost, C., Sennéchael, N., Miguet, J., Itkin, P., Rösel, A., Koenig, Z., Villacieros-Robineau, N., and Granskog, M. A. Observations of flooding and snow-ice formation in a thinner arctic sea-ice regime during the n-ice2015 campaign: Influence of basal ice melt and storms. *Journal of Geophysical Research: Oceans*, 122(9):7115–7134, 2017.

[68] Richter-Menge, J. A. and Cox, G. F. N. Structure, Salinity and Density of Multi-Year Sea Ice Pressure Ridges. *Journal of Energy Resources Technology*, 107(4):493–497, 12 1985.

[69] Shimizu, H. Air permeability of deposited snow. *Contributions from the Institute of Low Temperature Science*, A22:1–32, 03 1970.

[70] Shreve, R. Migration of air bubbles, vapor figures, and brine pockets in ice under a temperature gradient. *Journal of Geophysical Research*, 72, 08 1967.

[71] Skatulla, S., Audh, R. R., Cook, A., Hepworth, E., Johnson, S., Lupascu, D. C., MacHutchon, K., Marquart, R., Mielke, T., Omatuku, E., Paul, F., Rampai, T., Schröder, J., Schwarz, C., and Vichi, M. Physical and mechanical properties of winter first-year ice in the antarctic marginal ice zone along the good hope line. *The Cryosphere Discussions*, 2021:1–35, 2021.

[72] Skatulla, S., Audh, R. R., Cook, A., Hepworth, E., Johnson, S., Lupascu, D. C., MacHutchon, K., Marquart, R., Mielke, T., Omatuku, E., Paul, F., Rampai, T., Schröder, J., Schwarz, C., and Vichi, M. Data repository for physical and mechanical properties of winter first-year ice in the antarctic marginal ice zone along the good hope line. *University of Cape Town*, https://doi.org/10.25375/uct.14900361 2021.

[73] Sturm, M., Morris, K., and Massom, R. *The Winter Snow Cover of the West Antarctic Pack Ice: Its Spatial and Temporal Variability*, pages 1–18. American Geophysical Union (AGU), 1998.

[74] Tanikawa, W. and Shimamoto, T. Comparison of klinkenberg-corrected gas permeability and water permeability in sedimentary rocks. *International Journal of Rock Mechanics and Mining Sciences*, 46:229–238, 12 2009.

[75] Taujoo, H. Master's thesis: Design of gravity experiment to measure the permeability of antarctic sea ice. 2019.

[76] Timco, G. and Weeks, W. A review of the engineering properties of sea ice. *Cold Regions Science and Technology*, 60(2):107–129, 2010.

[77] Untersteiner, N. Natural desalination and equilibrium salinity profile of perennial sea ice. *Journal of Geophysical Research (1896-1977)*, 73(4):1251–1257.

[78] Vancoppenolle, M., Goosse, H., de Montety, A., Fichefet, T., Tremblay, B., and Tison, J.-L. Modeling brine and nutrient dynamics in antarctic sea ice: The case of dissolved silica. *Journal of Geophysical Research: Oceans*, 115(C2), 2010.

[79] Vancoppenolle, M., Notz, D., Vivier, F., Tison, J.-L., Delille, B., Carnat, G., Zhou, J., Jardon, F., Griewank, P., Lourenco, A., and Haskell, T. Technical note: On the use of the mushy-layer rayleigh number for the interpretation of sea-ice-core data. *The Cryosphere Discussions*, 7:3209–3230, 07 2013.

[80] Vichi, M. A statistical definition of the antarctic marginal ice zone. *The Cryosphere Discussions*, 2021:1–23, 2021.

[81] Wakatsuchi, M. Brine exclusion process from growing sea ice. *Contributions from the Institute of Low Temperature Science*, A33:29–65, mar 1984.

[82] Weeks, W. F. and Ackley, S. F. *The Growth, Structure, and Properties of Sea Ice*, pages 9–164. Springer US, Boston, MA, 1986.

[83] Weeks, W. and Wettlaufer, J. Crystal orientations in floating ice sheets. 01 1996.

[84] Wettlaufer, J., WORSTER, M., and Huppert, H. Natural convection during solidification of an alloy from above with application to the evolution of sea ice. *Journal of Fluid Mechanics*, 344:291 – 316, 08 1997.

[85] Wettlaufer, J. S. Introduction to crystallization phenomena in natural and artificial sea ice, in physics of ice-covered seas. pages 105–194, 1998.

[86] Wibberley, C. Hydraulic diffusivity of fault gouge zones and implications for thermal pressurization during seismic slip. *Earth Planets and Space*, 54:1153 – 1171, 11 2002.

[87] Wibberley, C. and Shimamoto, T. Earthquake slip weakening and asperities explained by fluid pressurization. *Nature*, 436:689–92, 09 2005.

[88] Worster, M. Natural convection, solute trapping, and channel formation during solidification of saltwater. *Journal of Physical Chemistry B - J PHYS CHEM B*, 101, 08 1997.

[89] Worster, M. Convection in mushy layers. *Annual Review of Fluid Mechanics*, 29:91–122, 11 2003.

[90] Worster, M. G. and Wettlaufer, J. S. Natural convection, solute trapping, and channel formation during solidification of saltwater. *The Journal of Physical Chemistry B*, 101(32):6132–6136, 1997.